

**NASA
Technical
Paper
2804**

May 1988

**Aerothermal Tests of
Quilted Dome Models
on a Flat Plate at a
Mach Number of 6.5**

Christopher E. Glass
and L. Roane Hunt

(NASA-TP-2804) AEROTHERMAL TESTS OF QUILTED
DOME MODELS ON A FLAT PLATE AT A MACH NUMBER
OF 6.5 (NASA) 72 p CSCL 20D

N88-22325

Unclas

H1/34 0140759

NASA

**NASA
Technical
Paper
2804**

1988

Aerothermal Tests of Quilted Dome Models on a Flat Plate at a Mach Number of 6.5

Christopher E. Glass
and L. Roane Hunt

*Langley Research Center
Hampton, Virginia*



National Aeronautics
and Space Administration

Scientific and Technical
Information Division

Summary

Aerothermal tests were conducted in the NASA Langley 8-Foot High-Temperature Tunnel (8' HTT) at a Mach number of 6.5 on simulated arrays of thermally bowed metallic thermal protection system (TPS) tiles at an angle of attack of 5° . Detailed surface pressures and heating rates were obtained for arrays aligned with the flow and skewed 45° diagonally to the flow with nominal bowed heights of 0.1, 0.2, and 0.4 in. submerged in both laminar and turbulent boundary layers. Aerothermal tests were made at a nominal total temperature of 3300°R , a total pressure of 400 psia, a total enthalpy of 950 Btu/lbm, a dynamic pressure of 2.7 psi, and a unit Reynolds number of 0.4×10^6 per foot. The experimental results form a data base that can be used to help predict aerothermal load increases from bowed arrays of TPS tiles.

Surface heating for the aligned array with a laminar boundary layer was characteristic of two-dimensional flow and the peak heating occurred just forward of the dome center. However, heating for the skewed array with a laminar boundary layer showed three-dimensional effects of vortical flow impingement with attendant high heating. Heating for the aligned and skewed arrays with a turbulent boundary layer was characteristic of two-dimensional flow with higher heating on the windward surface. In general, heating for the downstream tiles was less than for the upstream tiles. At the 0.1 in. height, representative of a bowed metallic TPS tile, the integrated heat load over the dome increased less than 15 percent and the pressure drag was at least an order of magnitude less than the calculated flat-plate skin friction.

Introduction

An important design consideration for many hypersonic flight vehicles is the thermal protection system (TPS) for the load-carrying structure. Various candidates of both ceramic and metallic designs have been fabricated and tested. (For example, see refs. 1-4.)

All the various TPS concepts have inherent surface irregularities that must be studied both analytically and experimentally to determine whether these surface irregularities cause significant increases in either pressure or heat load or both. (Higher thermal loads may require higher temperature materials, which may result in increased mass of the flight vehicle.) One concern about the ceramic TPS concepts associated with surface irregularity has been surface gaps between tiles, which allow for thermal and mechanical deflections. (See refs. 1 and 2.) Many

of these gaps have been filled with various flexible fillers that are costly in labor and weight. The earlier metallic concepts, presented in references 2 and 3, were characterized by a corrugated aerodynamic surface. The average and peak heating penalties due to the corrugated surface are small for crossflow angles of 10° or less but are significantly higher for the larger crossflow angles (ref. 5). A more recent metallic design, as described in references 6 and 7, features a metallic tile, with a low thermal conductance, mechanically attached at each corner to the primary structure. A typical 20-tile metallic TPS design is shown in figure 1 glowing during an aerothermal test in the NASA Langley 8-Foot High-Temperature Tunnel. This metallic design, although relatively smooth at ambient conditions, has surface irregularities due to thermal bowing of the individual tiles, which is allowed in order to relieve thermally induced stresses at operating temperatures. The design features an overlapping edge on two sides of each tile to eliminate open gaps such as occur between the ceramic Shuttle tiles. An array of bowed tiles over the surface of a vehicle would alter the surface to a quilted or wavy pattern and modify the aerothermal pressure and heat loads on the surface.

The flow over wavy surfaces associated with the earlier metallic concepts was studied analytically in references 8 and 9; however, the most successful methods were empirical. (See refs. 5 and 10.) Extrapolation of flow behavior from localized regions to large surface areas is the most difficult part of the complete vehicle analysis. The solution to the full Navier-Stokes equations for laminar Mach 7 flow over the quilted surface pattern of bowed TPS tiles (refs. 11 and 12) is a major contribution in defining the interactions between the flow field and the surface irregularities associated with bowed TPS tiles. The Navier-Stokes analysis of reference 11 was applied to a single row of spherical dome protuberances oriented with the row transverse to the flow. This analysis provides very graphic details of the flow field and local heating on domes and shows the effect of height variations from one-half to twice the laminar-boundary-layer thickness. The laminar analysis in reference 12, which was an extension from the single row of domes to a series of domes in a quilted pattern, revealed that vortices shed by the leading dome of the skewed quilted pattern impinged on the sides of the downstream domes and significantly increased the heating. This analysis also indicated that the heat load to the downstream domes was substantially less than that to the leading dome. However,

the analysis needs a turbulence model to study the fully turbulent case and to include transitional flow due to the flow disturbance produced by the domes in realistic flow simulation.

Presented in reference 13 are the results of an experimental aerothermal study of a single row of spherical dome protuberances transversely oriented to a Mach 6.5 flow with laminar and turbulent boundary layers. A baseline dome was chosen to have a diameter of 14 in. with a dome height of 0.1 in. based on preliminary calculations that showed a 9.9- × 9.9-in. tile (diagonal length of 14 in.) would bow 0.1 in. at the design temperature differential. The dome diameter D and the dome height H were varied from $D/H = 0.007$ to $D/H = 0.028$ to parametrically establish pressure and heating-rate distributions on the domes.

The present study was designed to provide experimental data for comparison with the laminar analysis of reference 12 and to provide experimental data for the turbulent-boundary-layer flow condition. For this study, a quilted pattern of 9.9- × 9.9-in. domes was tested aligned with the flow and skewed 45° diagonally to the flow. A baseline condition of 0.1-in.-high domes simulated the quilted metallic tile bowed height. Also, dome heights of 2 and 4 times the baseline condition were tested to establish the pressure and heating-rate distribution trends. Aerothermal tests were made in the Langley 8-Foot High-Temperature Tunnel at a Mach number of 6.5, a total temperature of 3300°R, a total pressure of 400 psia, a total enthalpy of 950 Btu/lbm, a unit Reynolds number of 0.4×10^6 per foot, a dynamic pressure of 2.7 psi, and an angle of attack of 5°. Detailed surface pressure and heating-rate distributions were obtained for domes submerged in both laminar and turbulent boundary layers. The results of this study are presented herein and serve as a data base to complement and verify predictions of the increased aerothermal loads due to the thermally induced bowing of metallic TPS tiles in a quilted pattern.

Symbols

A_{xy}	dome area projected in the x - y plane, in ²
A_{yz}	dome area projected in the y - z plane (normal to the local flow), in ²
$C_{D,P}$	pressure drag coefficient, $\frac{F_P}{\frac{1}{2}(\rho u^2)_e A_{xy}}$
C_p	constant-pressure specific heat, Btu/lbm-°R

$C_{\tau,fp}$	flat-plate skin-friction coefficient, $\frac{\tau}{\frac{1}{2}(\rho u^2)_e}$
D	dome diameter, in.
F_P	pressure drag force, $\sum_{n=1}^N p_n A_{yzn}$, lbf
H	dome height, in.
M	Mach number
N_{Pr}^*	local Prandtl number based on Eckert's reference temperature
N_{St}^*	local Stanton number based on Eckert's reference temperature
P	pressure load, $\sum_{n=1}^N p_n A_{xyn}$, lbf
p	pressure, psia
Q	heat load, $\sum_{n=1}^N \dot{q}_n A_{xyn}$, Btu/sec
\dot{q}	heating rate, Btu/ft ² -sec
R	dome radius, in.
Re	free-stream unit Reynolds number per foot
Re_s	local Reynolds number based on characteristic length S from the leading edge
r, θ	polar coordinates (see fig. 5)
S	distance from panel holder leading edge, in. (see fig. 3)
T	temperature, °R
t	time, sec
u	velocity in streamwise direction, ft/sec
V_∞	free-stream velocity, ft/sec
x, y, z	Cartesian coordinates (see fig. 5)
Z	pressure orifice height
α	angle of attack
γ	ratio of specific heats
Δ	incremental change of
δ	velocity boundary-layer thickness, in.
ρ	density, lbm/ft ³
τ	skin thickness, in.; also wall shear stress, psi
1,2,3,...	referring to location or measurement number

Subscripts:

aw	adiabatic wall
e	boundary-layer edge
fp	flat plate
ip	instrumented plug
t	test chamber total conditions
w	wall
∞	test chamber free-stream conditions

Superscript:

*	based on Eckert's reference temperature
---	---

Abbreviations:

B.L.	boundary layer
C	ceramic dome
id	inside diameter
L.E.	leading edge
od	outside diameter
P	pressure dome
T	heat flux dome
TPS	thermal protection system
2-D	two-dimensional
3-D	three-dimensional

Apparatus and Test

Model

The quilted dome model shown in figure 2 installed in the Langley 8-Foot High-Temperature Tunnel consists of 9.9- × 9.9-in. simulated TPS tiles bowed spherically outward mounted on the flat-plate panel holder. The aerodynamic fences are used to maintain two-dimensional flow over the test surface by preventing vortical flow spillage at the test angle of attack of 5°. A laminar boundary layer was established over the test surface by using a 0.38-in-radius blunt leading edge, and a turbulent boundary layer was established by using 0.19-in-diameter spherical flow trips evenly spaced four diameters apart along the top surface of a sharp leading edge. The two solid copper leading edges are shown schematically in figure 3. (See ref. 14 for more details on both leading edge configurations.) The entire windward surface is covered with 1.0-in-thick ceramic panels to insulate the panel holder structure from aerothermal heating.

To avoid interference due to thermal bowing, metallic TPS tiles must be installed in straight patterns rather than the staggered pattern used for the Shuttle ceramic tiles. When a metallic TPS tile array with a straight pattern is applied to an actual vehicle, the local flow angle relative to the tile pattern varies from 0° to 45°, which causes a design dilemma; i.e., no optimum flow direction can be achieved for the entire tile array. Because local flow angle can vary over the surface of a vehicle, the two extreme flow directions of 0° and 45° were included in the model inserts, as shown in figure 3. Configuration A is the aligned case, and configurations B and C are variations of the 45° skewed case. Each configuration is faired with the upstream flat surface by using one or more bowed leading domes. The aligned array, configuration A, is faired to the upstream surface by three bowed leading domes abreast, with the middle dome centered on the symmetry line. Configuration C is faired to the upstream surface with a single leading dome; however, most of the skewed array test runs were made with configuration B, which is faired with two leading domes to match the analytical model of reference 12.

The individual domes were interchangeable to form the various configurations. The domes were set into the panel inserts with peripheral gaps no greater than 0.05 in. Most of the test runs were made with open longitudinal gaps to facilitate model changes, but additional runs for configuration A with laminar flow were made with the longitudinal gaps closed with ceramic filler because open longitudinal gaps caused boundary-layer transition. The location of each array is shown relative to the panel insert and the panel holder leading edge in figure 3. The designations "P" and "T" (fig. 3) correspond to the normal positions for the pressure-instrumented dome and the thermocouple-instrumented heat flux dome, respectively. All other domes in the array were ceramic. Table I gives the locations of the instrumented domes for each run, and the designation "C" is used for the ceramic domes when instrumented domes were not used.

The baseline dome has a nominal height (distance above the flat-plate surface) of 0.1 in., corresponding to the expected maximum bowed height of a typical TPS concept. The tiles were 9.9 × 9.9 in., which results in a diagonal length of 14 in. that matches the baseline dome surface curvature of the earlier tests of reference 13. For the parametric study, the spherical dome radius was varied to produce nominal heights of 0.1, 0.2, and 0.4 in. to exaggerate surface data trends associated with the larger protuberance heights. The actual dome heights for each run are presented in table I for the four positions indicated in figure 4 along

the centerline. The heights were greater than nominal because some domes did not meet fabrication tolerances so other domes were shimmed to maintain constant dome height. Variance from the nominal height can be identified in the table.

Each dome consisted of a 0.50-in. base that was recessed below the test surface and an upper spherical dome portion that protruded above the surface, as shown in figure 5. The domes were fastened to the panel insert with a single stud at their center. The pressure domes were machined from solid stainless steel, and the upper spherical portion was machined to match the nominal dimensions. However, the heat flux domes were fabricated with less precision in that the thin-wall material was formed from a 0.031-in-thick AISI 316 stainless steel sheet and then attached to the machined base with countersunk screws around the perimeter. The ceramic domes were cast with Resco Cast RS-17E material for each height. The ceramic domes were used to complete the quilted array about the instrumented domes and used to determine the temperature pattern on the surface of an insulating material for comparison with heating patterns obtained from the thin-wall metallic domes.

Instrumentation

The pressure and heat flux domes were instrumented with 59 sensors distributed as given by table II, using polar coordinates r and θ . The instrumented dome coordinate system is shown in figure 5(a), and selected instrument location numbers are shown in figure 5(b) for the aligned and skewed orientations. The pressure domes were instrumented using 0.060-in-id stainless steel tubes mounted through holes drilled in the domes, silver soldered in place, and filed smooth to the outer surface. The tubes were attached to individual electro-mechanical pressure transducers located inside the panel holder directly below the panel inserts. The heat flux domes were instrumented with Chromel-Alumel thermocouples with individual wires spot-welded 0.040 in. apart to the underside of the thin-wall cover sheet. By using a one-dimensional transient heat balance, the local surface heat flux was determined from the slope of the temperature time histories of the thermocouples.

The surface temperatures on the ceramic model were measured and recorded by an AGA Thermovision System 680 (AGA-680) infrared scanner mounted directly over the panel. Other instrumentation on the panel holder consisted of an instrumented plug and a boundary-layer probe shown schematically in figure 6. The instrumented plug had a Gardon heat flux gage and a pressure orifice to mea-

sure surface heat flux and static pressure forward of the dome model ($S = 28.2$ in.) and was used only to monitor real-time surface conditions on the panel holder during the tunnel tests. The boundary-layer probe had twelve 0.06-in-od pitot pressure tubes and was used in two runs to define the boundary layer forward of the dome model ($S = 26.2$ in.) for both laminar and turbulent conditions. Pressure orifice heights and calculated Mach number are presented in table III for runs 1 and 22.

Test Facility

The Langley 8-Foot High-Temperature Tunnel (8' HTT) is a large blowdown tunnel that simulates aerodynamic heating and pressure loading for a nominal Mach number of 7 at altitudes between 80 000 and 120 000 ft. (See fig. 7.) The high energy needed for simulation is obtained by burning a mixture of methane and air under pressure in the combustor and expanding the products of combustion through a conical-contoured nozzle into the open-jet test chamber. The flow enters a supersonic diffuser where it is pumped by an air ejector through a mixing tube and exhausted to the atmosphere through a subsonic diffuser. The tunnel operates at total temperatures from 2400°R to 3600°R, free-stream dynamic pressures from 250 to 1800 psf, free-stream unit Reynolds numbers from 0.3×10^6 to 2.2×10^6 per foot, and has a maximum test time of 120 sec.

The model is stored in the pod below the test stream to protect it from adverse tunnel start-up loads. Once the desired flow conditions are established, the model is inserted into the test stream on a hydraulically actuated elevator. Insertion time was typically 1.5 sec. The model pitch system provides an angle-of-attack range of $\pm 20^\circ$. More detailed information about the tunnel can be found in references 14 and 15.

Test Procedure

The free-stream flow conditions and flat-plate reference values for the tunnel tests are presented in table IV. Nominal run conditions for this test were total temperature of 3300°R, total pressure of 400 psia, and total enthalpy of 950 Btu/lbm. The free-stream test conditions presented are based on a data base of previous tunnel surveys, and the thermal, transport, and flow properties for the combustion products of methane and air are presented in reference 16. The present test was conducted using two surface flow conditions:

1. Laminar boundary layer with a blunt leading edge without flow trips

2. Turbulent boundary layer with a sharp leading edge with flow trips

A correlation between flat-plate reference conditions at the instrumented dome locations and the free-stream total pressure and total temperature was established in reference 13. This relationship was used to determine reference flat-plate pressures and heating rates for the current test. The boundary-layer probe determined the boundary-layer profile upstream of the quilted dome model.

For many test runs, the model was left in the stream 5 sec to ensure pressure transducer output reached steady state and to obtain temperature time histories from the thermocouple-instrumented heat flux dome. However, during 14 runs the model was left in the test stream for 40 sec to allow the model surface to approach the radiation equilibrium temperature. All test runs were made at an angle of attack of 5° (see fig. 3) to optimize local flow conditions over the flat-plate panel holder.

Data Acquisition and Reduction

Model pressure and temperature and tunnel digital data were recorded on magnetic tape with the on-site 8' HTT digital computer at a rate of 20 samples per second. The magnetic tapes were then sent to the Langley Central Digital Data Recording Subsystem for processing the information to useful engineering units. Model pressure values were selected from the data after steady pressures were established. Unpublished data from a previous test have shown that the pressure gages and the data recording system operate with an error less than 0.25 percent of full scale. The actual absolute error when the gage is operating at the bottom of its scale can be intolerable unless the output is adjusted for the lower range pressures (about 0.1 psi). This is conveniently done in the present tests by adjusting the output of all model gages to match the pressure of a reference precision gage in the test chamber outside the flow prior to model injection, when all pressure orifices are subjected to the same low pressure. As a result, the error is minimized to the effects of gage nonlinearity over a small range, and the maximum expected error is less than about 0.5 percent. The same approach was used with the boundary-layer probe to adjust both static and pitot pressure measurements. Their respective error produced a possible error in Mach number of less than 1.5 percent.

The surface heating rates were calculated from the measured thin-wall temperature time histories by using the one-dimensional transient heat balance equation

$$\dot{q} = \rho C_p \tau \frac{\Delta T}{\Delta t} \quad (1)$$

The temperature-time data were reduced at each time step by using the central difference method to obtain the slope, thus producing a continuous heating-rate history during the entire model exposure. The recorded value of this heating rate was selected immediately after the flow transients associated with the model insertion and before radiation and conduction errors occurred. The model was designed to minimize the inherent uncertainties associated with the thin-wall technique. The dome wall was fabricated from a 0.031-in-thick sheet of AISI 316 stainless steel with the thermocouples spot-welded to the underside of the wall. The uncertainty in the thickness of sheet metal is about ± 2 percent. There were no underside convection losses because the space beneath the dome surface was open and evacuated to a pressure of about 0.1 psia during test exposure. For the present test, the measured underside temperature rise was less than 80°R during test runs; therefore, radiation losses were negligible for this condition where the adiabatic wall temperature was at least 3000°R . The design of the dome also minimized possible conduction losses by reducing the contact area of the thin skin to the base plate at the periphery, and the spatial temperature gradients of the dome interior were not sufficient to cause significant lateral heat conduction. The major error not accounted for in the heating-rate data reduction is probably due to the variation of C_p with temperature. A fixed value of C_p was used in the present data reduction because the actual variation of C_p with temperature is inherently difficult to obtain. Using the fixed value caused an underestimated heating rate which gives an error of between 3 and 10 percent. Overall, the effect of heating-rate errors was minimized by normalizing the data so that both the numerator and the denominator included the same errors which were thereby canceled.

Infrared scanner analog data from the AGA-680 were recorded on-site using a 14-track frequency-modulated (FM) tape recorder at a rate of 16 data frames per second. The FM data tapes were digitized and reduced to temperature contour plots. Each data frame consisted of 70 horizontal scan lines with 120 points per scan line. For the present test, the scanner mapped an area 42×42 in. square. Since a scan line is discretized into 120 points, a discrete temperature was determined for an area of 0.35×0.6 in.

Results and Discussion

The present results consist of laminar- and turbulent-boundary-layer profiles, temperature con-

tours, pressure and heating-rate contours and distribution plots, and integrated pressure and heat load plots. The local flow field over the flat-plate panel holder in terms of Mach number profiles is presented first to characterize the approaching flow. Next, typical temperature contours, reduced from infrared scanner data, are presented and compared with heating-rate contours to provide a qualitative picture of the effect of the flow over the quilted surface on temperature and heating-rate patterns. Typical quantitative pressure contours and distribution plots and heating-rate contours and distribution plots complete the discussion on the effect of the bowed surface on local pressure and heating rate. Although not a fundamental objective of this study, the effect of the longitudinal gaps on transition from laminar flow to turbulent flow over the aligned array is presented because transition caused a significant increase in the heat flux in the vicinity of the gaps. Finally, the integrated pressure and heat loads over the quilted array of bowed domes are compared with their equivalent flat-plate surface levels.

Local Flow Field

The local flow field over the flat-plate panel holder is characterized in this section for the two surface flow conditions of laminar boundary layer with a blunt leading edge (no trips) and turbulent boundary layer with a sharp leading edge (trips). The two local flow conditions of the present tests are characterized by the Mach number profiles tabulated in table III and shown in figure 8. The Mach number was calculated from the ratio of static flat-plate pressure to pitot pressure by using the Rayleigh pitot formula with $\gamma = 1.38$. The profile location for the present test was forward of the dome model insert at $S = 26.2$ in., and the profile locations $S = 58.1$ in. and $S = 89.1$ in., taken from reference 13, are just forward and aft of the instrumented dome locations.

Laminar boundary layer. In figure 8(a), the experimental Mach number data are compared with Mach number profile distributions obtained from a boundary-layer computer program (ref. 17) for the laminar boundary layer. The experimental Mach number profiles at the three locations for the laminar-boundary-layer condition agree with the laminar boundary layers predicted by the methods of reference 17, indicating that a laminar boundary layer is being produced over the flat-plate panel holder. The experimental data shown in figure 8(a) extend beyond the boundary-layer edge into a region of increasing Mach number or decreasing entropy gradient that is produced by the curved bow shock associated with a blunt leading edge. For a given streamline through

a shock, entropy rise is a function of the shock angle or strength through which the streamline passes, so that the highest streamline entropy rise will occur through a normal shock (stagnation streamline) and a lower entropy rise will be produced as the shock angle decreases. Thus, as a flow field develops along the flat plate with a blunt leading edge, an entropy gradient will be produced with higher entropy at the wall and decreasing entropy away from the wall. A further discussion of the entropy gradient caused by a blunt leading edge can be found in reference 18.

Turbulent boundary layer. The boundary-layer computer program of reference 17 was also used to predict the turbulent-boundary-layer case with transition starting at $S = 5$ in. (trip location) and transition ending at $S = 6.25$ in. Computed boundary-layer thicknesses and profiles from the computer program are shown in figure 8(b) for the three profile locations. At the $S = 26.2$ in. location, the computed boundary-layer thickness and Mach number profile deviate slightly from the experimental data; however, at the $S = 58.1$ and 89.1 in. profile locations, the deviation between the computed results and the experimental results becomes greater, possibly because of an inadequate turbulence model used in the computer program. Therefore, the turbulent-boundary-layer thickness with a sharp leading edge was obtained using the Prandtl's power-law expression taken from reference 19:

$$\frac{\delta}{S} \approx 0.37 \text{Re}_s^{-1/5} \quad (2)$$

The resulting boundary-layer thickness calculated by equation (2) agrees with the experimental boundary-layer thickness at the three profile locations as shown in figure 8(b).

The experimental turbulent Mach number profiles shown in figure 8(b) are also compared with profiles derived from an assumed one-seventh-power-law flat-plate turbulent velocity profile taken from reference 20:

$$\frac{u}{u_e} = \left(\frac{z}{\delta}\right)^{1/7} \quad (3)$$

The one-seventh-power-law velocity profile (eq. (3)) was converted to Mach number profiles at the three locations for direct comparison with the experimental results. The velocity-to-Mach-number conversion was based on the definition of Mach number assuming a constant γ :

$$\frac{u}{u_e} = \frac{M\sqrt{T}}{M_e\sqrt{T_e}} \quad (4)$$

Substituting for static temperature by using the isentropic relationship from reference 21, equation (4) can be expressed as

$$\frac{u}{u_e} = \frac{M \sqrt{T_t \left(1 + \frac{\gamma-1}{2} M_e^2\right)}}{M_e \sqrt{T_{t,e} \left(1 + \frac{\gamma-1}{2} M_e^2\right)}} \quad (5)$$

To define the variation in total temperature within the boundary layer, the Crocco relation between total temperature and velocity was used for the present case. This relation is given in reference 22 as

$$\frac{T_t - T_w}{T_{t,e} - T_w} = \frac{u}{u_e} \quad (6)$$

Combining equations (3) and (5), the Mach number variation within the boundary layer is given as

$$M = \left[\frac{\lambda M_e^2}{\left(1 + \frac{\gamma-1}{2} M_e^2\right) - \left(\lambda \frac{\gamma-1}{2} M_e^2\right)} \right]^{1/2} \quad (7)$$

where

$$\lambda = \frac{(z/\delta)^{2/7}}{T_t/T_{t,e}} \quad (8)$$

The total temperature variation in the boundary layer is expressed in terms of known variables by combining equations (3) and (6) to give

$$\frac{T_t}{T_{t,e}} = \left(\frac{z}{\delta}\right)^{1/7} \left(1 - \frac{T_w}{T_{t,e}}\right) + \left(\frac{T_w}{T_{t,e}}\right) \quad (9)$$

Therefore, the predicted Mach number profiles for the turbulent boundary layers shown in figure 8(b) were calculated from equations (7), (8), and (9). The resulting Mach number profiles agree, in general, with the experimental profiles in figure 8(b), but they deviate slightly near the wall. The deviation is attributed to the 0.19-in-diameter flow trips attached near the leading edge. Overall, figure 8(b) indicates that a turbulent boundary layer was produced over the flat-plate panel holder for the sharp leading edge configuration with flow trips.

The laminar and turbulent Mach number profiles shown in figure 8 characterize the undisturbed flow field on the flat-plate panel holder. The undisturbed laminar boundary layer was greater than 0.5 in. at the leading dome of the model and the turbulent boundary layer was greater than 0.6 in. at the leading dome of the model. Hence, all dome heights were submerged within both the laminar and turbulent boundary layers.

Qualitative Temperature and Heating-Rate Patterns

Surface temperature contours, shown in figure 9, were obtained from the AGA-680 infrared scanner for models with all-ceramic domes. The models were oriented in both the aligned and the skewed configurations and were exposed to flow conditions with both laminar and turbulent boundary layers. Heating-rate contours were calculated from the temperature time histories of the thermocouple output of the heat flux domes. The surface temperature contours give a qualitative indication of the local heat flux and flow characteristics on the dome model.

Laminar boundary layer. The temperature distribution for the center row of domes of the aligned array with a laminar boundary layer (see fig. 9(a)) shows peak temperature on the windward side of the leading dome because of flow impingement. However, the temperature peaks on the downstream domes spread laterally outward from the longitudinal centerline and, on the fourth dome, have moved close to the longitudinal edges of the center row of domes because the flow is being channeled through a path of least flow resistance.

Figure 9(b) shows temperature contours for the skewed array with a laminar boundary layer. The temperature contours on the leading domes are similar to those in figure 9(a), but as the flow moves downstream and encounters the alternating surface pattern of the skewed array, it causes two distinct peak temperature regions on the windward side of each downstream dome. As flow is turned by the local surface contour, velocity gradients create vortices that move through the valleys. This same flow phenomenon is evident in the analytical study of reference 12 for laminar flow over the skewed array and indicates that the heating peaks are caused by vortex structures in the boundary layer that increase the temperature gradient at the wall. Note that in figures 9(a) and 9(b) a high temperature gradient exists along the outside longitudinal gaps, indicating the outer longitudinal gaps cause boundary-layer transition to turbulent conditions. This phenomenon will be discussed in detail in a later section.

Temperature and heating-rate contours for a laminar boundary layer are compared at location 4 for the aligned array and location 3 for the skewed array. (See figs. 4(a) and 4(b), respectively.) The comparison shown in figure 10(a) indicates that the flow is two-dimensional with higher heating on the windward side of the dome. Figure 10(b) shows the comparison for the skewed array configuration. The laminar Navier-Stokes prediction given in reference 12 for the skewed array configuration is shown in the

inset in this figure. Although the Navier-Stokes prediction is for a sharp leading edge laminar boundary layer with no entropy gradient outside the boundary layer and a ratio of dome height to boundary-layer thickness of unity, a qualitative comparison shows that predicted vortex-induced peak heating areas are present in both cases. The temperature and heating contours suggest highly three-dimensional flow with the peaks located in the same region.

Turbulent boundary layer. Surface temperature distributions for turbulent-boundary-layer flow over the aligned and skewed array configurations are shown in figures 9(c) and 9(d), respectively, and both exhibit similar temperature contour patterns inferring two-dimensional flow characteristics. The surface temperature is highest on the windward side of the dome and decreases as the flow expands to the leeward side of the dome. The temperature contours are generally oriented in bands perpendicular to the flow with little difference occurring between contours on domes of the same array. Higher momentum of the turbulent flow throughout the boundary layer and a thicker boundary layer make the flow less susceptible to influence by the surface contour and discourage the three-dimensional flow characteristics seen in the laminar cases. These temperature levels and contours are a result of the heating rates that are discussed in the next section.

Figures 10(c) and 10(d) show the comparison between temperature (left side of the figure) and heating rate (right side of the figure) for the aligned and skewed configurations with a turbulent boundary layer. The comparison shows higher temperatures and higher normalized heating rates (\dot{q}/\dot{q}_{fp}) on the windward side of the dome and a heating decrease as the flow expands to the leeward side. In general, lines of constant temperature and heating rates are perpendicular to the streamwise direction for both the aligned and the skewed arrays consistent with two-dimensional flow characteristics with insignificant vortex action as seen with the laminar boundary layer. Also, a comparison between the two configurations with a turbulent boundary layer shows the skewed array has higher peak heating on the windward side.

Quantitative Pressure Distributions

Dome pressures, normalized to the flat-plate reference pressure of each run, are presented in table V for both laminar- and turbulent-boundary-layer flow conditions. The flat-plate reference pressures are presented in table IV. For each configuration, the experimental results shown in figures 11 through 18 are presented first as surface contours and longitudinal

distributions at each height (odd-numbered figures). Then the results are presented as composite longitudinal and lateral distributions with height variation (even-numbered figures). The longitudinal distributions are in the streamwise direction at a constant y/R value of 1, and the lateral distributions are in the crossflow direction at a constant x/R value of 1. (See fig. 5(a).) The surface contours presented in this section and the following sections were generated from experimental data taken at the 59 sensor locations of the instrumented domes by using a contouring routine that is based on a splines-under-tension, curve-fitting process.

Laminar boundary layer. Contour and longitudinal distributions of normalized pressure for the aligned array configuration with a laminar boundary layer are presented in figure 11 for array heights of 0.2 and 0.4 in. The longitudinal 0.05-in. gaps were closed with a ceramic filler for this array configuration to avoid the effects of boundary-layer transition due to open gaps. (Boundary-layer transition due to open gaps is discussed later.) Surface pressure contours for the aligned array with a laminar boundary layer (fig. 11) show higher pressure on the windward side and lower pressure on the leeward for both dome heights. The longitudinal centerline plots (figs. 11 and 12(a)) show an initial compression region (x/R less than 0.6), an expansion region (x/R greater than 0.6 and less than 1.45), and a rearward pressure recovery (x/R greater than 1.45). The normalized pressure distribution calculated by using the 2-D linearized, small-perturbation theory given by reference 23 is also included (see fig. 11(b)) for the highest dome and agrees with the experimental distribution in the expansion region. The small-perturbation theory indicates the surface geometry would cause a continued pressure decrease on the rearward side of the dome. Since the pressure increases in this region, the flow must be separated to account for the pressure recovery. (The occurrence of separated flow is substantiated by decreases in heating, which are shown in a later section.) Predicted forward and rear edge pressures disagree with experimental results because of the velocity gradient through the boundary layer, 3-D effects of the array geometry, and forward and aft weak shock systems associated with flow separation pockets that are not accounted for by the small-perturbation theory. Figure 12(b) is a comparison between the crossflow distributions of the two heights and shows a constant lateral pressure distribution for both heights at a value near the flat-plate reference pressure.

The corresponding surface pressure contours and the longitudinal pressure distributions for the skewed array configuration with a laminar boundary layer

are presented in figure 13 for heights of 0.1, 0.2, and 0.4 in. Again, the windward pressure was higher than the flat-plate value and the leeward pressure was lower than the flat-plate value, as shown in figures 13 and 14(a). Also, as the dome height increases, the pressure gradient in the expansion region increases (fig. 14(a)). The pressure distribution calculated by the 2-D linearized flow theory is shown in figure 13(c), and the slope agrees with the experimental data in the expansion region, indicating an inviscid flow characteristic over the top of the dome. As stated previously, rearward edge pressure recovery indicates local laminar separation is present for x/R greater than 1.5, as was indicated for the aligned array with a laminar boundary layer. Figure 14(b) shows the lateral pressure distributions to be constant for all three heights at about the flat-plate reference pressure.

Turbulent boundary layer. The normalized pressure contours and distributions for turbulent-boundary-layer flow over the aligned array configuration with heights of 0.1, 0.2, and 0.4 in. are shown in figure 15. The figure shows that the surface pressure contours become better defined with height increase because the longitudinal gradient shown in figures 15 and 16(a) increases with dome height increase. Figure 15(c) shows the comparison between experimental pressures and pressures calculated by the 2-D linearized flow theory. Note that the slopes nearly agree in the expansion region, but the experimental pressure is higher—an effect possibly due to a stronger forward shock system than that for the laminar case and greater flow displacement caused by the array of domes raised above the normal test surface. Figure 16(a) gives the longitudinal pressure distributions for the three dome heights and shows an initial windward compression region for all heights. However, there is no rearward edge pressure recovery, as seen in the laminar cases, because turbulent-boundary-layer separation is less likely to occur than laminar-boundary-layer separation. The lateral pressure distributions in figure 16(b) show a constant crossflow pressure distribution at the dome centerline that is about 10 percent higher than the flat-plate reference pressure. In this case, the induced pressure increased with dome height since the effective flat-plate angle of attack increased as dome height increased.

Figure 17 shows the pressure contours and longitudinal centerline plots for the skewed array with a turbulent boundary layer. The contours for the 0.1-in. height show a region of peak pressure on the windward side, and, as the height increases, the peak pressure moves more toward the forward edge of the dome. The isobars for all three heights of this con-

figuration are more noticeably concave to the flow direction than those observed for the laminar boundary layer. The pressure predicted by 2-D linearized flow theory, shown in figure 17(c), is in agreement with the slope of the experimental pressure measurements, but the experimental pressure distribution is about 15 percent higher than the predicted value. A comparison at the 0.4-in. height between the aligned and skewed configurations (see figs. 15(c) and 17(c), respectively) shows that the slope and level of the experimental pressures in the expansion regions agree. However, the longitudinal plot for the aligned configuration (fig. 15(c)) shows that forward compression occurred up to the second windward instrument location (location 2, see fig. 5(b)) on the dome and that for the skewed configuration (fig. 17(c)) the forward compression occurred before the first windward instrument location (location 10, see fig. 5). This difference is possibly because the skewed configuration allows the compression to take place over the longer windward perimeter, giving a greater 3-D relief than the aligned configuration. The longitudinal pressure distributions in figure 18(a) show a linear decrease in dome surface pressure for all heights except at the peak pressure region for the 0.1-in.-high dome and show that as dome height increases, the pressure gradient increases. The lateral distributions (fig. 18(b)) for all heights show the lateral edge pressure at the flat-plate reference level, but the distributions curve to a maximum value 10 to 15 percent above the reference pressure at the dome center ($y/R = 1.0$).

Quantitative Heating-Rate Distributions

Dome heating rates, calculated from temperature rise rates and normalized to the flat-plate reference heating rate for each run, are presented in table VI for both boundary-layer flow conditions. The flat-plate reference heating rates are given in table IV. The experimental heating rates given in figures 19 through 26 are presented in the same manner as the experimental pressures in the preceding section.

Laminar boundary layer. Figure 19 shows surface heating-rate contours and longitudinal distributions for the aligned array configuration with a laminar boundary layer for heights of 0.2 and 0.4 in. The longitudinal 0.05-in. gaps were closed with a ceramic filler for this array configuration to avoid the effects of boundary-layer transition due to open gaps. (Boundary-layer transition due to open gaps is discussed in the next section.) The contours and distribution plots for the 0.2-in. height (fig. 19(a)) show a heating-rate increase between 1.2 and 1.3 times the flat-plate value over most of the dome surface. Contours on the 0.4-in.-high dome, which show peak

heating on the windward side, are closely spaced and illustrate an increased heating-rate gradient with increasing dome height. The longitudinal distribution of figure 19(b) shows that forward and rearward edge heating falls below the flat-plate reference value at x/R less than 0.45 and x/R greater than 1.5. The corresponding pressure distribution (fig. 11(b)) for the same regions shows pressure recovery, and the combination of recovering pressure and lower heating indicates forward and rearward flow separation. The longitudinal and lateral centerline heating-rate distributions for the two heights are given in figure 20. In the longitudinal distribution (fig. 20(a)), the heat flux distribution for the 0.4-in.-high dome shows decreased heating on the crest with the windward peak higher than the leeward peak. The leeward peak may be caused by local boundary-layer transitional effects as was noted in similar results from the tests of a single dome given in reference 13. The distributions shown in figure 20(b) are fairly constant across the lateral centerline with heating levels of about 1.5 for the 0.4-in. height and 1.25 for the 0.2-in. height.

Normalized heating-rate contours and longitudinal distributions are shown in figure 21 for the skewed array with a laminar boundary layer and dome heights of 0.1, 0.2, and 0.4 in. The contours for the 0.1-in. height show no distinct peak heating regions; however, as the height increases (figs. 21(b) and (c)) two distinct windward peak heating regions can be seen on either side of the longitudinal centerline. As discussed previously, these peak heating regions are due to three-dimensional vortices in the laminar boundary layer created as the flow passes over the skewed array configuration. The existence of the vortices has been shown analytically in reference 12. For the highest dome tested (fig. 21(c)), the surface contours show the vortex-induced peak heating is above 2.7 times the flat-plate reference heating level. The longitudinal centerline plot shows a region on the forward edge of the dome (x/R less than 0.4) where the heating level falls below unity, indicating a slight forward flow separation. The heating rate in the rearward separation region (see fig. 13(c)) was affected by the local flow transition producing higher heating rates near the trailing edge than occurred in the rearward separation region for the aligned array with a laminar boundary layer. Detailed discussions on laminar separation with boundary-layer transitional effects are presented in reference 24 for a larger scale wing-cove-elevon model that was tested in the 8' HTT. The localized separation trends of the present laminar results are consistent with the results of reference 24. Therefore, even though the pressure in the separation region increased (see fig. 13(c)), the corresponding heating can either decrease or

increase, depending on boundary-layer transitional effects.

Figure 22 shows the longitudinal and lateral centerline distributions for the three heights. The longitudinal plots in figure 22(a) show that as height is increased, the maximum heating level on the longitudinal centerline increases to nearly twice the flat-plate value for the highest dome. Surface effects of the three-dimensional vortical flow discussed above and shown in figure 21 are also shown on the lateral distributions of figure 22(b). The two peak heating regions centered at $y/R = 0.5$ and 1.5 become more evident and increase to a higher level with increasing dome height. The strength of the vortical flow should be expected to increase with an increase in dome height because larger velocity and pressure gradients are produced by larger surface protuberances. A comparison between figures 22 and 20 shows that the skewed array has a higher heating level on the longitudinal centerline, a higher peak heating occurring symmetrically off-center, and a more complex surface-heating pattern than the aligned array.

Turbulent boundary layer. Normalized heating-rate contours and longitudinal distributions for the aligned array with a turbulent boundary layer are shown in figure 23. The 0.1-in.-high dome has a defined peak heating region on the windward side; however, the 0.2- and 0.4-in. heights have a peak heating line perpendicular to the flow direction. For all three heights, the normalized heating level is above 1 on the windward side and decreases linearly to below 1 on the leeward side, as shown in figures 23 and 24(a). Also, as the height increases, peak heating level and heating-rate gradient increase. The lateral distributions in figure 24(b) show that for all three heights, heating across the lateral centerline is nearly constant and varies from the flat-plate level to 1.1 times the flat-plate level. In contrast to results from the aligned array in a laminar boundary layer (fig. 19), the contours shown in figure 23 for the aligned array with a turbulent boundary layer indicate that heating results from a two-dimensional flow pattern although the surface is three-dimensional.

Figure 25 shows contours and longitudinal centerline distributions of normalized heating rate for the skewed array configuration with a turbulent boundary layer. The contours shown in figure 25 indicate heating characteristics of two-dimensional flow, as did the contours for the aligned configuration with a turbulent boundary layer, which results in similar heating patterns on the dome surface. (Compare fig. 25 with fig. 23.) Other similarities between the aligned and skewed arrays with a turbulent boundary layer are shown by comparing figures 26 and 24. The peak heating level and heating-rate gradient on

the longitudinal centerline increase with dome height, and the heating on the lateral centerline is constant at about 1.1 times the flat-plate value for all three dome heights of the skewed array. The increased heating is attributed to the flow displacement caused by the array of domes protruding above the normal test surface.

Longitudinal Gap Effects

All array configurations were tested with a clearance gap of less than 0.05 in. between individual domes to facilitate array changes. However, when the aligned array was exposed to flow with a laminar boundary layer, excessive heating was present along the dome longitudinal edges. To isolate the cause of the excessive edge heating, the longitudinal gaps were closed with a ceramic filler. Subsequent tests on the aligned array with a laminar boundary layer did not show high longitudinal-edge heating. Experimental pressures and heating rates for laminar-boundary-layer flow over the aligned array with and without the longitudinal gaps are presented in this section. Pressure distributions for dome heights of 0.1, 0.2, and 0.4 in. with open longitudinal gaps are shown in figure 27. Comparison of the pressure contours shows, as previously shown in figures 11 and 12(b), that as dome height increases, the streamwise pressure gradient increases, and the lateral centerline crossflow distributions are nearly constant across the dome. However, the heating rates shown in figure 28 for the same conditions show that as the height increases, the heating increases drastically along the longitudinal edges. The fact that no pressure increase exists near the gaps where heating is high means that heating is caused by boundary-layer transition to turbulent.

Figures 29 and 30 give pressure and heating rate comparisons between the 0.4-in-high domes for the following cases indicated in the figures:

- (a) Filled longitudinal gaps
- (b) Port longitudinal gap filled and starboard gap open
- (c) Open longitudinal gaps

Figure 29 shows little effect on the surface pressure between the three cases, but figure 30 shows a significant effect on the surface heating. The contour plots of figure 30 show that with filled longitudinal gaps, dome heating peaks on the windward side at about 1.65 times the flat-plate reference value. However, with open longitudinal gaps (fig. 30(c)), heating peaks along the forward longitudinal edge at about 5 times the laminar flat-plate value and approaches the turbulent heating level. The lateral plots given in figure 30 show a constant heating at 1.5 times the

flat-plate reference value when the gaps were filled, but when the gaps were open, excessive edge heating near the turbulent level is present. High heating was due to boundary-layer transition because no pressure increase occurred near the longitudinal gaps.

Total Integrated Loads on the Instrumented Domes

The pressure and heating rate distributions obtained during these tests form a data base to be used in assessing the aerothermal load increase on multiple dome protuberances in a quilted array. The increased pressure and heating, normalized to the flat-plate value, were computed and are presented in this section.

Pressure and heat load increase. Shown as figure 31 are plots of total integrated pressure and heat loads normalized to the flat-plate value on the instrumented domes. Results are given for various dome heights, aligned and skewed arrays, and laminar and turbulent boundary layers. The pressure and heat loads, respectively, were obtained using the following equations:

$$\frac{P}{P_{fp}} = \frac{\sum_{n=1}^N p_n A_{xy_n}}{p_{fp} A_{xy}} \quad (10)$$

and

$$\frac{Q}{Q_{fp}} = \frac{\sum_{n=1}^N \dot{q}_n A_{xy_n}}{\dot{q}_{fp} A_{xy}} \quad (11)$$

Figure 31(a) shows the total increase in pressure load for all cases to be less than 10 percent above the flat-plate level for the lowest domes and no greater than 15 percent above the flat-plate pressure for the highest domes. As indicated earlier, turbulent surface pressures were generally higher than flat-plate values because of greater flow displacement than the laminar case. Shown in figure 31(b) are the normalized total integrated heat loads. The arrays tested in a turbulent boundary layer show a heat load increase less than 8 percent above the turbulent flat-plate level. All arrays with the lowest dome heights that were tested in a laminar boundary layer show a heat load increase to be less than 15 percent above the flat-plate laminar level. The arrays with a laminar boundary layer show a greater heat load increase as dome height is increased. The skewed array with a laminar boundary layer has the greatest heat load increase to about 75 percent above the flat-plate heating for the 0.4-in-high dome. The aligned array with a laminar boundary layer has a

heat load increase of 33 percent, but with a turbulent boundary layer the increase is only 5 percent above the flat-plate heating level for the highest dome. The increased heat load for the laminar-boundary-layer condition is probably due to local transitional effects and local flow vorticity effects, especially for the skewed array. Flow over the quilted configuration has a greater effect on heat loads than on pressure loads.

Pressure drag. The pressure drag coefficient, plotted in figure 32(a), was calculated by dividing the pressure drag force F_P over the dome by the local dynamic pressure, i.e.,

$$C_{D,P} = \frac{F_P}{\frac{1}{2}(\rho u^2)_e A_{xy}} \quad (12)$$

where

$$F_P = \sum_{n=1}^N p_n A_{yzn} \quad (13)$$

The ticked symbol shown in figure 32 is data from the 0.1-in-high dome in the aligned array with open longitudinal gaps; therefore, the data may be subject to gap effect errors. Figure 32(a) shows that the calculated pressure drag coefficient for the skewed array in either a laminar or a turbulent boundary layer increased about two orders of magnitude as the dome height increased. However, for the aligned array in either boundary-layer type, the pressure drag coefficient increased only about one order of magnitude as the dome height increased.

Figure 32(b) shows the pressure drag coefficient normalized to the local flat-plate skin-friction coefficient to give an indication of the magnitude of the pressure drag coefficient. The local flat-plate skin-friction coefficient was obtained by using methods described in reference 25. The method is as follows. Local Reynolds number Re^* and Prandtl number N_{Pr}^* are calculated at Eckert's reference temperature T^* , where

$$T^* = 0.22T_{aw} + 0.28T_e + 0.5T_w \quad (14)$$

and

$$T_{aw} = T_e + (T_t - T_e)N_{Pr}^r \quad (15)$$

$r = 1/2$ for a laminar boundary layer

$r = 1/3$ for a turbulent boundary layer

Local Stanton number N_{St}^* based on Eckert's reference temperature is calculated by using the following relationships for laminar and turbulent boundary layers, respectively:

$$N_{St}^* = 0.332N_{Pr}^{*-2/3}Re^{*-1/2} \quad (16)$$

$$N_{St}^* = 0.030N_{Pr}^{*-2/5}Re^{*-1/5} \quad (17)$$

The local flat-plate skin-friction coefficient is then obtained by using Reynolds analogy:

$$C_{\tau,fp} = 2N_{St}^* \quad (18)$$

Figure 32(b) shows the increase in pressure drag coefficient for an array of protuberances bowing outward, normalized to the calculated flat-plate skin-friction coefficient. Results from aligned and skewed array configurations with a laminar boundary layer show pressure drag to be the same order of magnitude as the flat-plate skin friction for the highest domes tested. However, at the lowest dome height (the design height of bowed TPS tiles) with a laminar boundary layer, pressure drag for the aligned array is one order of magnitude below flat-plate skin-friction drag, and pressure drag for the skewed array is two orders of magnitude below that for flat-plate skin friction. For both array configurations in a turbulent boundary layer, pressure drag at the highest dome is one order of magnitude below that for flat-plate skin friction, and pressure drag at the lower height is less than two orders of magnitude below that for the flat-plate skin friction. Although the actual dome skin friction was not measured, figure 32(b) does indicate that pressure drag is insignificant for the domes at the designed bowed height of 0.1 in.

Effect of dome position in the array. Figure 33 shows the normalized integrated heat load over the 0.4-in-high heat flux dome located at various positions in the array as indicated in the tables to the right of the plots. Figure 33(a) shows that as the flow moves downstream, the integrated heat load over the aligned array with a laminar or turbulent boundary layer decreases. The heating decreases more for the turbulent boundary layer than for the laminar boundary layer; however, a heating decrease with increased distance from the leading dome for a laminar boundary layer indicates the boundary layer is not in transition. Shown in figure 33(b) are the dome position effects for the skewed array with laminar and turbulent boundary layers. This figure shows decreased heating on the skewed array in a turbulent boundary layer as the flow moves downstream; however, the skewed array in a laminar boundary layer had increased heating with increased distance from

the leading dome because of boundary-layer transition and vorticity. Thus, the general heating trend on an array of domes for a fixed boundary-layer condition decreases with distance from the leading dome, but the skewed array is more sensitive to transition from a laminar to a turbulent boundary layer.

Concluding Remarks

Aerothermal tests were conducted in the NASA Langley 8-Foot High-Temperature Tunnel (8' HTT) at a Mach number of 6.5 on simulated arrays of bowed 9.9- × 9.9-in. square metallic tiles mounted on a flat-plate test apparatus at an angle of attack of 5°. Detailed surface pressures and heating rates were obtained for arrays aligned with the flow and skewed 45° diagonally to the flow with nominal bowed heights of 0.1, 0.2, and 0.4 in. submerged in both laminar and turbulent boundary layers. The 9.9- × 9.9-in. simulated tile with a bowed height of 0.1 in. is representative of a thermally bowed metallic thermal protection system (TPS) tile. Aerothermal tests were made at a nominal total temperature of 3300°R, a total pressure of 400 psia, a total enthalpy of 950 Btu/lbm, a dynamic pressure of 2.7 psi, and a unit Reynolds number of 0.4×10^6 per foot. The experimental results form a data base that can be used to help predict aerothermal load increases from bowed arrays of TPS tiles.

The present results indicate that surface heating for the aligned array with a laminar boundary layer showed two-dimensional flow characteristics with peak heating just forward of the dome center; however, heating for the skewed array with a laminar boundary layer showed three-dimensional effects of vortical flow similar to results given by Navier-Stokes analysis. Heating for both aligned and skewed arrays with a turbulent boundary layer showed two-dimensional flow characteristics with higher heating on the windward surface. Pressures were increased on the windward surface and reduced on the leeward surface as predicted by linearized small-perturbation theory, and the distributions were only moderately affected by surface and boundary-layer variations. Generally, the small gaps between domes did not affect the pressure and heating distributions, but the longitudinal gaps of the aligned array with a laminar boundary layer caused flow transition and excessive heating. Heating decreased with increasing distance from the leading dome for the aligned array with a laminar boundary layer and for both the aligned array and the skewed array with a turbulent boundary layer for the highest domes tested; however, heating increased with increasing distance from the leading dome for the skewed array with a laminar boundary

layer because of boundary-layer transition and vorticity. At the 0.1-in. height, representative of a bowed metallic TPS tile, the integrated heat load over the dome increased less than 15 percent, and the pressure drag was at least an order of magnitude less than the calculated flat-plate skin friction.

NASA Langley Research Center
Hampton, VA 23665-5225
March 7, 1988

References

1. Strouhal, George; and Tillian, Donald J.: Testing the Shuttle Heat-Protection Armor. *Astronaut. & Aeronaut.*, vol. 14, no. 1, Jan. 1976, pp. 57-65.
2. Bohon, Herman L.; Sawyer, J. Wayne; Hunt, L. Roane; and Weinstein, Irving: Performance of Full Size Metallic and RSI Thermal Protection Systems in a Mach 7 Environment. AIAA-75-800, May 1975.
3. Bohon, Herman L.; Shideler, John L.; and Rummmler, Donald R.: Radiative Metallic Thermal Protection Systems. A Status Report. *J. Spacecr. & Rockets*, vol. 14, no. 10, Oct. 1977, pp. 626-631.
4. Shideler, John L.; Webb, Granville L.; and Pittman, Claud M.: Verification Tests of Durable Thermal Protection System Concepts. *J. Spacecr. & Rockets*, vol. 22, no. 6, Nov.-Dec. 1985, pp. 598-604.
5. Sawyer, James Wayne.: *Pressure and Heating-Rate Distributions on a Corrugated Surface in a Supersonic Turbulent Boundary Layer*. NASA TP-1024, 1977.
6. Jackson, L. Robert; and Dixon, Sidney C.: *A Design Assessment of Multiwall, Metallic Stand-Off, and RSI Reusable Thermal Protection Systems Including Space Shuttle Application*. NASA TM-81780, 1980.
7. Kelly, H. Neale; and Webb, Granville L.: Assessment of Alternate Thermal Protection Systems for the Space Shuttle Orbiter. AIAA-82-0899, June 1982.
8. Polak, A.; Werle, M. J.; Vatsa, V. N.; and Bertke, S. D.: Numerical Study of Separated Laminar Boundary Layers Over Multiple Sine-Wave Protuberances. *J. Spacecr. & Rockets*, vol. 13, no. 3, Mar. 1976, pp. 168-173.
9. Yates, John E.: *Linearized Integral Theory of the Viscous Compressible Flow Past a Wavy Wall*. AFOSR-TR-72-1335, U.S. Air Force, July 1972. (Available from DTIC as AD 746 332.)
10. Brandon, H. J.; and Masek, R. V.: *Measurement and Correlation of Aerodynamic Heating to Surface Corrugation Stiffened Structures in Thick Turbulent Boundary Layers*. NASA CR-132503, [1974].
11. Olsen, George C.; and Smith, R. E.: Analysis of Aerothermal Loads on Spherical Dome Protuberances. AIAA-83-1557, June 1983.
12. Olsen, George C.; and Smith, R. E.: Aerothermal Loads Analysis for High Speed Flow Over a Quilted Surface Configuration. AIAA-84-1630, June 1984.
13. Glass, Christopher E.; and Hunt, L. Roane: *Aerothermal Tests of Spherical Dome Protuberances on a Flat Plate at a Mach Number of 6.5*. NASA TP-2631, 1986.

14. Deveikis, William D.; and Hunt, L. Roane: *Loading and Heating of a Large Flat Plate at Mach 7 in the Langley 8-Foot High-Temperature Structures Tunnel*. NASA TN D-7275, 1973.
15. Deveikis, William D.; Bruce, Walter E., Jr.; and Karnes, John R.: *Techniques for Aerothermal Tests of Large, Flightweight Thermal Protection Panels in a Mach 7 Wind Tunnel*. NASA TM X-71983, 1974.
16. Leyhe, E. W.; and Howell, R. R.: *Calculation Procedure for Thermodynamic, Transport, and Flow Properties of the Combustion Products of a Hydrocarbon Fuel Mixture Burned in Air With Results for Ethylene-Air and Methane-Air Mixtures*. NASA TN D-914, 1962.
17. Harris, Julius E.; and Blanchard, Doris K.: *Computer Program for Solving Laminar, Transitional, or Turbulent Compressible Boundary-Layer Equations for Two-Dimensional and Axisymmetric Flow*. NASA TM-83207, 1982.
18. Ferri, Antonio: Some Heat Transfer Problems in Hypersonic Flow. *Aeronautics and Astronautics*, Nicholas John Hoff and Walter Guido Vincenti, eds., Pergamon Press, Inc., 1960, pp. 344-377.
19. White, Frank M.: *Viscous Fluid Flow*. McGraw-Hill, Inc., c.1974.
20. Schlichting, Hermann (J. Kestin, transl.): *Boundary-Layer Theory*, Seventh ed. McGraw-Hill Book Co., c.1979.
21. Ames Research Staff: *Equations, Tables, and Charts for Compressible Flow*. NACA Rep. 1135, 1953. (Supersedes NACA TN 1428.)
22. Bushnell, Dennis M.; Johnson, Charles B.; Harvey, William D.; and Feller, William V.: *Comparison of Prediction Methods and Studies of Relaxation in Hypersonic Turbulent Nozzle-Wall Boundary Layers*. NASA TN D-5433, 1969.
23. Anderson, John D., Jr.: *Modern Compressible Flow—With Historical Perspective*. McGraw-Hill, Inc., c.1982.
24. Deveikis, William D.: *Effects of Flow Separation and Cove Leakage on Pressure and Heat-Transfer Distributions Along a Wing-Cove-Elevon Configuration at Mach 6.9*. NASA TP-2127, 1983.
25. Kays, W. M.; and Crawford, M. E.: *Convective Heat and Mass Transfer*, Second ed. McGraw-Hill, Inc., c.1980.

Table I. Quilted Dome Model Configurations and Heights H Above Flat Plate
[Dimensions given in inches]

(a) Laminar boundary layer with blunt leading edge

Run	Nominal height	Actual height				Instrumented dome location*			Gap*	Time, sec
		H1	H2	H3	H4	2	3	4		
Aligned array										
†1	0.4	0.427	0.450	0.472	0.469	C	C	C	O	5
2	.4	.423	.421	.486	.491	C	P	T	O	5
3	.4	.430	.456	.524	.499	C	T	P	O	5
4	.2	.279	.288	.299	.324	C	P	T	O	5
5	.1	.182	.180	.189	.202	C	P	T	O	5
6	.4	.427	.450	.472	.469	C	C	C	O	40
7	.2	.289	.296	.325	.323	C	C	C	O	40
8	.1	.161	.174	.187	.185	C	C	C	O	40
9	.4	.429	.448	.488	.461	C	P	T	PF	5
10	.4	.429	.448	.488	.461	C	P	T	F	5
11	.2	.266	.276	.300	.312	C	P	T	F	5
12	.4	.429	.448	.478	.449	C	C	C	F	40
13	.2	.271	.286	.361	.287	C	C	C	F	40
Skewed array										
‡14	0.4	0.437	0.487	0.486	0.430	P	T	C	O	5
15	.4	.119	.489	.490	.424	P	T	C	O	5
16	.4	.121	.506	.468	.426	T	P	C	O	5
17	.2	.123	.327	.342	.272	P	T	C	O	5
18	.1	.105	.186	.215	.157	P	T	C	O	5
19	.4	.140	.470	.466	.448	C	C	C	O	40
20	.2	.133	.321	.327	.282	C	C	C	O	40
21	.1	.104	.185	.187	.144	C	C	C	O	40

*Abbreviations in table I:

- C ceramic dome
- F filled longitudinal gaps
- O open longitudinal gaps
- P pressure dome
- PF port gap filled and starboard gap open
- T heat flux dome

[†]Define local flow field with boundary-layer probe.

[‡]Configuration C (see fig. 4(c)).

Table I. Concluded

(b) Turbulent boundary layer with sharp leading edge

Run	Nominal height	Actual height				Instrumented dome location*			Gap*	Time, sec
		H1	H2	H3	H4	2	3	4		
Aligned array										
†22	0.4	0.427	0.450	0.472	0.469	C	C	C	O	5
23	.4	.466	.478	.482	.491	C	P	T	O	5
24	.2	.286	.284	.291	.327	C	P	T	O	5
25	.1	.181	.187	.213	.208	C	P	T	O	5
26	.4	.427	.450	.472	.469	C	C	C	O	40
27	.2	.289	.296	.325	.323	C	C	C	O	40
28	.1	.161	.174	.187	.185	C	C	C	O	40
Skewed array										
†29	0.4	0.436	0.481	0.487	0.428	P	T	C	O	5
30	.4	.138	.487	.489	.454	P	T	C	O	5
31	.4	.121	.506	.468	.426	T	P	C	O	5
32	.2	.130	.312	.336	.266	P	T	C	O	5
33	.1	.105	.186	.215	.157	P	T	C	O	5
34	.4	.140	.470	.466	.448	C	C	C	O	40
35	.2	.133	.321	.327	.282	C	C	C	O	40
36	.1	.095	.180	.179	.161	C	C	C	O	40

*Abbreviations in table I:

- C ceramic dome
- F filled longitudinal gaps
- O open longitudinal gaps
- P pressure dome
- PF port gap filled and starboard gap open
- T heat flux dome

†Define local flow field with boundary-layer probe.

‡Configuration C (see fig. 4(c)).

Table II. Instrumentation Locations for Both Pressure- and Thermocouple-Instrumented Domes

Location	θ , deg	r/R	Location	θ , deg	r/R
1	0	0.629	31	135.0	0.157
2	↓	.471	32	157.5	.629
3	↓	.314	33	↓	.471
4	↓	.157	34	↓	.314
5	↓	0	35	↓	.157
6	22.5	.629	36	180.0	.629
7	↓	.471	37	↓	.471
8	↓	.314	38	↓	.314
9	↓	.157	39	↓	.157
10	45.0	.786	40	202.5	.629
11	↓	.629	41	↓	.471
12	↓	.471	42	↓	.314
13	↓	.314	43	↓	.157
14	↓	.157	44	225.0	.786
15	67.5	.629	45	↓	.629
16	↓	.471	46	↓	.471
17	↓	.314	47	↓	.314
18	↓	.157	48	↓	.157
19	90.0	.629	49	270.0	.629
20	↓	.471	50	270.0	.314
21	↓	.314	51	292.5	.629
22	↓	.159	52	292.5	.314
23	112.5	.629	53	315.0	.786
24	↓	.471	54	↓	.629
25	↓	.314	55	↓	.471
26	↓	.157	56	↓	.314
27	135.0	.786	57	↓	.157
28	↓	.629	58	337.5	.629
29	↓	.471	59	337.5	.314
30	↓	.314			

Table III. Mach Number Obtained From Boundary-Layer Probe

Laminar (run 1)		Turbulent (run 22)	
Pressure orifice height, Z , in.	Mach number	Pressure orifice height, Z , in.	Mach number
0.032		0.032	1.994
.096	1.226	.096	3.725
.196	1.964	.205	3.952
.324	2.612	.321	4.502
.442	2.802	.445	5.169
.578	2.826	.582	5.692
.712	2.896	.712	5.849
.962	3.142	.964	5.781
1.159	3.411	1.163	5.786
1.468	3.746	1.470	5.815
2.017	4.443	2.021	5.837
2.503	5.010	2.471	5.732

Table IV. Free-Stream Flow and Flat-Plate Reference Values ($\alpha = 5^\circ$)

Run	$T_{t,\infty}$, °R	T_∞ , °R	$p_{t,\infty}$, psia	p_∞ , psia	$Re \times 10^{-6}$, ft ⁻¹	M_∞	V_∞ , ft/s	$\rho_\infty \times 10^3$, lbm/ft ³	p_{ip} , psia	p_{fp} , psia	\dot{q}_{fp} , Btu ft ² -s	\dot{q}_{fp} , Btu ft ² -s
Laminar boundary layer, blunt leading edge												
1	3287	419	402	0.096	0.430	6.53	6603	0.598		0.1843		0.636
Aligned array												
2	3195	405	385	0.095	0.448	6.50	6468	0.618	0.1874	0.1830	0.790	0.605
3	3256	414	397	.096	.437	6.52	6557	.606	.1882	.1843	.851	.626
4	3187	403	381	.095	.446	6.50	6457	.615	.1964	.1817	.719	.599
5	3348	428	411	.095	.416	6.54	6693	.580	.2028	.1843	.789	.654
6	3183	403	383	.096	.450	6.50	6450	.621	.1852	.1830	.770	.602
7	3197	405	385	.095	.447	6.50	6470	.616	.1982	.1824	.703	.605
8	3271	416	394	.094	.428	6.52	6580	.594	.1806	.1817	.778	.626
9	3267	416	396	.095	.432	6.52	6574	.599	.1972	.1830	.660	.626
10	3390	435	422	.096	.412	6.55	6756	.576	.1933	.1863	.681	.666
11	3244	412	391	.095	.435	6.52	6540	.602	.1930	.1824	.637	.617
12	3202	406	383	.095	.442	6.51	6478	.611	.1929	.1817	.652	.605
13	3467	447	438	.096	.398	6.57	6870	.560	.1922	.1870	.724	.688
Skewed array												
14	3266	415	395	0.095	0.431	6.52	6572	0.598	0.1976	0.1830	0.698	0.626
15	3269	416	397	.095	.432	6.52	6577	.599	.1880	.1837	.674	.626
16	3127	394	372	.095	.459	6.49	6370	.631	.1983	.1811	.688	.583
17	3262	415	392	.094	.430	6.52	6565	.596	.1916	.1817	.660	.623
18	3379	433	419	.095	.413	6.55	6740	.577	.1957	.1856	.722	.663
19	3308	422	405	.095	.426	6.53	6633	.592	.2024	.1843	.752	.642
20	3302	421	400	.094	.423	6.53	6624	.587	.1980	.1824	.676	.636
21	3340	427	409	.095	.418	6.54	6681	.582	.1971	.1837	.690	.651

Table IV. Concluded

Run	$T_{t,\infty}$, °R	T_{∞} , °R	$p_{t,\infty}$, psia	p_{∞} , psia	$Re \times 10^{-6}$, ft^{-1}	M_{∞}	V_{∞} , ft/s	$\rho_{\infty} \times 10^3$, lbm/ft ³	p_{ip} , psia	p_{fp} , psia	\dot{q}_{ip} , $\frac{Btu}{ft^2 \cdot s}$	\dot{q}_{fp} , $\frac{Btu}{ft^2 \cdot s}$
Turbulent boundary layer, sharp leading edge												
22	3257	414	398	0.096	0.438	6.52	6558	0.606		0.1863		3.366
Aligned array												
23	3337	427	409	0.095	0.418	6.54	6677	0.583	0.1967	0.1856	5.629	3.498
24	3306	422	404	.095	.425	6.53	6631	.591	.2022	.1863	5.741	3.449
25	3272	416	400	.096	.434	6.52	6581	.602	.2074	.1870	5.618	3.383
26	3292	419	402	.095	.428	6.53	6609	.595	.1906	.1856	5.704	3.416
27	3407	438	426	.096	.409	6.56	6781	.573	.1974	.1883	6.130	3.614
28	3271	416	397	.095	.431	6.52	6579	.598	.2054	.1850	5.749	3.366
Skewed array												
29	3273	416	396	0.095	0.429	6.52	6582	0.595	0.2120	0.1843	5.323	3.366
30	3482	450	467	.101	.419	6.57	6893	.589	.2090	.2002	5.953	3.828
31	3372	432	419	.096	.416	6.55	6729	.580	.2035	.1883	5.659	3.564
32	3310	422	401	.094	.420	6.53	6637	.584	.2029	.1843	5.501	3.432
33	3318	423	405	.095	.422	6.53	6648	.588	.2010	.1856	5.471	3.465
34	3276	417	394	.094	.426	6.52	6586	.591	.1998	.1837	5.451	3.366
35	3299	420	400	.095	.424	6.53	6620	.588	.1959	.1843	5.444	3.416
36	3436	442	426	.095	.399	6.56	6824	.559	.2001	.1863	5.679	3.630

Table V. Pressure Values From the Pressure Instrumented Dome

Run	$\frac{p_1}{p_{fp}}$	$\frac{p_2}{p_{fp}}$	$\frac{p_3}{p_{fp}}$	$\frac{p_4}{p_{fp}}$	$\frac{p_5}{p_{fp}}$	$\frac{p_6}{p_{fp}}$	$\frac{p_7}{p_{fp}}$	$\frac{p_8}{p_{fp}}$	$\frac{p_9}{p_{fp}}$	$\frac{p_{10}}{p_{fp}}$	$\frac{p_{11}}{p_{fp}}$	$\frac{p_{12}}{p_{fp}}$
Laminar boundary layer, blunt leading edge												
Aligned array												
2	1.126	1.193	1.172	1.098	1.037	1.118	1.191	1.155	1.073	1.164	1.174	1.158
3	1.100	1.163	1.115	1.068	.998	1.099	1.173	1.134	1.018	1.149	1.149	1.120
4	1.114	1.148	1.112	1.111	1.056	1.088	1.161	1.097	1.084	1.129	1.174	1.092
5	1.115	1.119	1.104	1.092	1.047	1.096	1.127	1.114	1.057	1.096	1.134	1.109
9	1.207	1.242	1.221	1.136	1.078	1.178	1.245	1.181	1.110	1.218	1.206	1.177
10	1.098	1.148	1.140	1.058	1.002	1.115	1.138	1.086	1.031	1.125	1.150	1.135
11	1.082	1.132	1.134	1.057	1.068	1.084	1.130	1.113	1.040	1.106	1.161	1.088
Skewed array												
14	1.219	1.220	1.143	1.132	1.075	1.200	1.230	1.167	1.095	1.205	1.218	1.233
15	1.155	1.200	1.131	1.094	1.063	1.218	1.220	1.177	1.063	1.261	1.263	1.210
16	1.231	1.220	1.173	1.120	1.109	1.249	1.252	1.218	1.107	1.219	1.264	1.228
17	1.139	1.136	1.068	1.065	.990	1.137	1.161	1.115	1.037	1.170	1.164	1.151
18	.987	1.035	.985	.982	.981	1.005	1.054	1.048	.953	1.062	1.064	1.014
Turbulent boundary layer, sharp leading edge												
Aligned array												
23	1.264	1.312	1.255	1.197	1.116	1.262	1.284	1.243	1.156	1.326	1.317	1.258
24	1.135	1.206	1.155	1.135	1.115	1.135	1.177	1.157	1.105	1.184	1.206	1.161
25	1.130	1.153	1.087	1.082	1.050	1.095	1.144	1.055	1.050	1.152	1.110	1.140
Skewed array												
29	1.366	1.390	1.366	1.261	1.185	1.436	1.448	1.348	1.252	1.494	1.484	1.451
30	1.286	1.353	1.311	1.215	1.147	1.442	1.482	1.376	1.228	1.692	1.611	1.482
31	1.202	1.236	1.187	1.146	1.075	1.321	1.338	1.243	1.135	1.411	1.412	1.326
32	1.179	1.253	1.238	1.202	1.173	1.271	1.340	1.224	1.176	1.417	1.380	1.325
33	1.130	1.163	1.132	1.127	1.085	1.177	1.189	1.148	1.057	1.172	1.296	1.182

Table V. Continued

Run	$\frac{p_{13}}{p_{fp}}$	$\frac{p_{14}}{p_{fp}}$	$\frac{p_{15}}{p_{fp}}$	$\frac{p_{16}}{p_{fp}}$	$\frac{p_{17}}{p_{fp}}$	$\frac{p_{18}}{p_{fp}}$	$\frac{p_{19}}{p_{fp}}$	$\frac{p_{20}}{p_{fp}}$	$\frac{p_{21}}{p_{fp}}$	$\frac{p_{22}}{p_{fp}}$	$\frac{p_{23}}{p_{fp}}$	$\frac{p_{24}}{p_{fp}}$
Laminar boundary layer, blunt leading edge												
Aligned array												
2	1.113	1.081	1.121	1.117	1.051	1.043	1.037	1.045	1.055	1.052	0.933	0.961
3	1.082	1.024	1.051	1.080	1.037	.966	.974	.993	.989	.988	.889	.907
4	1.112	1.093	1.067	1.113	1.076	1.029	1.039	1.042	1.086	1.036	.999	1.021
5	1.089	1.084	1.067	1.087	1.095	1.044	1.067	1.054	1.097	1.077	1.053	1.074
9	1.160	1.131	1.160	1.140	1.114	1.067	1.074	1.087	1.103	1.089	.982	.992
10	1.063	1.085	1.079	1.092	1.078	1.005	.996	1.035	1.002	1.008	.955	.915
11	1.093	1.075	1.064	1.079	1.098	1.007	1.049	1.014	1.031	1.056	.968	1.010
Skewed array												
14	1.178	1.118	1.222	1.203	1.167	1.109	1.224	1.169	1.183	1.087	1.105	1.124
15	1.169	1.120	1.260	1.222	1.149	1.078	1.203	1.212	1.162	1.105	1.122	1.120
16	1.213	1.173	1.272	1.315	1.196	1.160	1.274	1.183	1.179	1.137	1.158	1.140
17	1.088	1.054	1.112	1.142	1.069	1.047	1.088	1.130	1.100	1.068	1.051	1.054
18	1.043	.993	1.021	1.023	.971	.926	1.004	1.016	1.001	1.015	.983	.984
Turbulent boundary layer, sharp leading edge												
Aligned array												
23	1.230	1.170	1.212	1.193	1.164	1.099	1.099	1.114	1.110	1.117	0.979	1.009
24	1.131	1.132	1.124	1.155	1.101	1.063	1.086	1.094	1.142	1.079	.996	1.034
25	1.098	1.078	1.105	1.072	1.087	1.034	1.061	1.082	1.030	1.055	1.032	1.030
Skewed array												
29	1.357	1.296	1.468	1.410	1.401	1.265	1.353	1.387	1.331	1.282	1.228	1.249
30	1.397	1.251	1.489	1.502	1.328	1.233	1.275	1.360	1.314	1.213	1.162	1.185
31	1.265	1.169	1.320	1.274	1.220	1.130	1.220	1.233	1.171	1.127	1.113	1.135
32	1.282	1.223	1.297	1.323	1.271	1.144	1.194	1.258	1.254	1.220	1.147	1.185
33	1.167	1.125	1.171	1.164	1.157	1.091	1.131	1.188	1.140	1.118	1.135	1.093

Table V. Continued

Run	$\frac{p_{25}}{p_{fp}}$	$\frac{p_{26}}{p_{fp}}$	$\frac{p_{27}}{p_{fp}}$	$\frac{p_{28}}{p_{fp}}$	$\frac{p_{29}}{p_{fp}}$	$\frac{p_{30}}{p_{fp}}$	$\frac{p_{31}}{p_{fp}}$	$\frac{p_{32}}{p_{fp}}$	$\frac{p_{33}}{p_{fp}}$	$\frac{p_{34}}{p_{fp}}$	$\frac{p_{35}}{p_{fp}}$	$\frac{p_{36}}{p_{fp}}$
Laminar boundary layer, blunt leading edge												
Aligned array												
2	1.000	1.017	0.821	0.864	0.913	0.952	0.992	0.888	0.874	0.932	0.987	0.915
3	.937	.972	.764	.814	.874	.907	.957	.804	.829	.893	.935	.858
4	.999	1.044	.959	.975	.999	.999	1.039	.962	.978	1.016	1.029	1.012
5	1.062	1.072	1.032	1.030	1.042	1.046	1.079	1.040	1.035	1.063	1.067	1.039
9	1.035	1.060	.859	.942	.963	.985	1.026	.884	.917	.978	1.038	.935
10	.969	.984	.874	.838	.890	.920	.986	.933	.836	.919	.954	.978
11	1.012	1.021	.941	.988	.993	1.049	1.027	.960	1.004	1.000	1.061	.991
Skewed array												
14	1.090	1.091	1.012	1.022	1.074	1.040	1.068	0.964	0.976	1.033	1.047	0.876
15	1.117	1.071	1.011	1.034	1.041	1.030	1.037	.939	.957	1.000	1.018	.878
16	1.139	1.109	1.054	1.073	1.066	1.075	1.084	.979	.999	1.015	1.061	.894
17	1.065	1.036	.998	1.027	1.036	1.038	1.018	.986	1.001	1.012	1.036	.930
18	.984	.977	.959	.989	.991	.965	.971	.965	.961	.967	.972	.970
Turbulent boundary layer, sharp leading edge												
Aligned array												
23	1.047	1.081	0.818	0.877	0.925	0.997	1.059	0.820	0.884	0.969	1.046	0.793
24	1.047	1.072	.952	.961	1.021	1.031	1.061	.955	.970	1.034	1.059	.928
25	1.063	1.066	.985	1.018	1.019	1.042	1.061	1.017	1.013	1.030	1.070	1.010
Skewed array												
29	1.248	1.232	1.025	1.076	1.159	1.180	1.212	0.976	1.023	1.119	1.178	0.900
30	1.209	1.197	.975	1.044	1.092	1.122	1.151	.926	1.006	1.078	1.114	.839
31	1.131	1.112	.960	1.006	1.050	1.066	1.090	.886	.951	.998	1.054	.801
32	1.192	1.193	1.066	1.115	1.177	1.146	1.182	1.053	1.084	1.122	1.127	1.001
33	1.133	1.113	1.062	1.076	1.087	1.113	1.102	1.064	1.080	1.075	1.108	1.035

Table V. Continued

Run	$\frac{p_{37}}{p_{fp}}$	$\frac{p_{38}}{p_{fp}}$	$\frac{p_{39}}{p_{fp}}$	$\frac{p_{40}}{p_{fp}}$	$\frac{p_{41}}{p_{fp}}$	$\frac{p_{42}}{p_{fp}}$	$\frac{p_{43}}{p_{fp}}$	$\frac{p_{44}}{p_{fp}}$	$\frac{p_{45}}{p_{fp}}$	$\frac{p_{46}}{p_{fp}}$	$\frac{p_{47}}{p_{fp}}$	$\frac{p_{48}}{p_{fp}}$
Laminar boundary layer, blunt leading edge												
Aligned array												
2	0.862	0.0904	0.986	0.866	0.868	0.922	0.975	0.800	0.839	0.888	0.940	0.975
3	.815	.861	.950	.808	.822	.870	.921	.765	.819	.858	.905	.926
4	.974	.992	1.041	.959	.967	1.008	1.025	.953	.963	.983	.989	1.018
5	1.026	1.033	1.076	1.024	1.029	1.052	1.054	1.017	1.029	1.045	1.054	1.026
9	.871	.960	.994	.946	.909	.963	1.044	.904	.897	.947	1.008	1.044
10	.869	.900	.964	.937	.859	.897	1.001	.889	.849	.880	.913	.959
11	.963	.987	1.034	.959	.989	.996	.998	.945	.954	.960	1.013	1.010
Skewed array												
14	0.918	0.965	1.017	0.868	0.884	0.950	1.002	0.929	0.897	0.876	0.929	0.979
15	.895	.930	1.017	.872	.865	.942	.971	.956	.908	.875	.928	.967
16	.930	.972	1.051	.909	.893	.956	1.012	.956	.893	.916	.966	1.007
17	.951	.971	1.010	.900	.937	.968	1.004	.898	.914	.916	.977	.981
18	.972	.948	.977	.952	.935	.933	1.007	.922	.923	.933	.948	.945
Turbulent boundary layer, sharp leading edge												
Aligned array												
23	0.876	0.944	1.043	0.803	0.879	0.966	1.042	0.802	0.856	0.923	0.995	1.051
24	.973	.983	1.070	.924	.982	1.021	1.039	.932	.966	.992	1.036	1.008
25	.990	1.022	1.067	.987	1.010	1.032	1.029	.983	1.009	1.035	1.050	1.056
Skewed array												
29	0.988	1.050	1.141	0.854	0.930	1.017	1.056	0.727	0.831	0.909	1.025	1.100
30	.922	.987	.986	.761	.852	.926	1.048	.645	.738	.828	.934	1.035
31	.880	.936	1.033	.747	.819	.923	.997	.677	.734	.842	.931	1.000
32	1.057	1.083	1.161	.960	1.015	1.082	1.110	.895	1.007	.985	1.053	1.091
33	1.054	1.070	1.055	1.026	1.039	1.072	1.108	.977	1.008	1.036	1.074	1.086

Table V. Concluded

Run	$\frac{p_{49}}{p_{fp}}$	$\frac{p_{50}}{p_{fp}}$	$\frac{p_{51}}{p_{fp}}$	$\frac{p_{52}}{p_{fp}}$	$\frac{p_{53}}{p_{fp}}$	$\frac{p_{54}}{p_{fp}}$	$\frac{p_{55}}{p_{fp}}$	$\frac{p_{56}}{p_{fp}}$	$\frac{p_{57}}{p_{fp}}$	$\frac{p_{58}}{p_{fp}}$	$\frac{p_{59}}{p_{fp}}$
Laminar boundary layer, blunt leading edge											
Aligned array											
2	1.013	1.020	1.126	1.071	1.185	1.175	1.202	1.158	1.098	1.176	1.156
3	.980	.945	1.039	1.048	1.139	1.145	1.097	1.075	1.054	1.143	1.098
4	1.043	1.005	1.070	1.061	1.141	1.101	1.120	1.122	1.076	1.156	1.099
5	1.056	1.046	1.057	1.099	1.106	1.110	1.121	1.071	1.068	1.085	1.112
9	1.045	1.063	1.128	1.108	1.176	1.212	1.166	1.127	1.113	1.174	1.157
10	.999	.991	1.075	1.070	1.128	1.166	1.150	1.097	1.078	1.125	1.108
11	1.055	1.049	1.042	1.084	1.077	1.077	1.097	1.086	1.047	1.120	1.078
Skewed array											
14	0.896	0.970	0.935	1.011	1.052	1.080	1.031	1.068	1.052	1.123	1.117
15	.879	.892	.939	.965	.980	1.018	1.016	.981	1.023	1.078	1.126
16	.967	.986	.970	1.045	1.039	1.055	1.116	1.039	1.084	1.146	1.131
17	.989	.939	.981	.980	1.040	1.053	1.058	1.047	1.062	1.087	1.069
18	.946	.953	.939	.981	.953	.963	1.006	.990	.947	1.021	1.027
Turbulent boundary layer, sharp leading edge											
Aligned array											
23	1.105	1.104	1.184	1.152	1.311	1.293	1.258	1.217	1.176	1.295	1.267
24	1.078	1.068	1.108	1.097	1.177	1.194	1.156	1.120	1.117	1.159	1.149
25	1.047	1.006	1.050	1.089	1.146	1.128	1.116	1.111	1.070	1.139	1.106
Skewed array											
29	0.888	1.099	0.983	1.132	1.051	1.125	1.129	1.251	1.199	1.232	1.292
30	.818	.960	.907	1.059	.985	1.051	1.092	1.189	1.173	1.172	1.266
31	.811	.986	.894	1.005	.972	.977	1.063	1.082	1.073	1.114	1.119
32	.994	1.091	.990	1.102	1.038	1.072	1.122	1.171	1.151	1.147	1.206
33	1.065	1.089	1.052	1.137	1.008	1.096	1.109	1.098	1.137	1.056	1.131

Table VI. Heating-Rate Values From the Thermocouple-Instrumented Dome

Run	$\frac{\dot{q}_1}{q_{fp}}$	$\frac{\dot{q}_2}{q_{fp}}$	$\frac{\dot{q}_3}{q_{fp}}$	$\frac{\dot{q}_4}{q_{fp}}$	$\frac{\dot{q}_5}{q_{fp}}$	$\frac{\dot{q}_6}{q_{fp}}$	$\frac{\dot{q}_7}{q_{fp}}$	$\frac{\dot{q}_8}{q_{fp}}$	$\frac{\dot{q}_9}{q_{fp}}$	$\frac{\dot{q}_{10}}{q_{fp}}$	$\frac{\dot{q}_{11}}{q_{fp}}$	$\frac{\dot{q}_{12}}{q_{fp}}$
Laminar boundary layer, blunt leading edge												
Aligned array												
2	1.207	1.734	1.816	1.685	1.480	1.269	1.686	1.844	1.727	4.407	2.723	2.213
3	.812	1.461	1.687	1.522	1.393	.978	1.439	1.700	1.608	2.476	1.395	1.554
4	1.115	1.285	1.351	1.135	1.342	1.234	1.249	1.402	1.338	2.399	1.850	1.449
5	1.304	1.324	1.280	1.434	1.430	1.323	1.316	1.396	1.461	1.475	1.440	1.364
9	1.270	1.719	1.844	1.648	1.462	1.431	1.834	2.025	1.817	5.436	3.871	2.664
10	.738	1.421	1.520	1.565	1.274	.916	1.341	1.678	1.522	1.144	1.284	1.552
11	1.007	1.270	1.147	1.176	1.217	1.066	1.161	1.229	1.288	1.294	1.382	1.251
Skewed array												
14	2.170	2.824	2.348	2.317	2.665	2.099	1.974	2.405	2.711	1.982	2.225	2.846
15	2.322	2.568	1.953	1.683	1.812	1.965	1.547	1.689	1.764	.891	.996	1.434
16	1.676	2.316	2.170	1.806	1.366	1.815	1.928	1.899	1.612	1.282	1.127	1.485
17	1.365	1.623	1.509	1.331	1.301	1.511	1.580	1.279	1.278	1.129	1.244	1.086
18	1.255	1.265	1.011	.986	1.023	1.333	1.326	1.099	1.120	1.265	1.299	1.189
Turbulent boundary layer, blunt leading edge												
Aligned array												
23	1.359	1.518	1.328	1.093	0.984	1.394	1.519	1.358	1.091	1.430	1.355	1.424
24	1.298	1.358	1.259	1.189	1.088	1.357	1.352	1.255	1.180	1.293	1.275	1.216
25	1.126	1.251	1.164	1.125	1.051	1.182	1.196	1.190	1.148	1.110	1.177	1.132
Skewed array												
29	1.433	1.517	1.325	1.131	1.016	1.493	1.584	0.808	1.151	1.737	1.474	1.503
30	1.449	1.573	1.379	1.150	1.104	1.549	1.656	1.488	1.222	1.792	1.567	1.626
31	1.571	1.762	1.550	1.263	1.170	1.715	1.857	1.671	1.316	2.025	1.685	1.725
32	1.239	1.274	1.193	1.161	1.127	1.385	1.310	1.227	1.220	1.500	1.419	1.303
33	1.223	1.213	1.090	1.133	1.085	1.260	1.177	1.185	1.167	1.294	1.278	1.086

Table VI. Continued

Run	\dot{q}_{13} \dot{q}_{fp}	\dot{q}_{14} \dot{q}_{fp}	\dot{q}_{15} \dot{q}_{fp}	\dot{q}_{16} \dot{q}_{fp}	\dot{q}_{17} \dot{q}_{fp}	\dot{q}_{18} \dot{q}_{fp}	\dot{q}_{19} \dot{q}_{fp}	\dot{q}_{20} \dot{q}_{fp}	\dot{q}_{21} \dot{q}_{fp}	\dot{q}_{22} \dot{q}_{fp}	\dot{q}_{23} \dot{q}_{fp}	\dot{q}_{24} \dot{q}_{fp}
Laminar boundary layer, blunt leading edge												
Aligned array												
2	1.892	1.637	4.436	2.868	2.003	1.644	4.406	3.096	2.005	1.595	3.552	2.696
3	1.665	1.540	3.241	1.713	1.556	1.500	4.259	2.050	1.509	1.503	2.979	1.740
4	1.367	1.252	2.478	1.910	1.405	1.384	2.587	2.056	1.536	1.344	2.448	1.887
5	1.313	1.419	1.537	1.456	1.447	1.399	1.507	1.482	1.299	1.421	1.562	1.409
9	2.052	1.828	5.072	3.497	2.368	1.673	4.987	3.778	2.290	1.704	3.685	3.011
10	1.653	1.515	1.459	1.420	1.699	1.545	1.494	1.444	1.466	1.410	1.211	1.382
11	1.323	1.238	1.314	1.395	1.186	1.287	1.227	1.181	1.279	1.262	1.160	1.315
Skewed array												
14	2.942	2.877	2.262	2.260	2.638	2.771	2.647	2.928	2.338	2.513	2.629	2.765
15	1.881	1.765	2.091	1.501	1.782	1.757	2.682	2.814	2.096	1.689	2.314	2.776
16	1.709	1.533	2.194	1.896	1.556	1.467	2.070	2.437	2.042	1.383	1.889	2.394
17	1.258	1.291	1.483	1.360	1.444	1.158	1.381	1.620	1.532	1.287	1.536	1.565
18	.961	.998	1.169	1.056	.428	.927	1.094	1.225	.851	.970	1.233	1.037
Turbulent boundary layer, sharp leading edge												
Aligned array												
23	1.264	1.052	1.125	1.149	1.156	1.039	1.261	1.072	1.030	0.999	0.755	0.845
24	1.157	1.149	1.131	1.104	1.116	1.128	1.043	1.063	1.037	1.088	.992	1.002
25	1.111	1.119	1.057	1.061	1.077	1.068	1.005	1.025	.936	1.039	1.003	.992
Skewed array												
29	1.409	1.142	1.521	1.363	1.320	1.156	1.458	1.410	1.232	1.093	1.158	1.202
30	1.497	1.244	1.614	1.511	1.413	1.199	1.690	1.480	1.309	1.158	1.266	1.176
31	1.620	1.309	1.780	1.679	1.537	1.278	1.667	1.578	1.453	1.255	1.257	1.368
32	1.225	1.234	1.352	1.333	1.219	1.213	1.249	1.295	1.234	1.195	1.272	1.248
33	1.108	1.210	1.245	1.172		1.186	1.205	1.178		1.121	1.193	1.137

Table VI. Continued

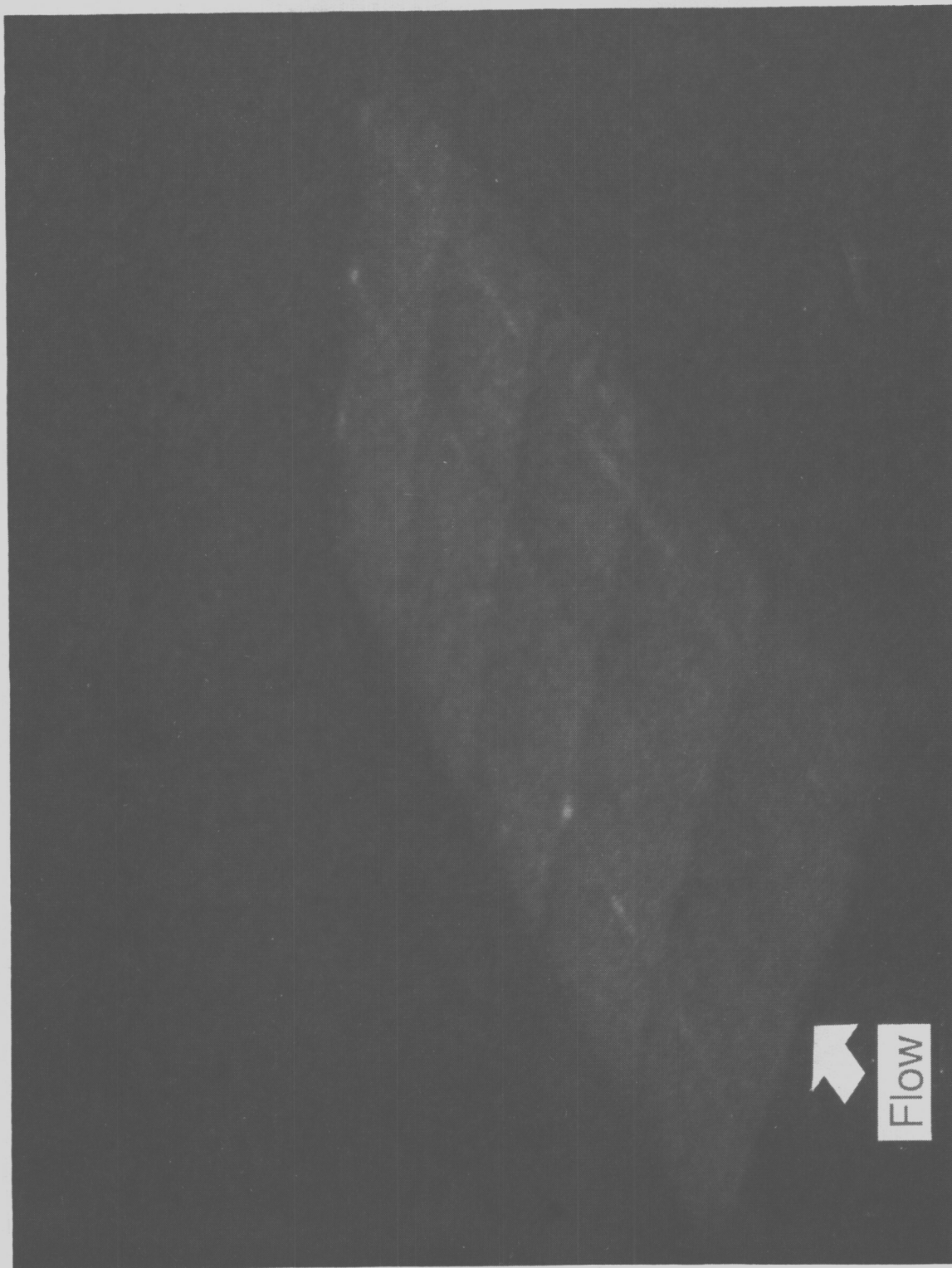
Run	$\frac{q_{25}}{q_F}$	$\frac{q_{26}}{q_F}$	$\frac{q_{27}}{q_F}$	$\frac{q_{28}}{q_F}$	$\frac{q_{29}}{q_F}$	$\frac{q_{30}}{q_F}$	$\frac{q_{31}}{q_F}$	$\frac{q_{32}}{q_F}$	$\frac{q_{33}}{q_F}$	$\frac{q_{34}}{q_F}$	$\frac{q_{35}}{q_F}$	$\frac{q_{36}}{q_F}$
Laminar boundary layer, blunt leading edge												
Aligned array												
2	1.856	1.512	3.094	2.511	1.894	1.643	1.454	1.233	1.371	1.387	1.431	0.656
3	1.387	1.394	2.706	1.663	1.360	1.349	1.392	.998	1.220	1.339	1.374	.819
4	1.463	1.369	2.041	1.833	1.589	1.442	1.416	1.259	1.348	1.262	1.331	1.008
5	1.496	1.425	1.554	1.479	1.419	1.512	1.429	1.331	1.411	1.320	1.386	1.193
9	2.063	1.731	3.447	2.965	2.145	1.834	1.677	1.530	1.507	1.615	1.491	.782
10	1.510	1.444	.905	1.097	1.263	1.339	1.401	.894	1.192	1.313	1.347	.617
11	1.257	1.261	1.276	1.152	1.267	1.282	1.229	1.212	1.282	1.217	1.241	1.104
Skewed array												
14	2.373	2.385	1.399	2.375	2.375	2.335	2.284	1.986	2.128	2.003	2.259	1.581
15	2.195	1.628	1.045	2.173	2.394	2.314	1.444	1.827	2.044	1.745	1.582	1.454
16	2.190	1.538	.872	1.872	2.275	2.125	1.487	1.856	2.052	1.834	1.463	1.477
17	1.529	1.275	1.308	1.386	1.610	1.603	1.452	1.427	1.595	1.502	1.359	1.116
18	1.034	.914	1.241	1.208	1.115	.994	.817	1.127	1.072	.990	.952	1.006
Turbulent boundary layer, sharp leading edge												
Aligned array												
23	0.896	0.980	0.696	0.690	0.719	0.832	0.937	0.645	0.698	0.810	0.921	0.614
24	1.028	1.037	.861	.873	.928	.974	1.013	.789	.891	.949	1.030	.733
25	.981	1.026	.926	.921	.928	.946	.998	.865	.879	.899	.960	.828
Skewed array												
29	1.121	1.082	1.026	1.092	1.081	1.051	1.052	0.942	0.930	0.956	1.009	0.789
30	1.148	1.134	1.053	1.079	1.056	1.074	1.086	.948	.930	.982	1.030	.807
31	1.296	1.216	1.088	1.201	1.175	1.197	1.163	1.014	1.013	1.080	1.132	.849
32	1.200	1.162	1.119	1.082	1.125	1.116	1.125	.951	1.003	1.057	1.106	.841
33	1.119	1.124	1.074	1.084	1.092	1.088	1.102	1.028	1.050	1.038	1.055	.960

Table VI. Continued

Run	\dot{q}_{37} q_{fp}	\dot{q}_{38} q_{fp}	\dot{q}_{39} q_{fp}	\dot{q}_{40} q_{fp}	\dot{q}_{41} q_{fp}	\dot{q}_{42} q_{fp}	\dot{q}_{43} q_{fp}	\dot{q}_{44} q_{fp}	\dot{q}_{45} q_{fp}	\dot{q}_{46} q_{fp}	\dot{q}_{47} q_{fp}	\dot{q}_{48} q_{fp}
Laminar boundary layer, blunt leading edge												
Aligned array												
2	1.303	1.401	1.480	1.281	1.403	1.461	1.483	3.436	2.967	2.056	1.638	1.646
3	1.174	1.321	1.343	1.112	1.208	1.388	1.399	3.427	2.535	1.460	1.436	1.488
4	1.055	1.286	1.348	1.259	1.300	1.114	1.273	1.595	1.443	1.369	1.232	1.318
5	1.305	1.319	1.359	1.230	1.270	1.383	1.427	1.709	1.531	1.413	1.374	1.428
9	1.369	1.515	1.606	1.004	1.190	1.390	1.503	1.477	1.644	1.494	1.473	1.599
10	1.249	1.442	1.383	.879	1.115	1.289	1.330	1.179	1.442	1.194	1.271	1.352
11	1.064	1.179	1.236	1.182	1.402	1.167	1.236	1.374	1.176	1.319	1.239	1.293
Skewed array												
14	1.734	2.069	2.694	1.388	1.826	2.232	2.583	1.955	2.329	2.304	2.529	2.743
15	1.626	1.554	1.644	.972	1.414	1.583	1.869	1.337	1.601	1.598	1.827	1.930
16	1.746	1.681	1.540	.925	1.346	1.466	1.454	.449	.984	1.195	1.351	1.493
17	1.367	1.350	1.404	1.186	1.224	1.324	1.424	.820	1.041	1.228	1.131	1.260
18	1.231	1.097	1.035	1.150	1.196	1.127	1.011	1.215	1.133	1.218	.999	.906
Turbulent boundary layer, sharp leading edge												
Aligned array												
23	0.693	0.786	0.938	0.630	0.686	0.771	0.906	0.720	0.815	0.774	0.806	0.926
24	.833	.961	1.002	.788	.846	.941	.993	.868	.879	.936	.970	1.009
25	.868	.881	.934	.883	.842	.909	.967	.938	.958	.935	.949	.988
Skewed array												
29	0.826	0.901	1.014	0.687	0.733	0.823	0.989	0.626	0.729	0.705	0.784	0.981
30	.826	.912	1.052	.677	.749	.860	1.059	.665	.781	.738	.824	1.036
31	.890	.968	1.128	.719	.767	.893	1.107	.640	.746	.729	.827	1.088
32	.912	1.013	1.080	.855	.891	.973	1.033	.778	.830	.909	.966	1.020
33	1.000	1.015	1.017	.985	1.010	1.023	1.034	.937	.988	.986	1.026	1.030

Table VI. Concluded

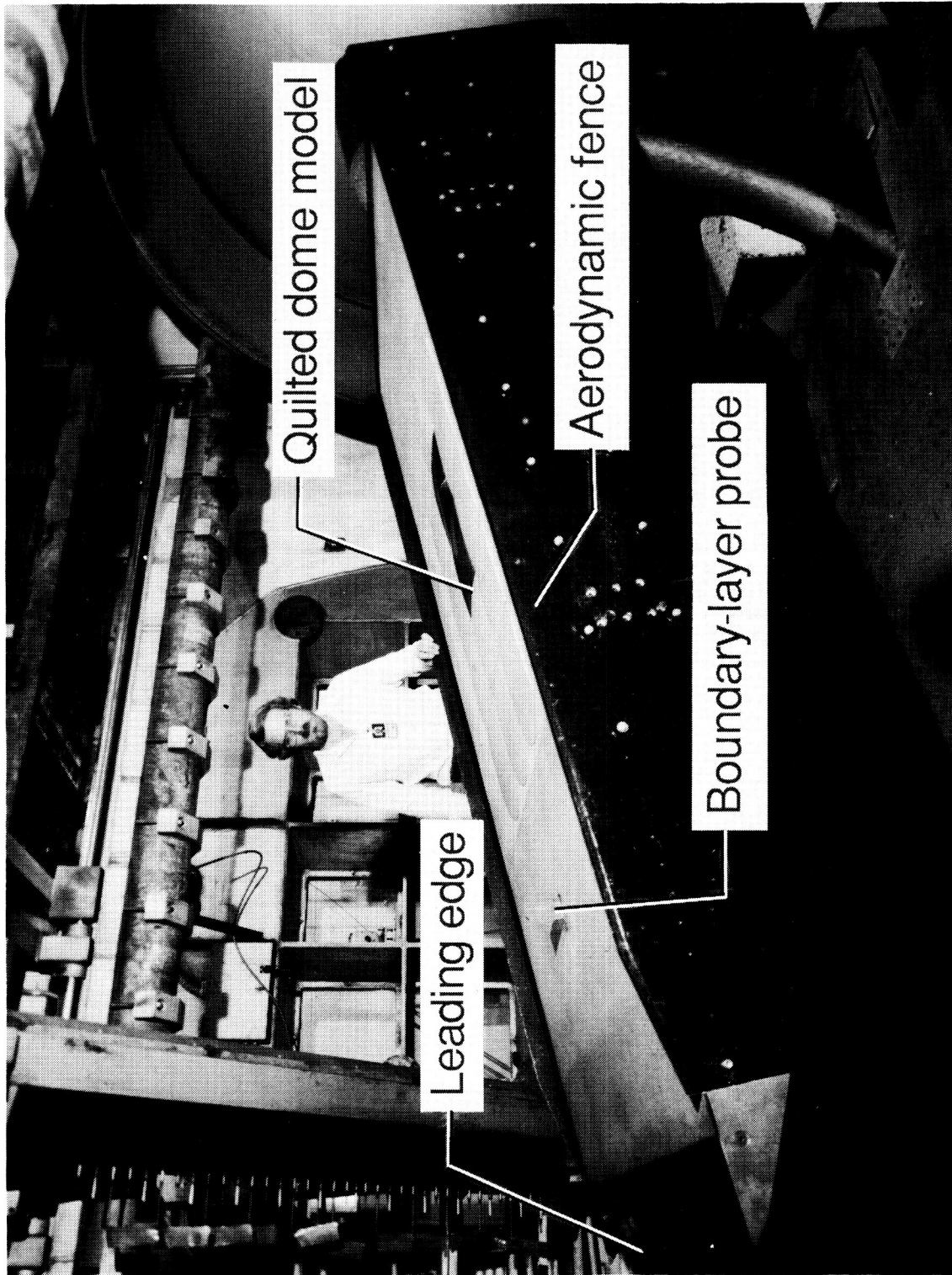
Run	$\frac{q_{49}}{q_{fp}}$	$\frac{q_{50}}{q_{fp}}$	$\frac{q_{51}}{q_{fp}}$	$\frac{q_{52}}{q_{fp}}$	$\frac{q_{53}}{q_{fp}}$	$\frac{q_{54}}{q_{fp}}$	$\frac{q_{55}}{q_{fp}}$	$\frac{q_{56}}{q_{fp}}$	$\frac{q_{57}}{q_{fp}}$	$\frac{q_{58}}{q_{fp}}$	$\frac{q_{59}}{q_{fp}}$
Laminar boundary layer, blunt leading edge											
Aligned array											
2	4.551	2.294	4.754	2.209	5.783	3.764	2.536	1.986	1.823	1.772	1.857
3	4.723	1.625	4.352	1.684	3.914	2.222	1.768	1.663	1.586	1.264	1.642
4	1.912	1.450	1.865	1.304	1.689	1.497	1.376	1.342	1.364	1.232	1.334
5	1.799	1.428	1.684	1.406	1.657	1.477	1.397	1.367	1.416	1.359	1.365
9	1.840	1.712	2.074	1.928	2.004	2.065	1.854	1.950	1.820	1.562	1.859
10	1.485	1.488	1.707	1.541	1.500	1.606	1.532	1.726	1.547	1.207	1.580
11	1.353	1.248	1.258	1.235	1.339	1.299	1.396	1.209	1.396	1.272	1.238
Skewed array											
14	1.379	1.798	2.098	2.012	1.916	2.481	2.537	2.238	2.104	2.454	2.161
15	1.309	1.449	1.974	1.750	1.533	2.178	2.482	1.976	1.517	2.317	1.947
16	1.376	1.697	1.835	1.866	1.660	2.119	2.187	2.307	1.795	2.013	2.185
17	1.152	1.382	1.304	1.586	1.308	1.516	1.539	1.712	1.404	1.554	1.603
18	1.072	1.128	1.219	1.104	1.301	1.282	1.320	1.129	1.030	1.229	1.168
Turbulent boundary layer, sharp leading edge											
Aligned array											
23	0.990	1.002	1.083	1.107	1.479	1.382	1.251	1.214	1.100	1.498	1.275
24	1.104	1.077	1.149	1.146	1.303	1.340	1.244	1.212	1.158	1.385	1.289
25	1.010	1.045	1.052	1.083	1.084	1.139	1.149	1.156	1.108	1.175	1.183
Skewed array											
29	0.815	0.852	0.838	0.959	1.132	1.169	1.114	1.079	1.087	1.444	1.159
30	.817	.869	.841	.961	1.131	1.098	1.126	1.109	1.117	1.455	1.195
31	.874	.925	.915	1.056	1.210	1.218	1.233	1.236	1.222	1.572	1.373
32	.916	.999	.959	1.060	1.146	1.122	1.124	1.129	1.175	1.252	1.223
33	.991	1.030	1.032	1.056	1.104	1.080	1.102	1.077	1.089	1.204	1.046



L-83-10,866

Figure 1. Typical test of super alloy honeycomb TPS 20-tile array in Langley 8-Foot High-Temperature Tunnel.

ORIGINAL PAGE IS
OF POOR QUALITY



L-85-2648

Figure 2. Aligned array quilted dome model installed in panel holder of 8-Foot High-Temperature Tunnel.

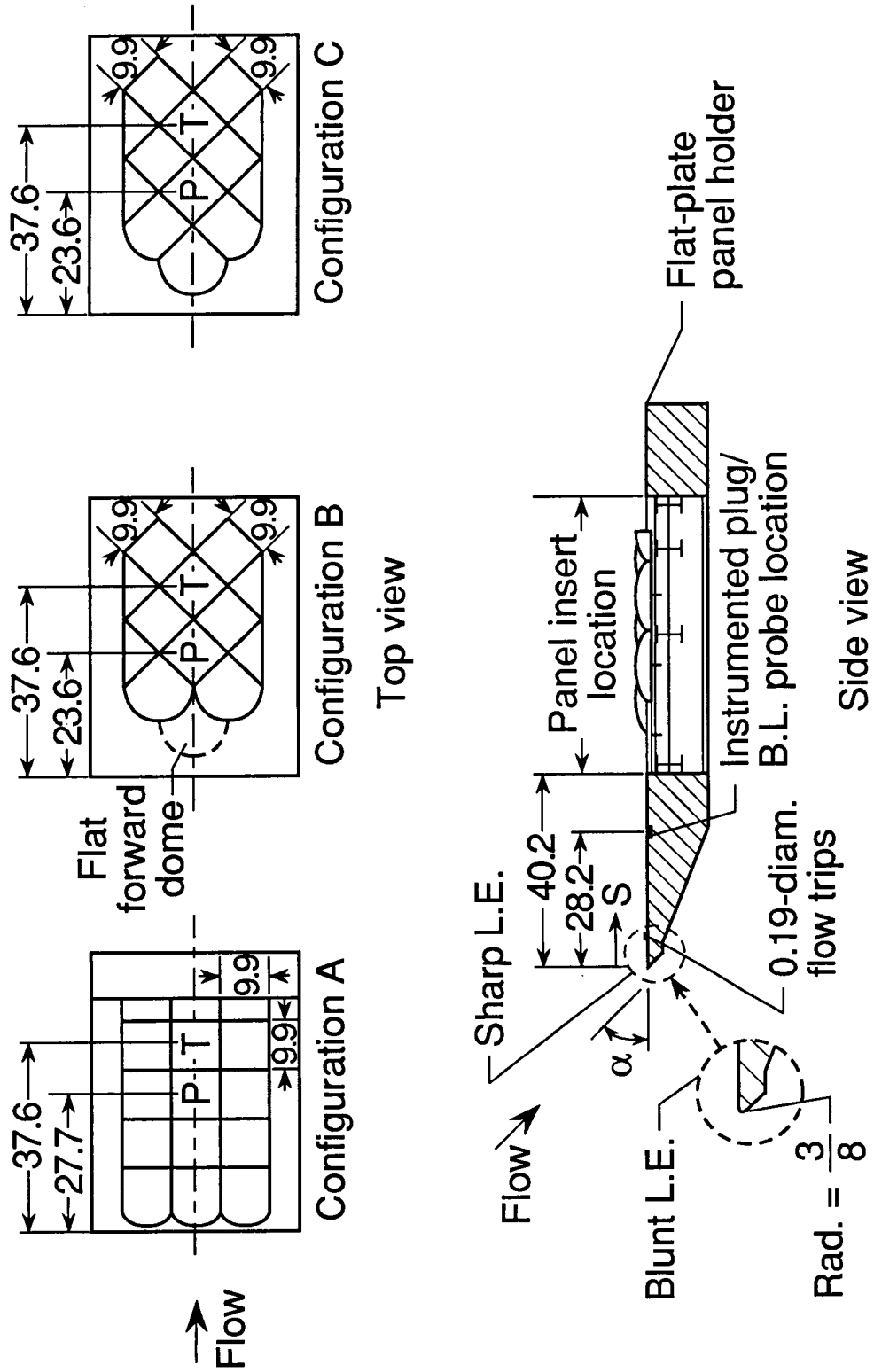
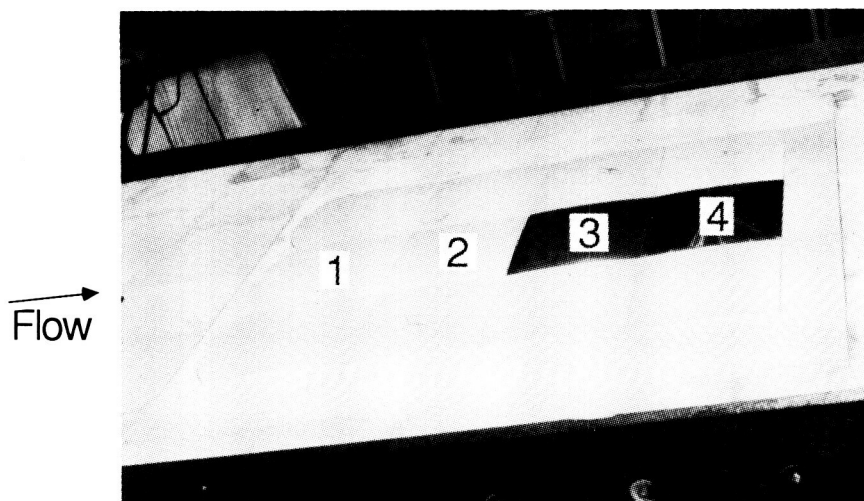
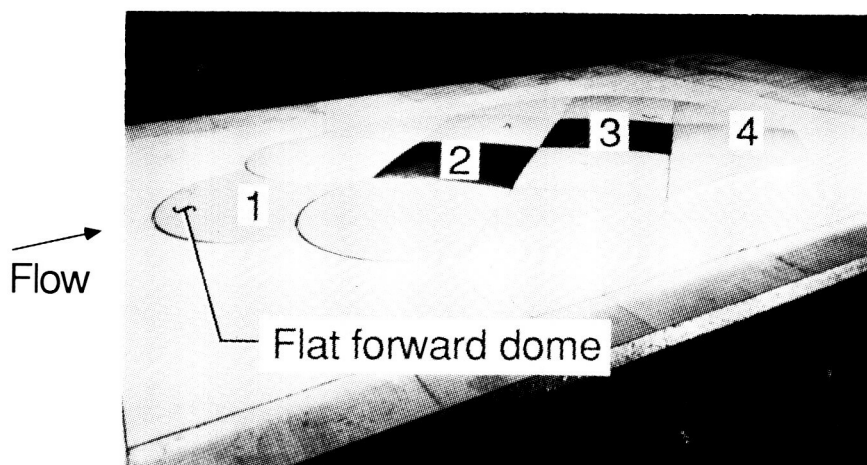


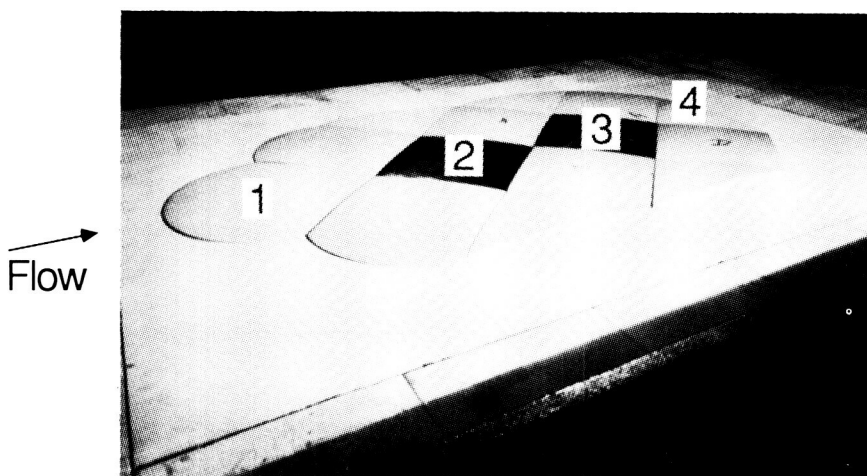
Figure 3. Schematic of the panel holder with quilted dome model inserts. All dimensions in inches.



(a) Configuration A.



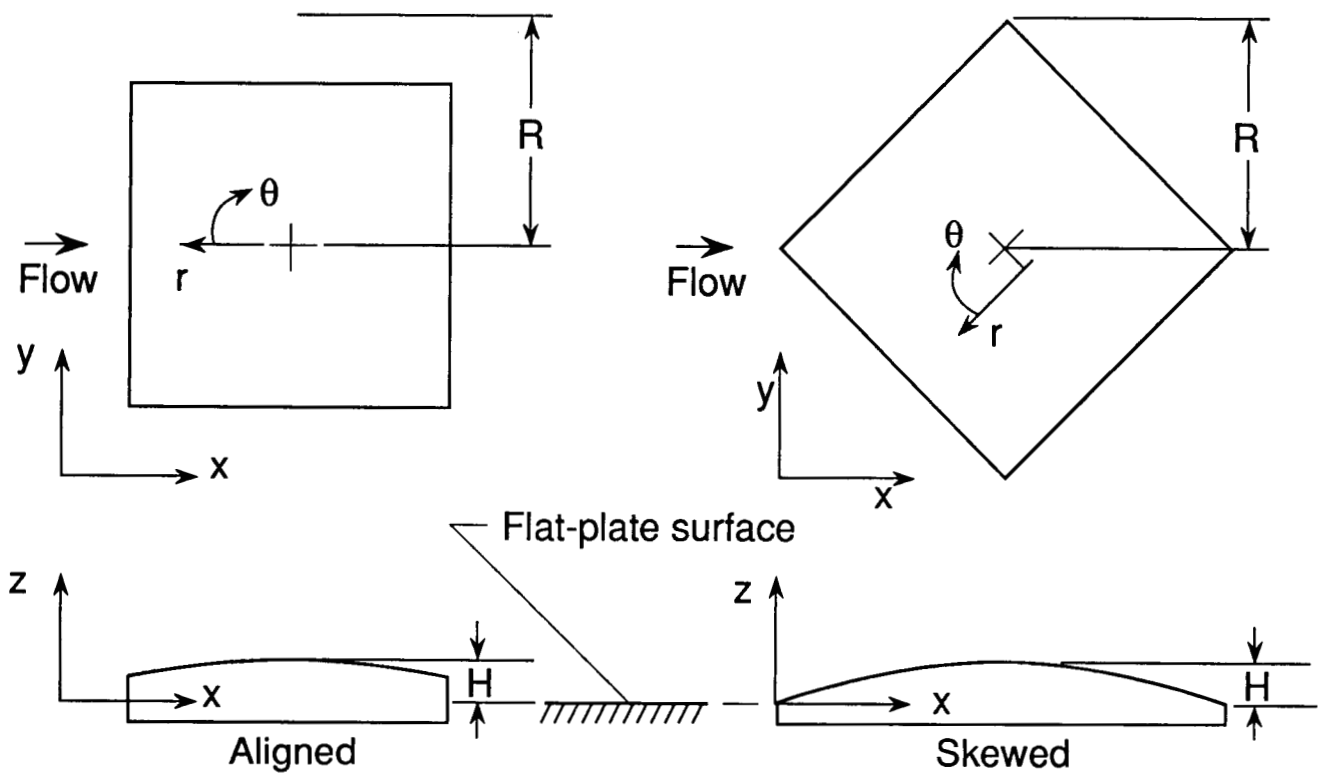
(b) Configuration B.



(c) Configuration C.

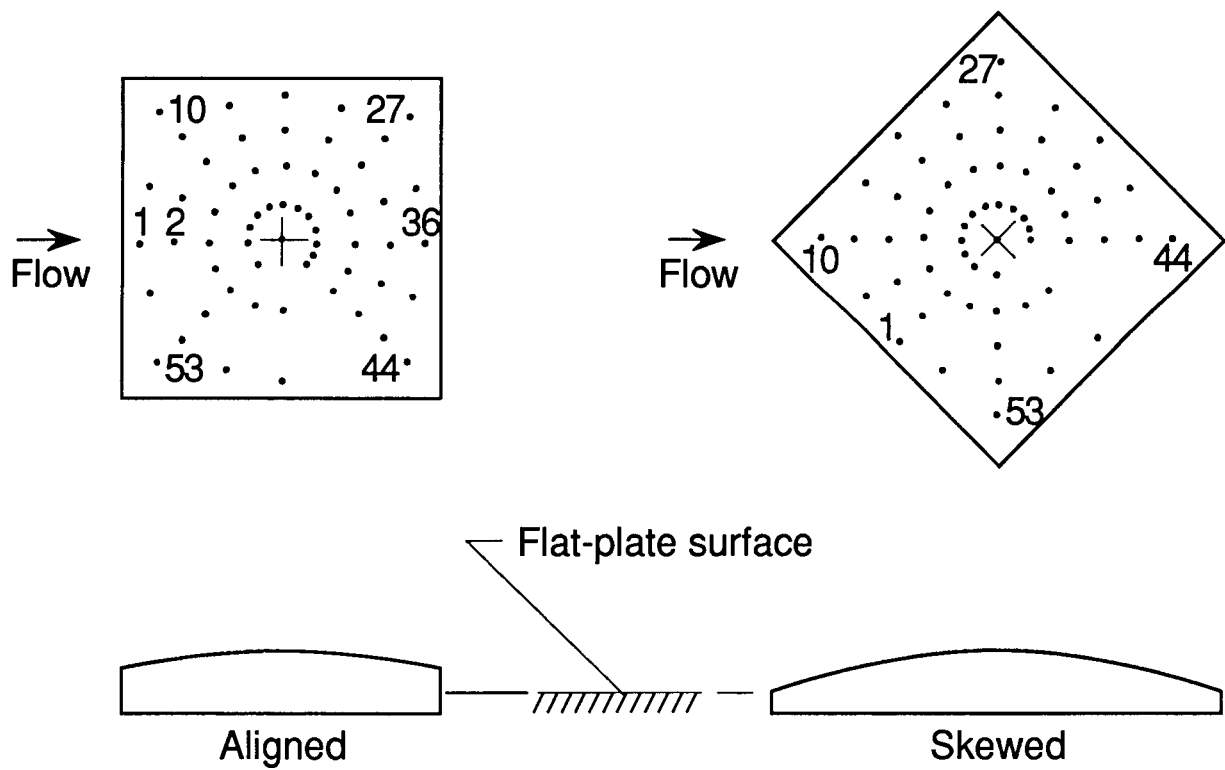
L-88-74

Figure 4. Quilted dome model configuration showing dome location numbers.



(a) Coordinate system for pressure- and thermocouple-instrumented domes. $R = 7$ in.

Figure 5. Coordinate system and instrumentation locations.



(b) Instrumentation locations for pressure- and thermocouple-instrumented domes.

Figure 5. Concluded.

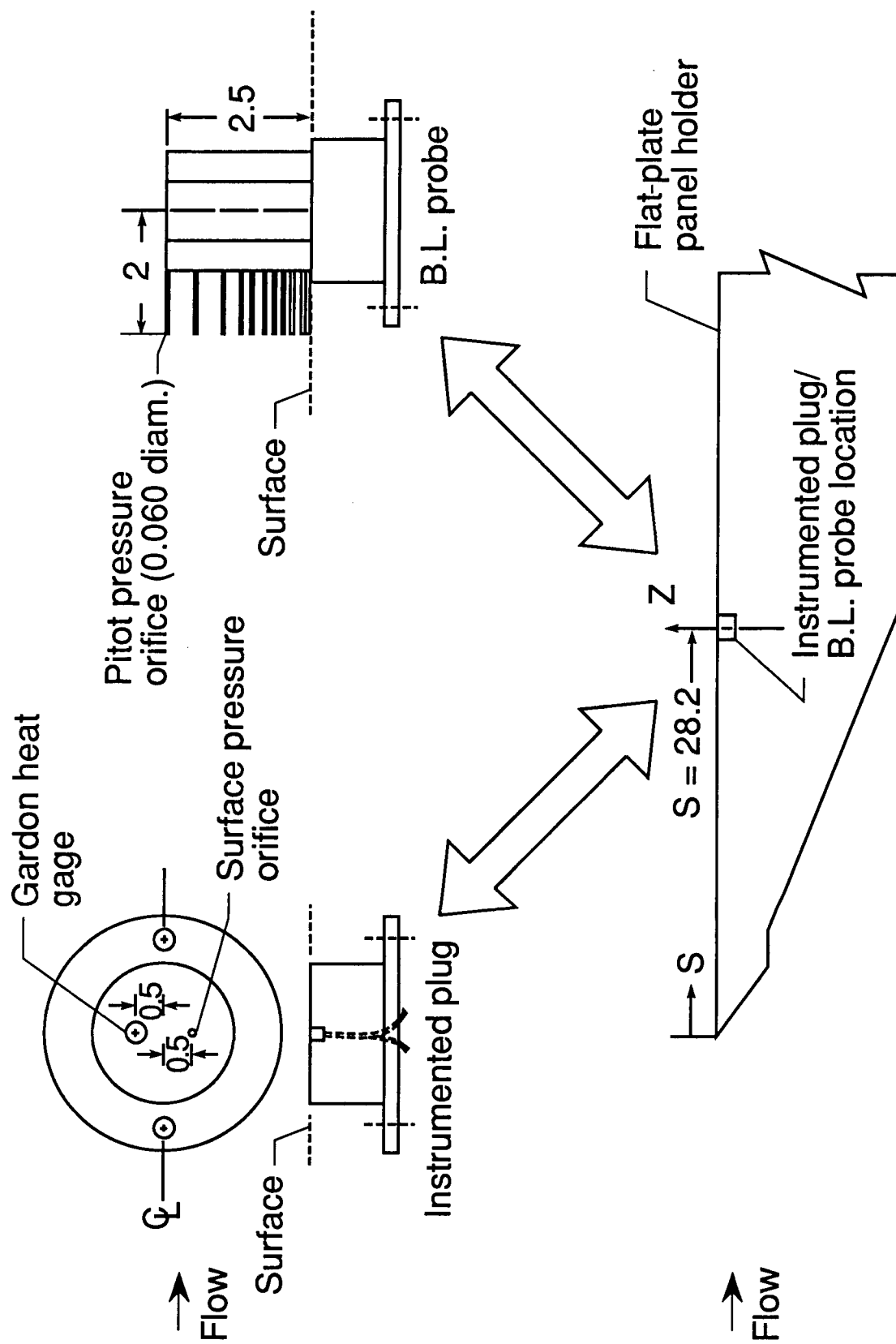


Figure 6. Schematic of the instrumented plug and boundary-layer probe. All dimensions in inches.

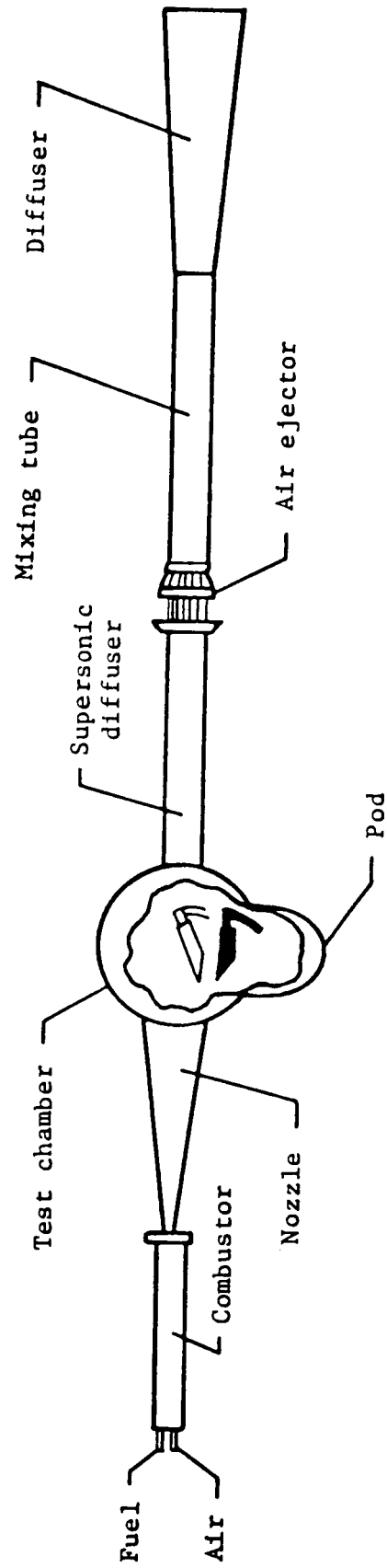


Figure 7. The Langley 8-Foot High-Temperature Tunnel.

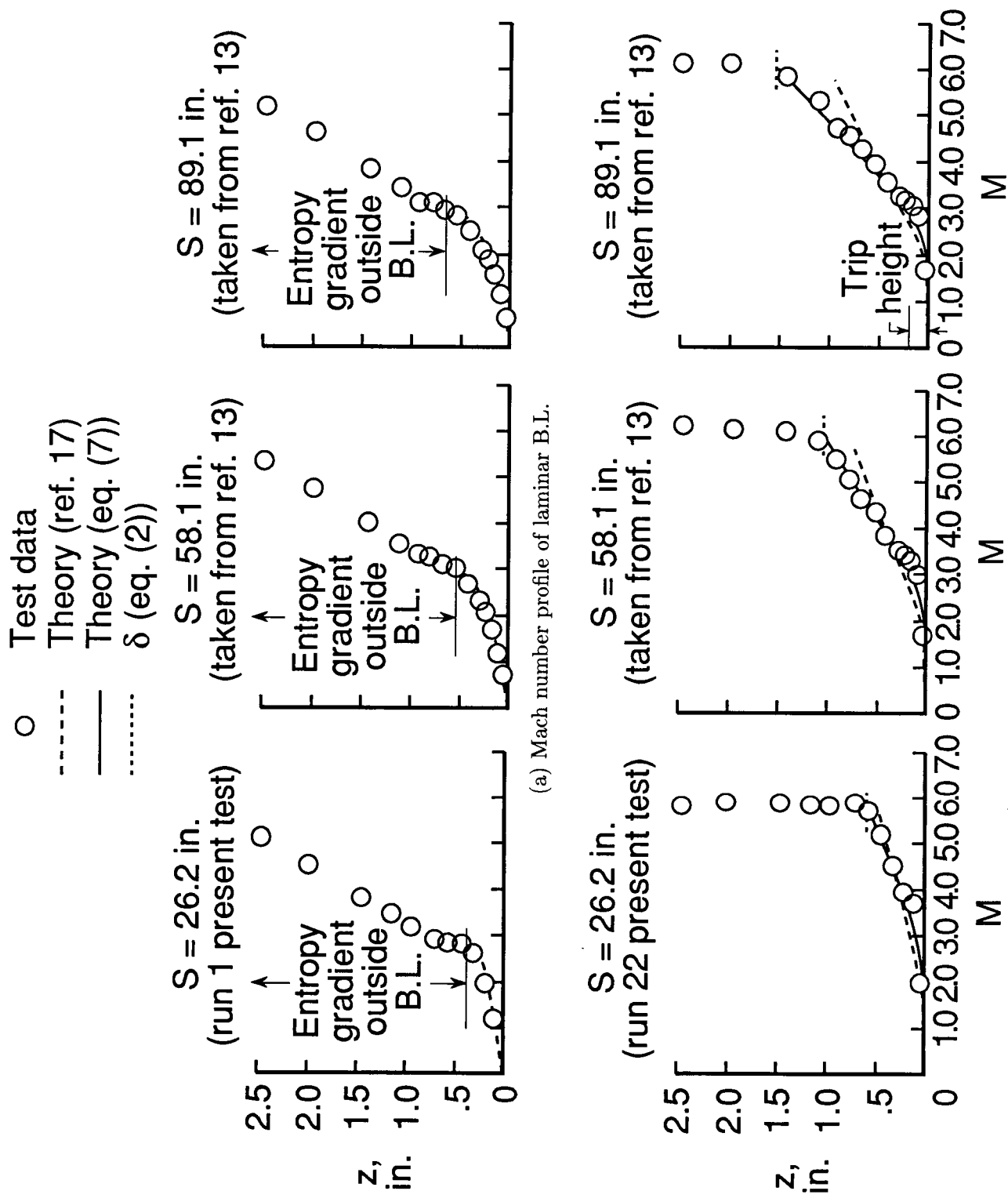
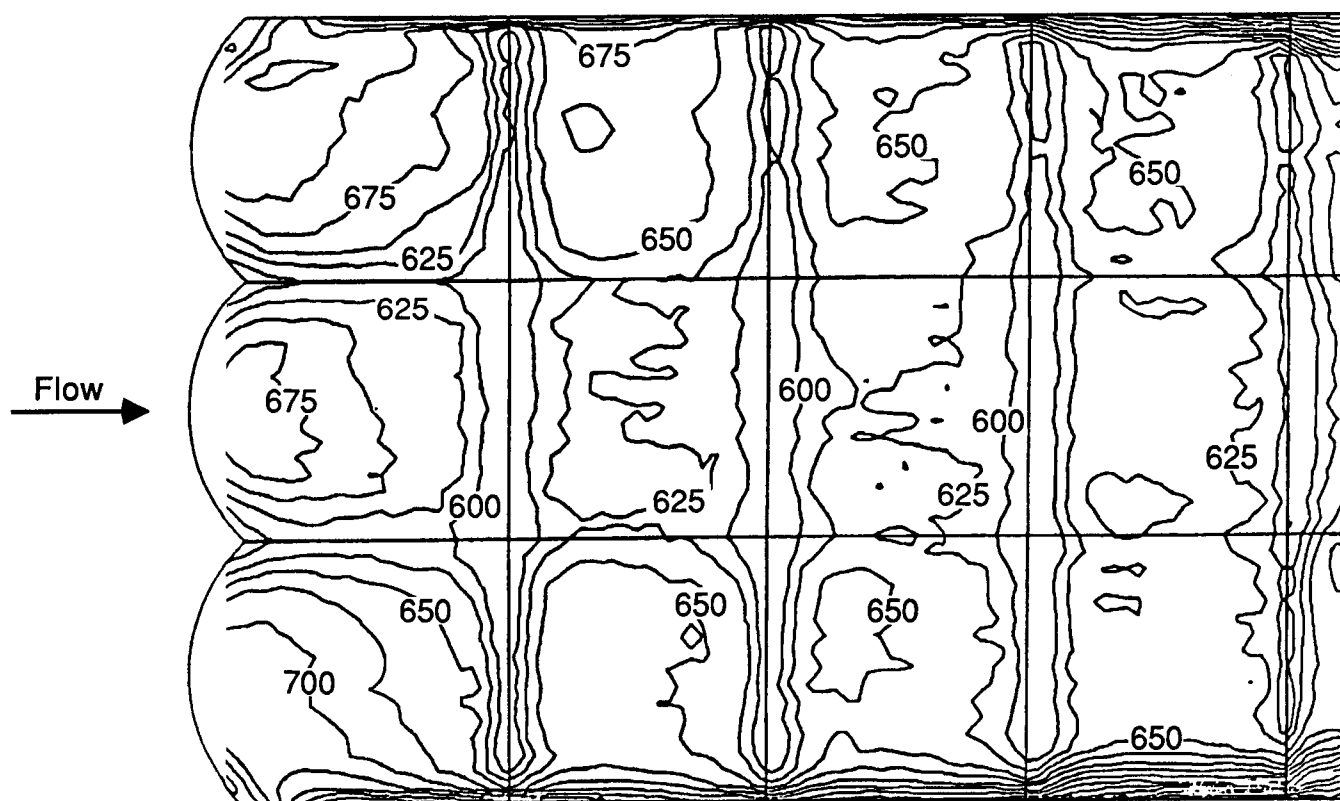
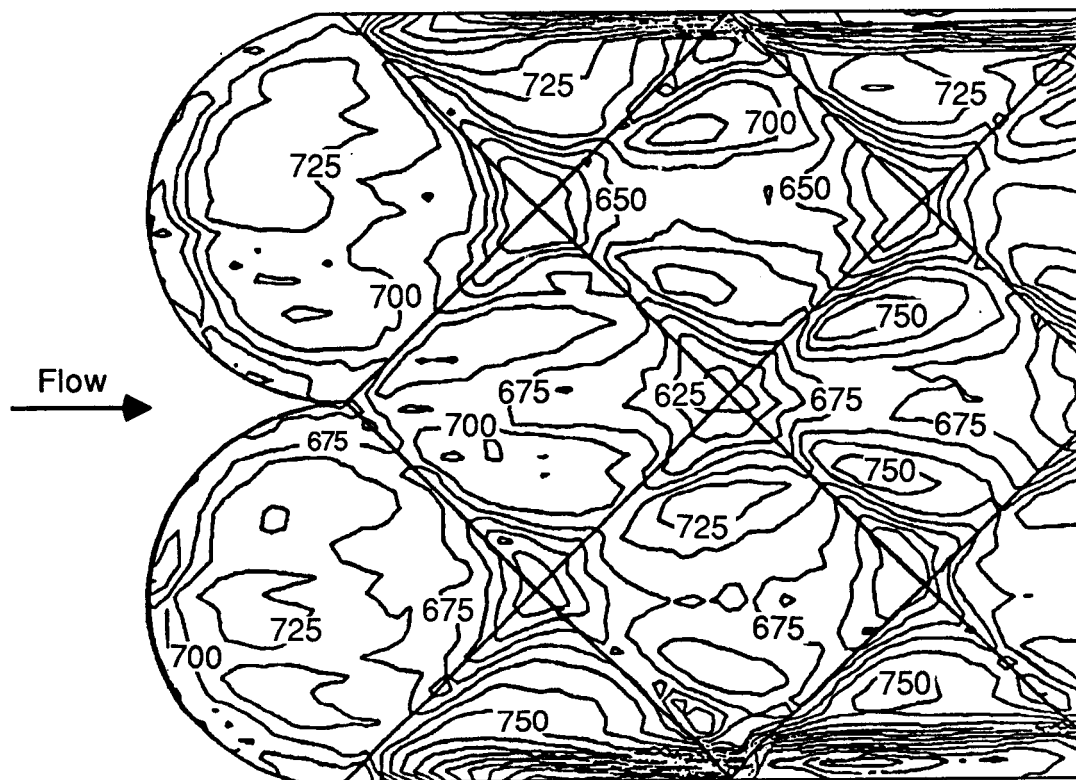


Figure 8. Boundary layer profiles for undisturbed flow. $\alpha = 5^\circ$.



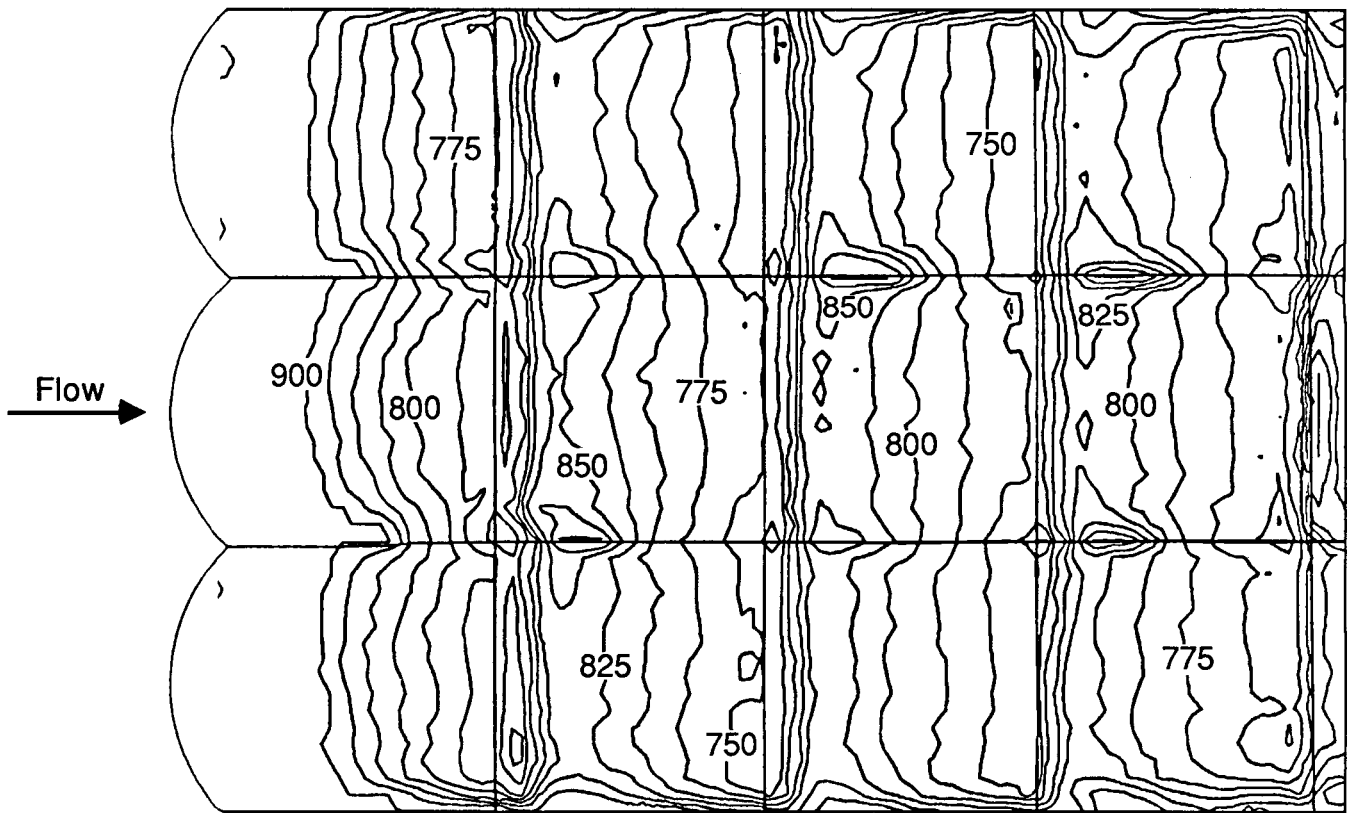
(a) Laminar B. L., aligned array.

Figure 9. Ceramic dome model temperature distributions. All temperatures given in °R; $H = 0.4$ in.



(b) Laminar B.L., skewed array.

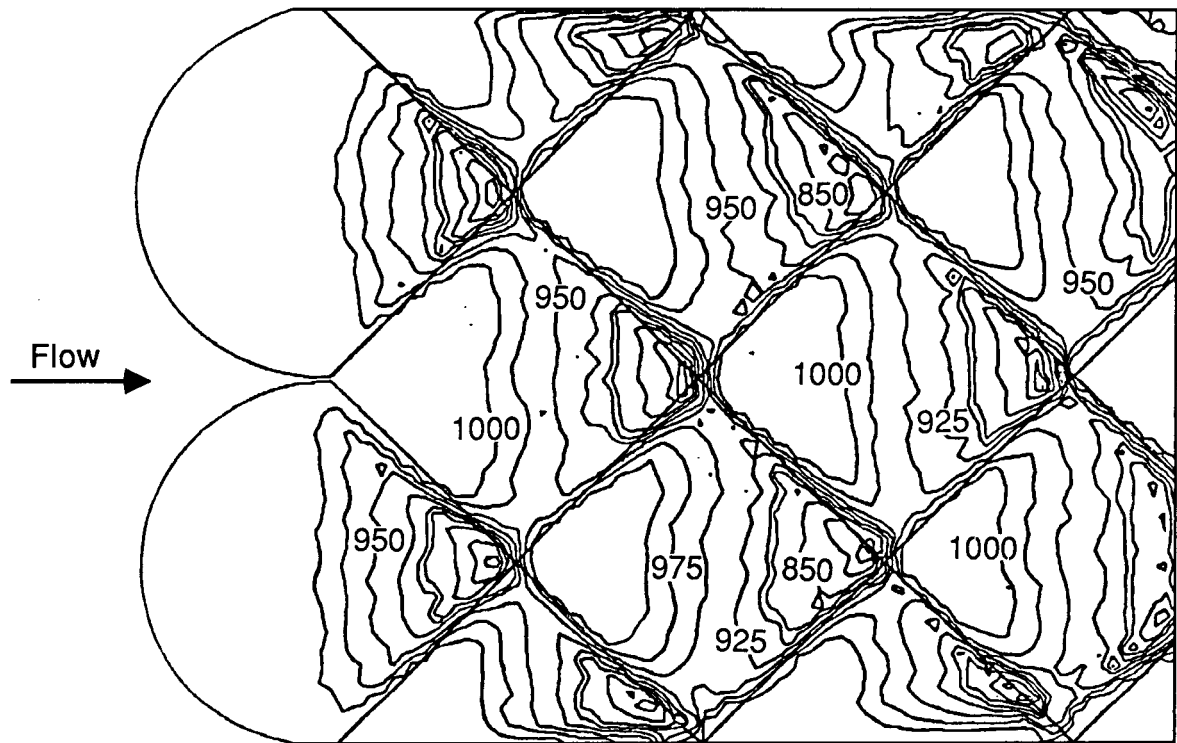
Figure 9. Continued.



(c) Turbulent B.L., aligned array.

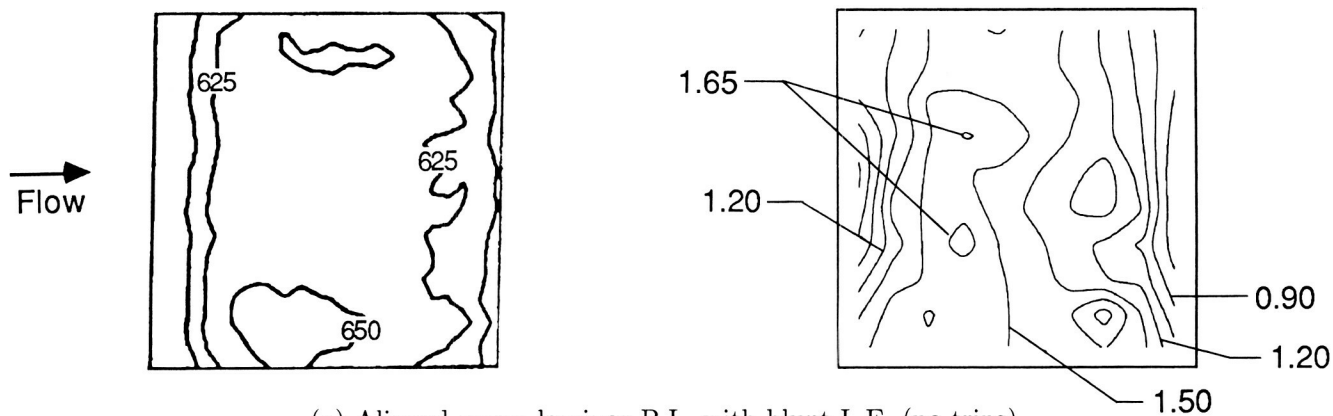
Figure 9. Continued.

ORIGINAL PAGE IS
OF POOR QUALITY.

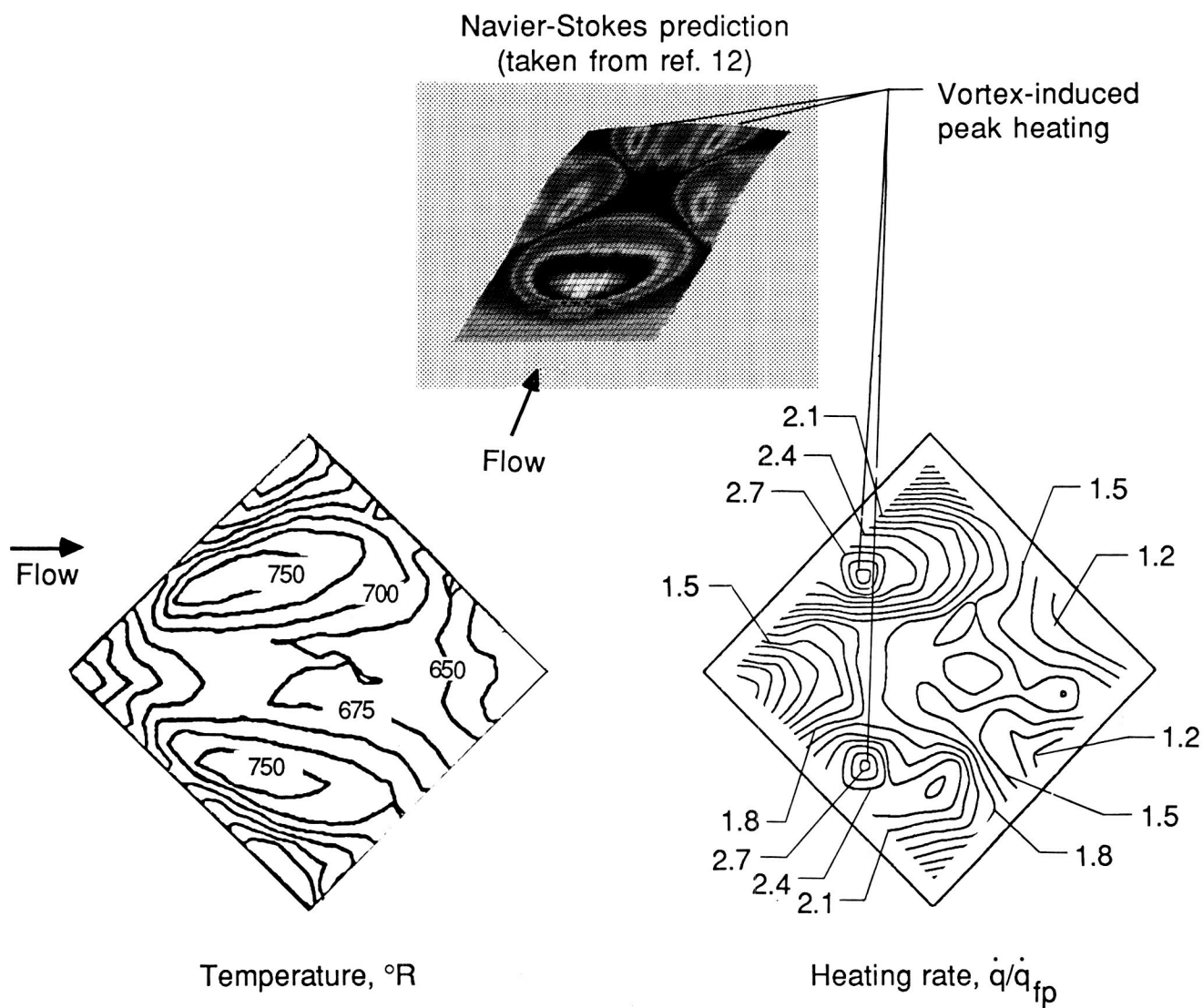


(d) Turbulent B.L., skewed array.

Figure 9. Concluded.

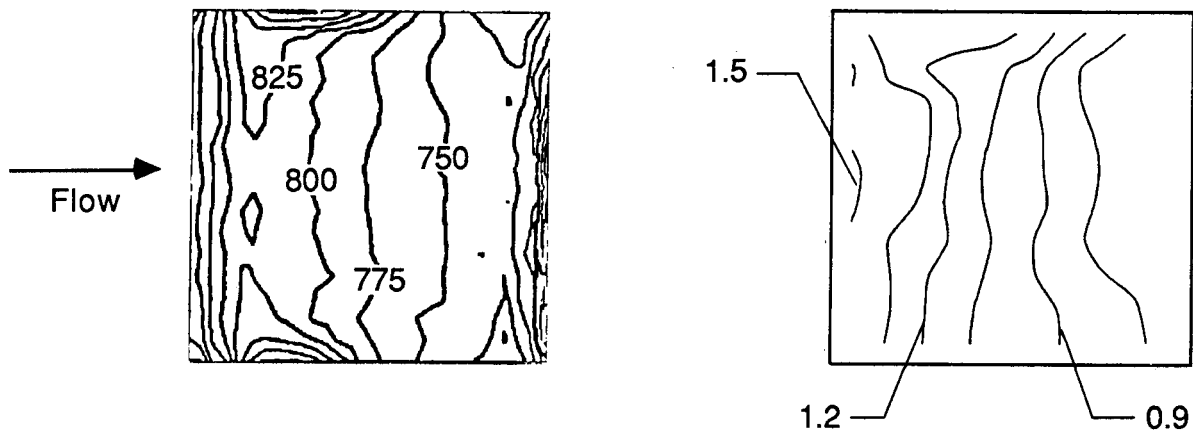


(a) Aligned array, laminar B.L. with blunt L.E. (no trips).

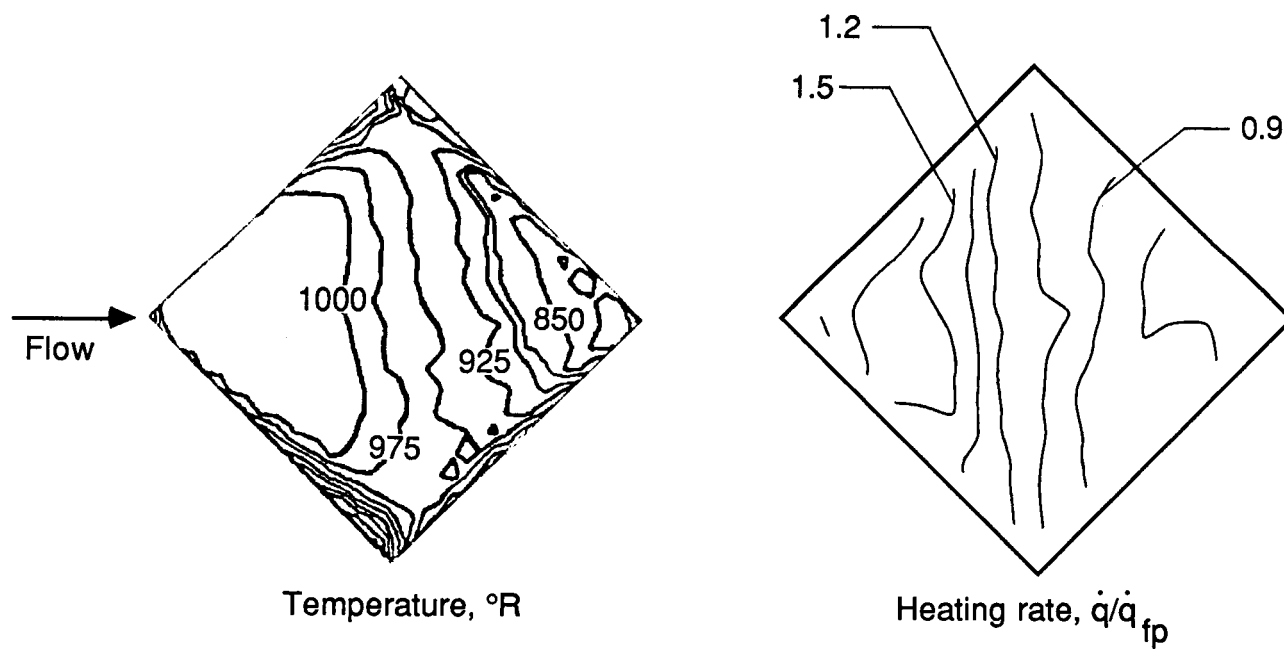


(b) Skewed array, laminar B.L. with blunt L.E. (no trips).

Figure 10. Comparison of temperature and heating-rate contours. $H = 0.4$ in.

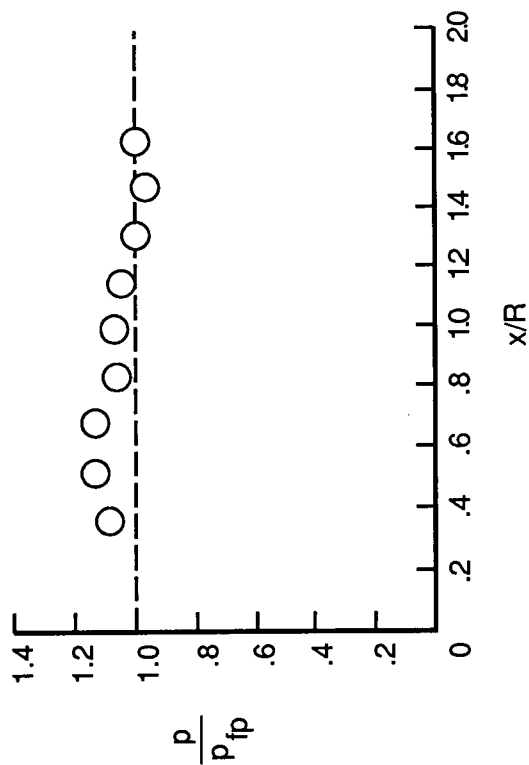
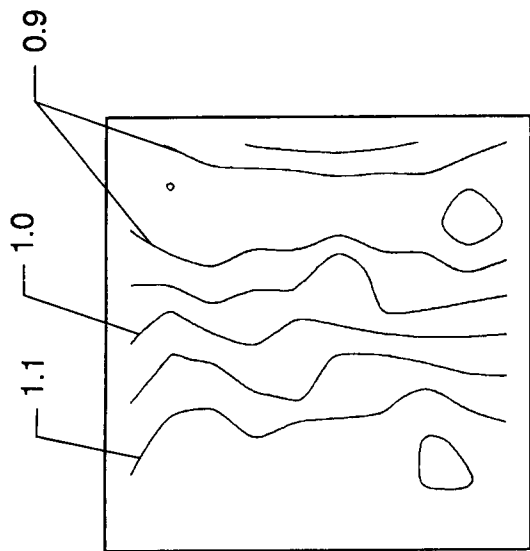
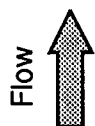


(c) Aligned array, turbulent B.L. with sharp L.E. (trips).

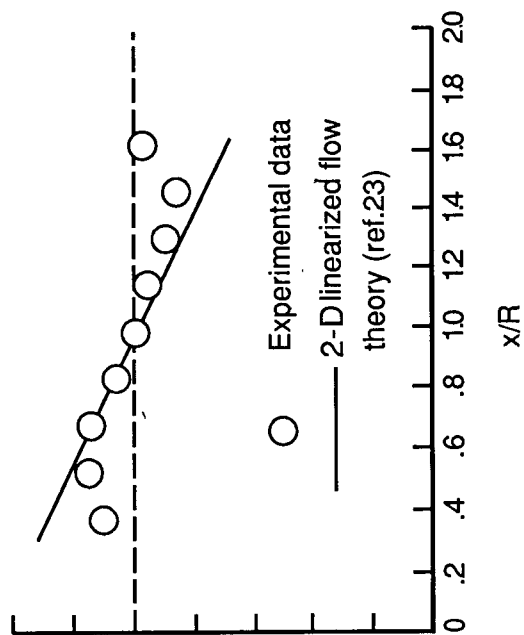


(d) Skewed array, turbulent B.L. with sharp L.E. (trips).

Figure 10. Concluded.

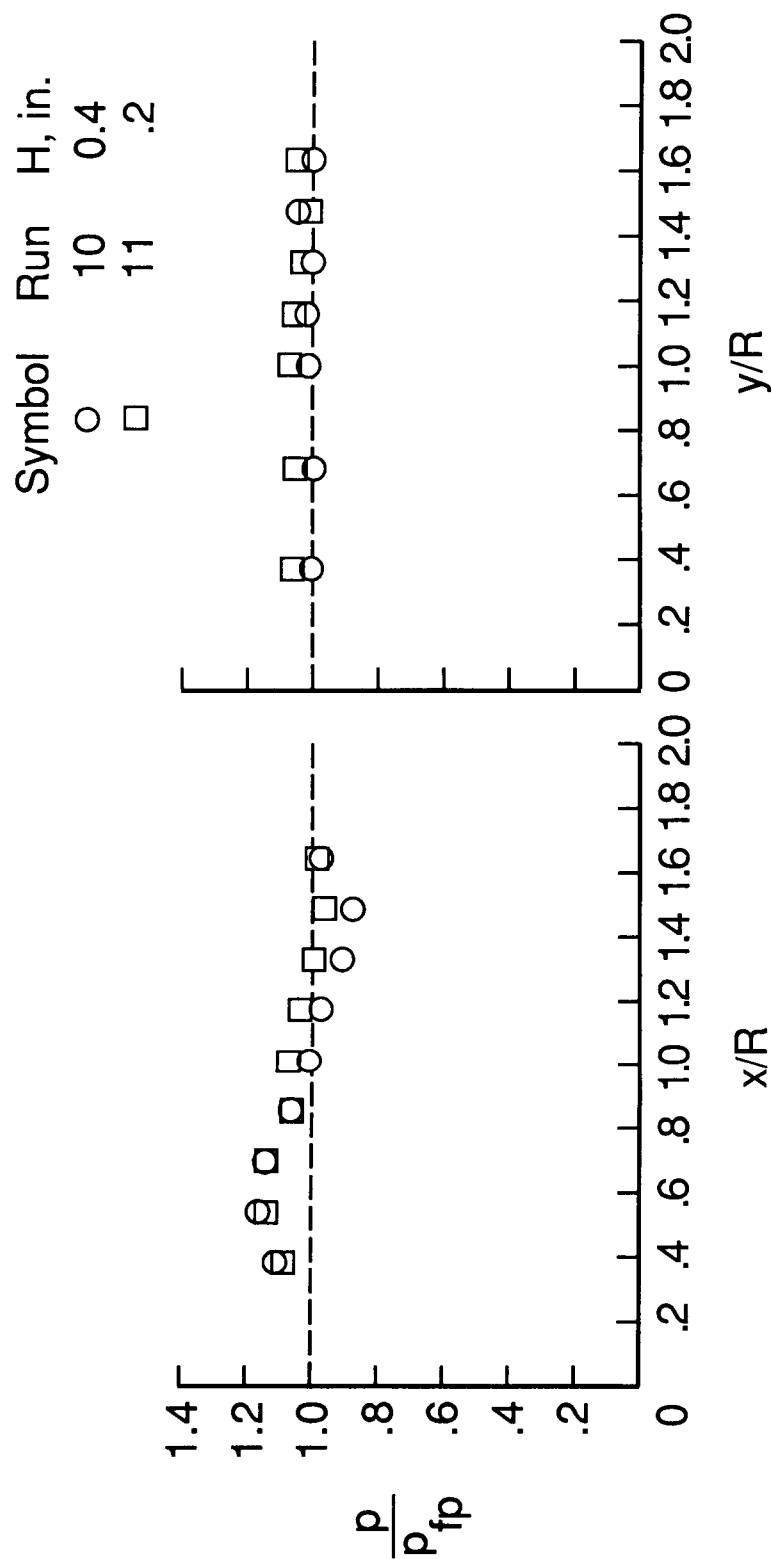


(a) Nominal height $H = 0.2$ in.



(b) Nominal height $H = 0.4$ in.

Figure 11. Pressure contours and longitudinal distributions on the aligned pressure dome, laminar B.L. with blunt L.E. (no trips).



(a) Longitudinal distributions.
 (b) Lateral distributions.

Figure 12. Pressure on the aligned pressure dome, laminar B.L. with blunt L.E. (no trips).

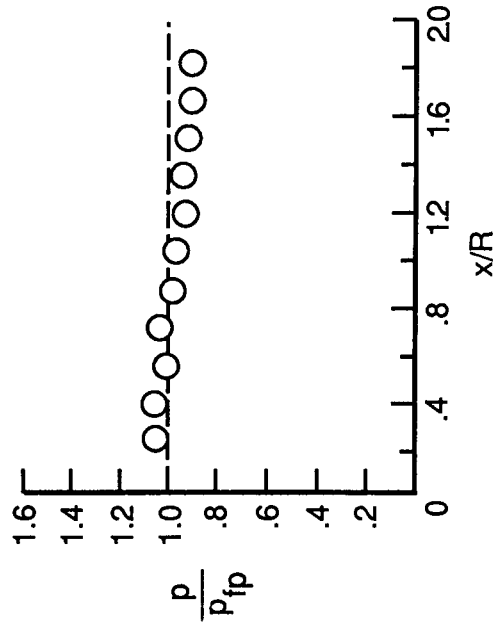
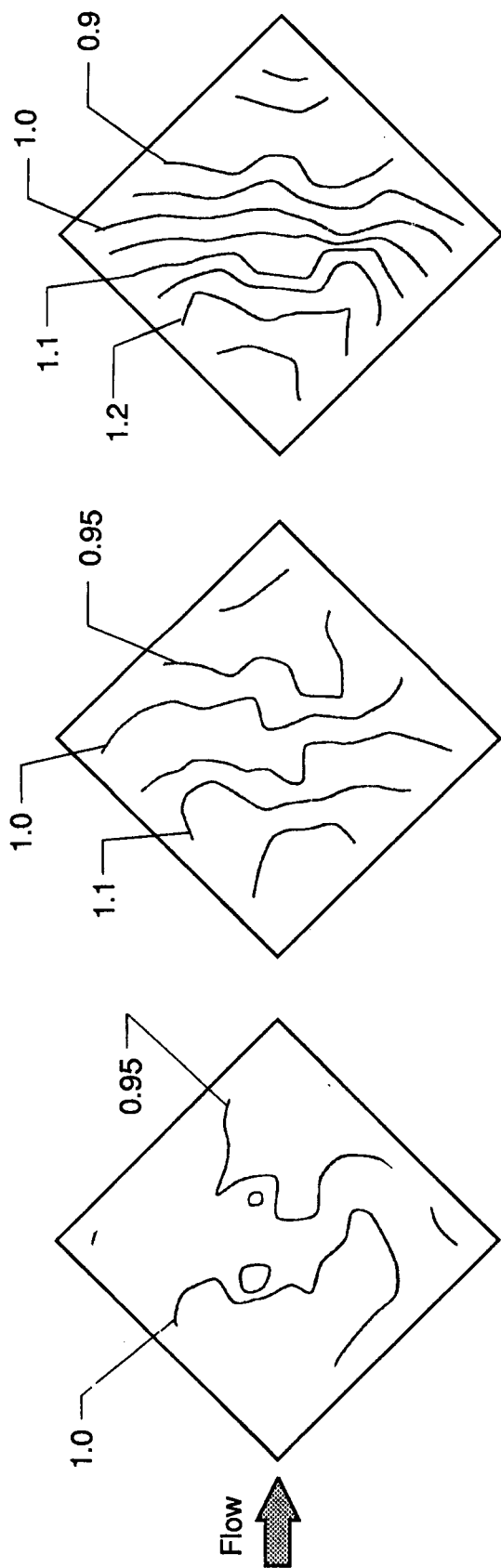
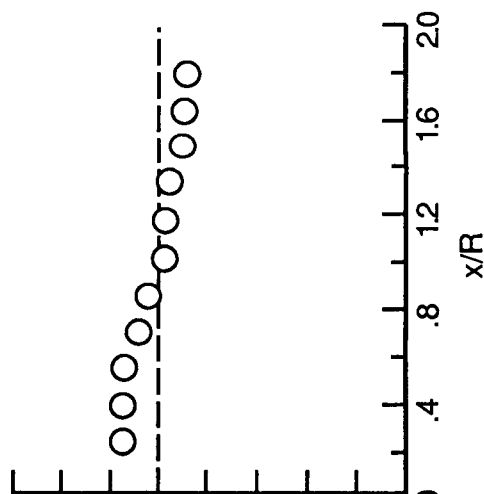
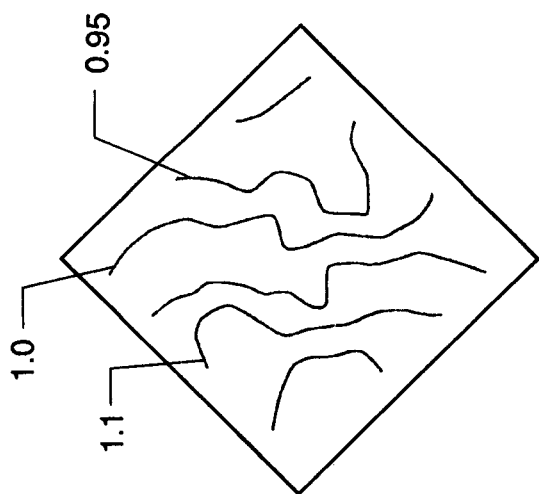
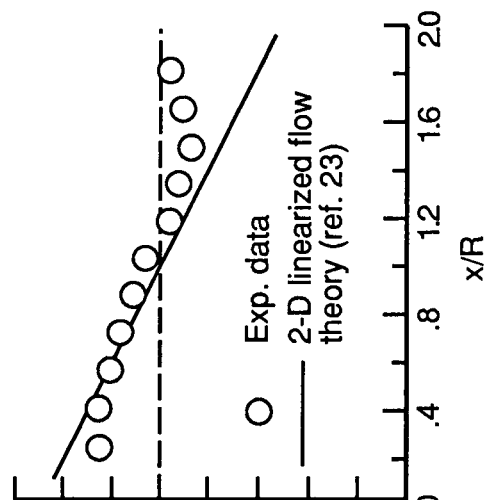
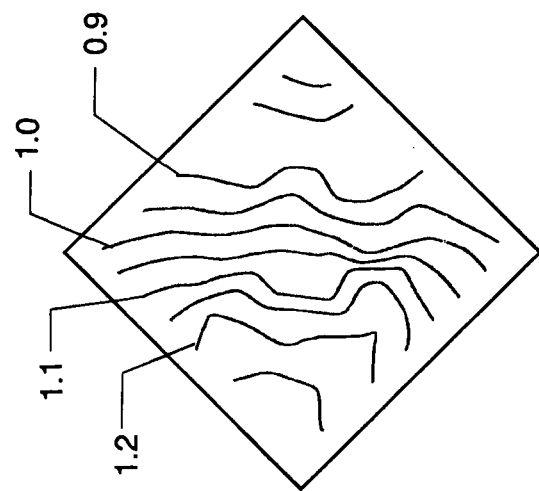
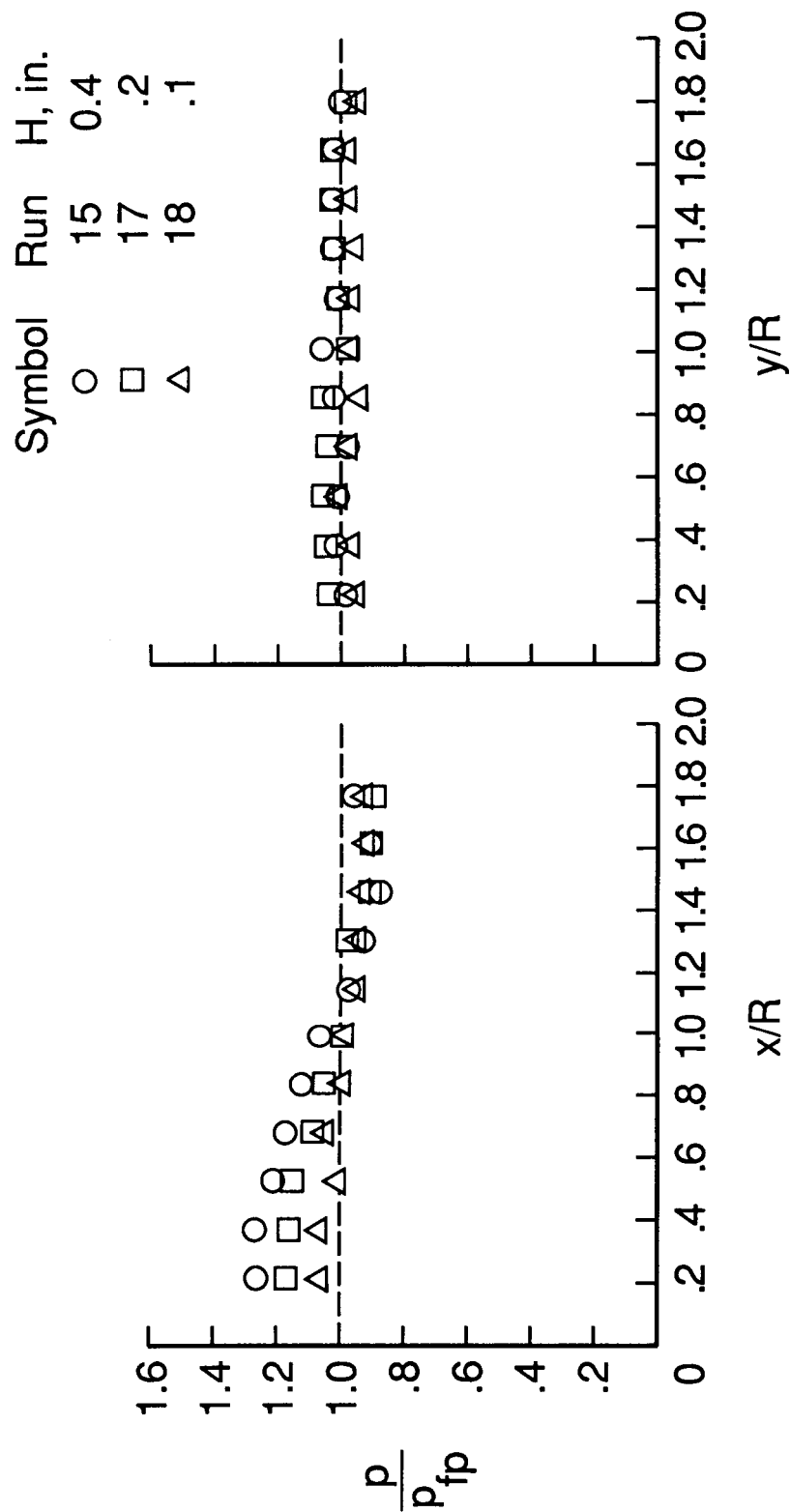
(a) Nominal height $H = 0.1$ in.(b) Nominal height $H = 0.2$ in.(c) Nominal height $H = 0.4$ in.

Figure 13. Pressure contours and longitudinal distributions on the skewed pressure dome, laminar B.L. with blunt L.E. (no trips).



(a) Longitudinal distributions.

(b) Lateral distributions.

Figure 14. Pressure on the skewed pressure dome, laminar B.L. with blunt L.E. (no trips).

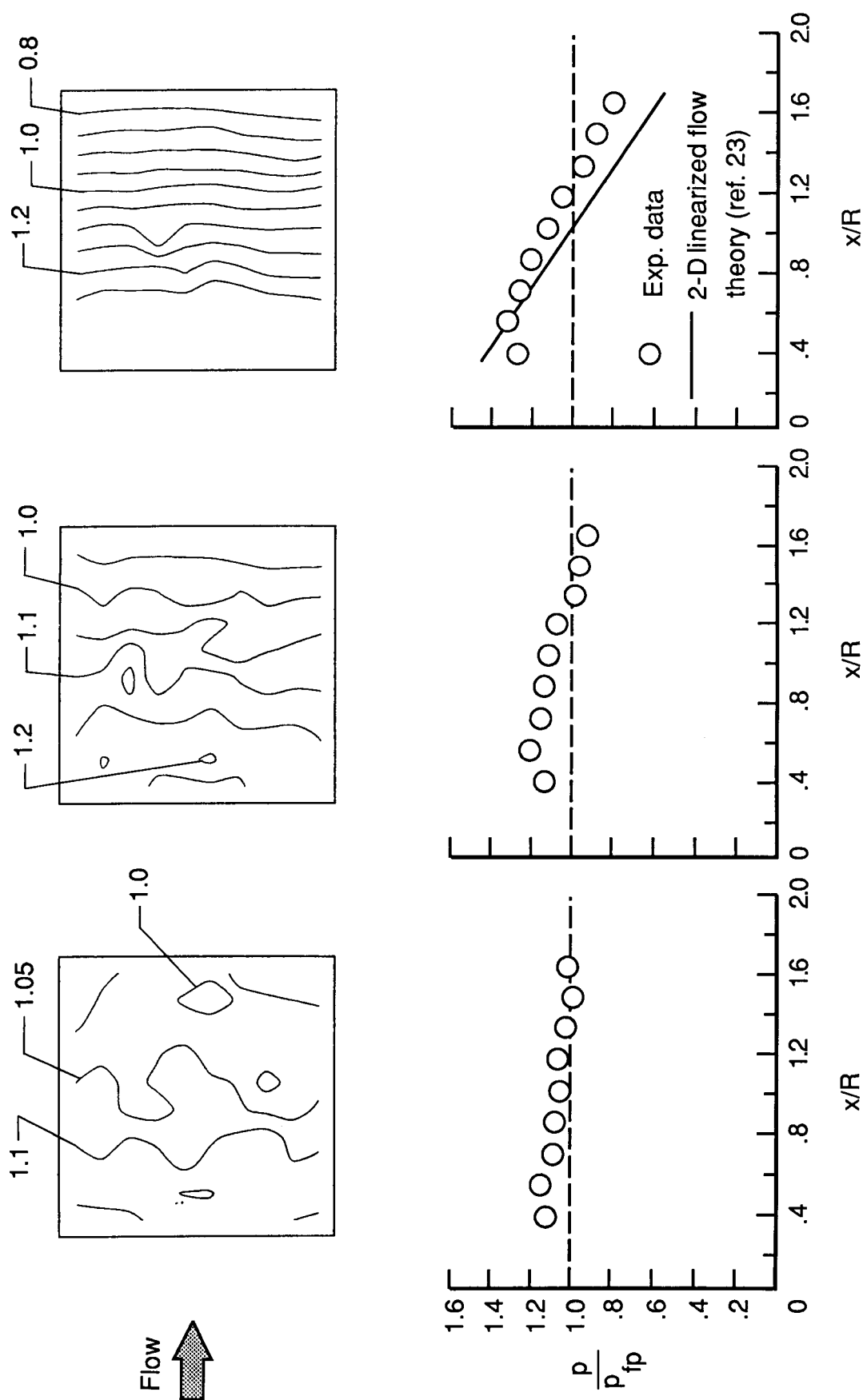
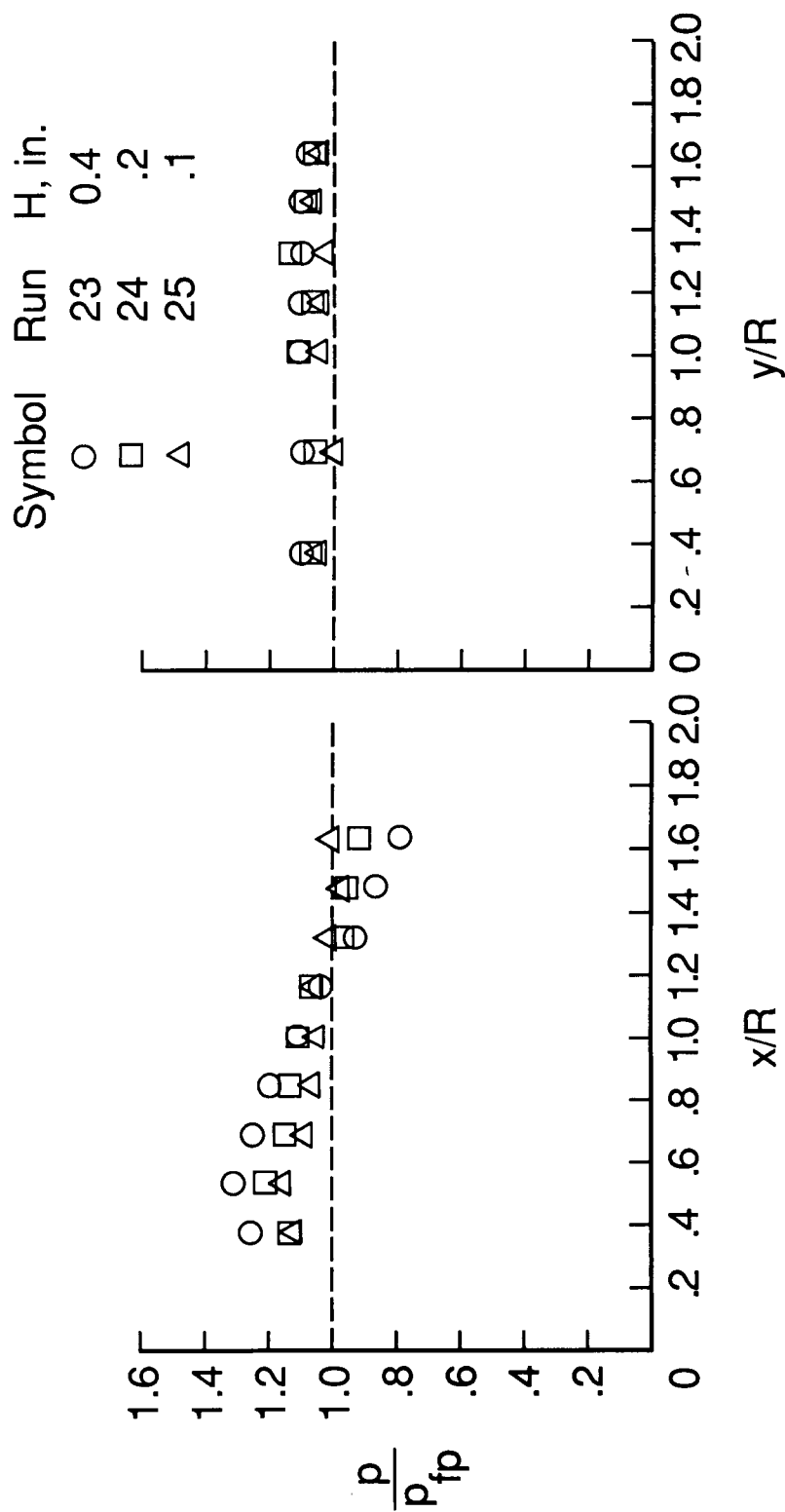


Figure 15. Pressure contours and longitudinal distributions on the aligned pressure dome, turbulent B.L. with sharp L.E. (trips).



(a) Longitudinal distributions.

(b) Lateral distributions.

Figure 16. Pressure on the aligned pressure dome, turbulent B.L. with sharp L.E. (trips).

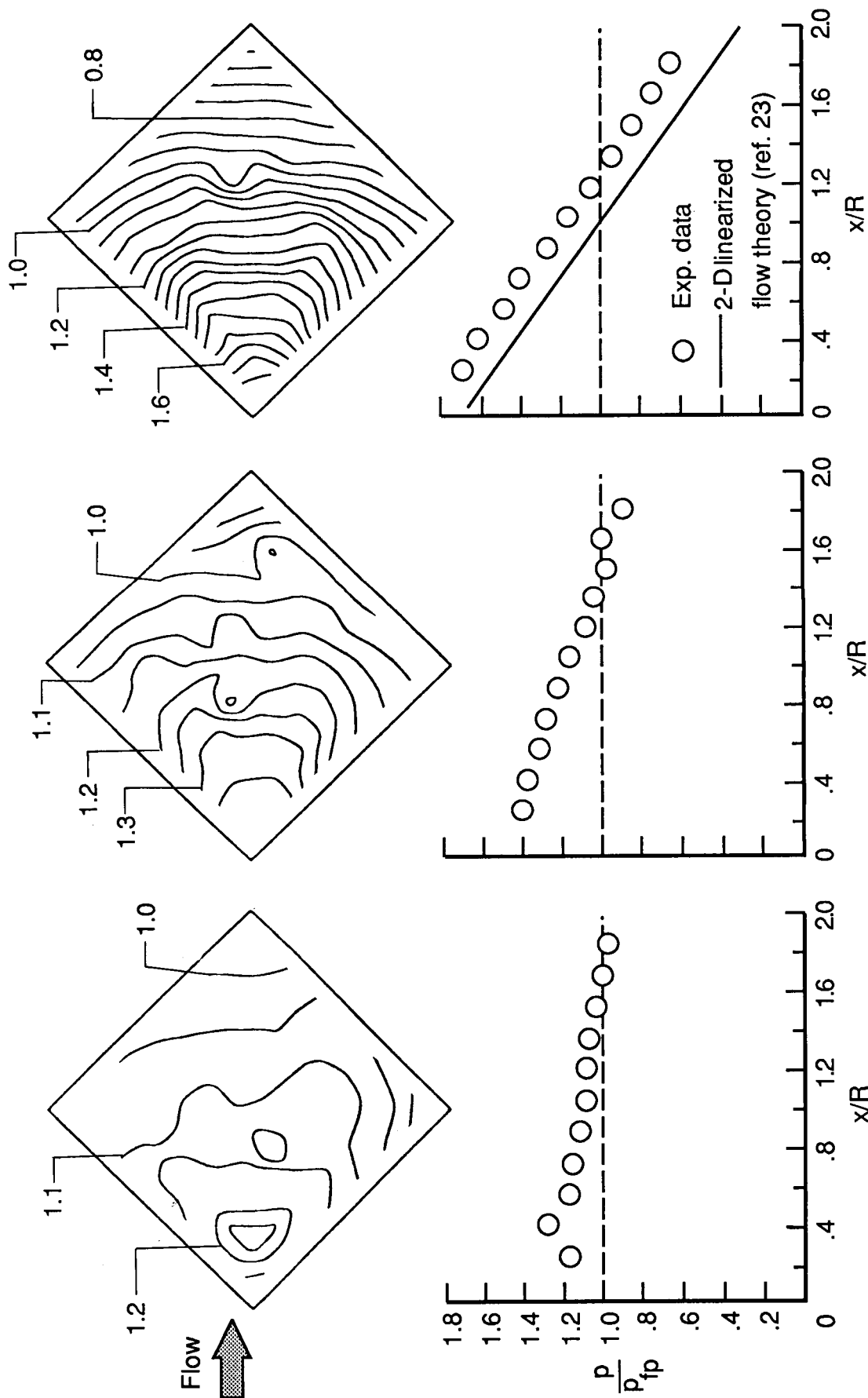
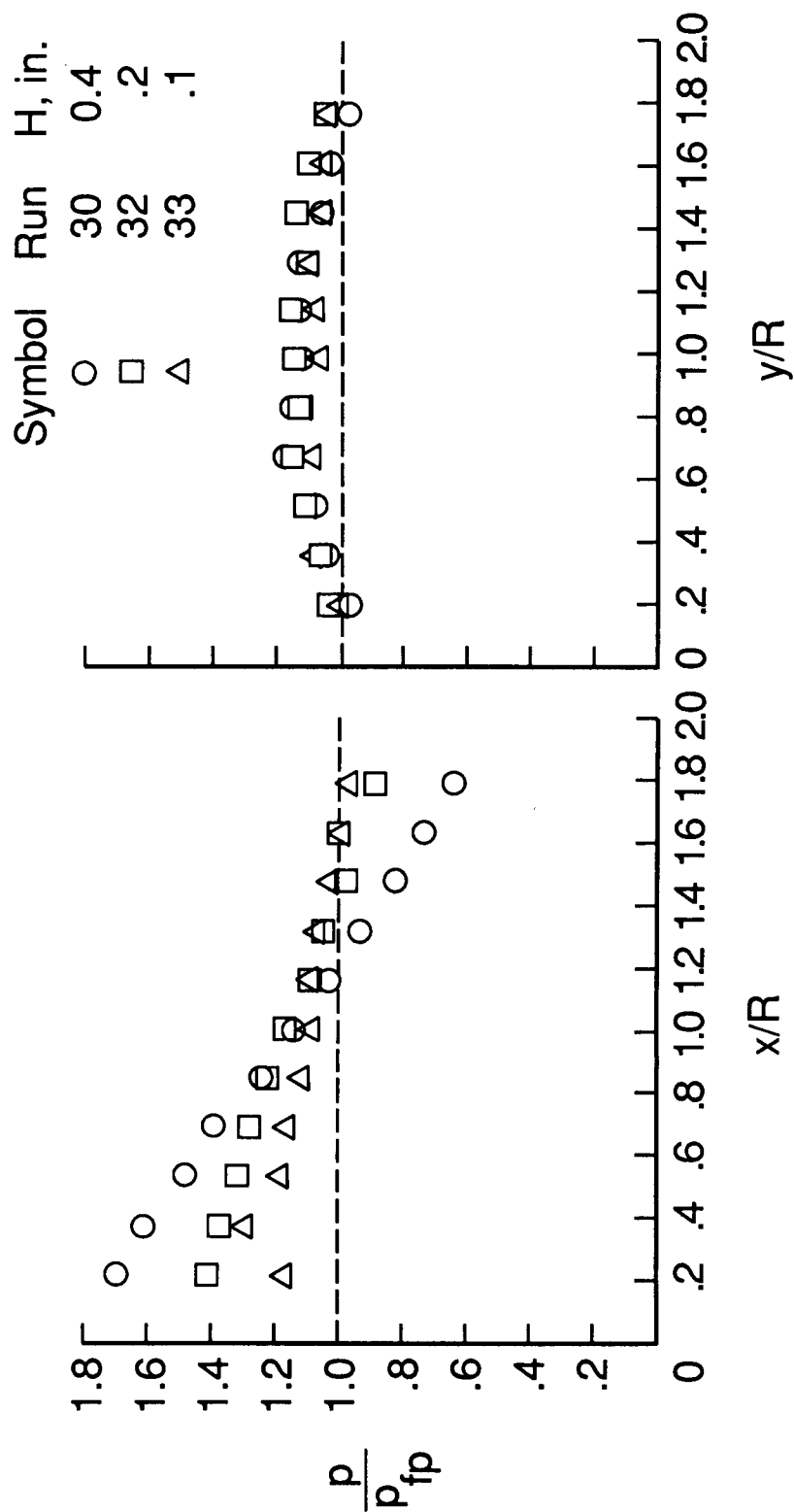


Figure 17. Pressure contours and longitudinal pressure distributions on the skewed pressure dome, turbulent B.L. with sharp L.E. (trips).



(a) Longitudinal distributions.

(b) Lateral distributions.

Figure 18. Pressure on the skewed pressure dome, turbulent B.L. with sharp L.E. (trips).

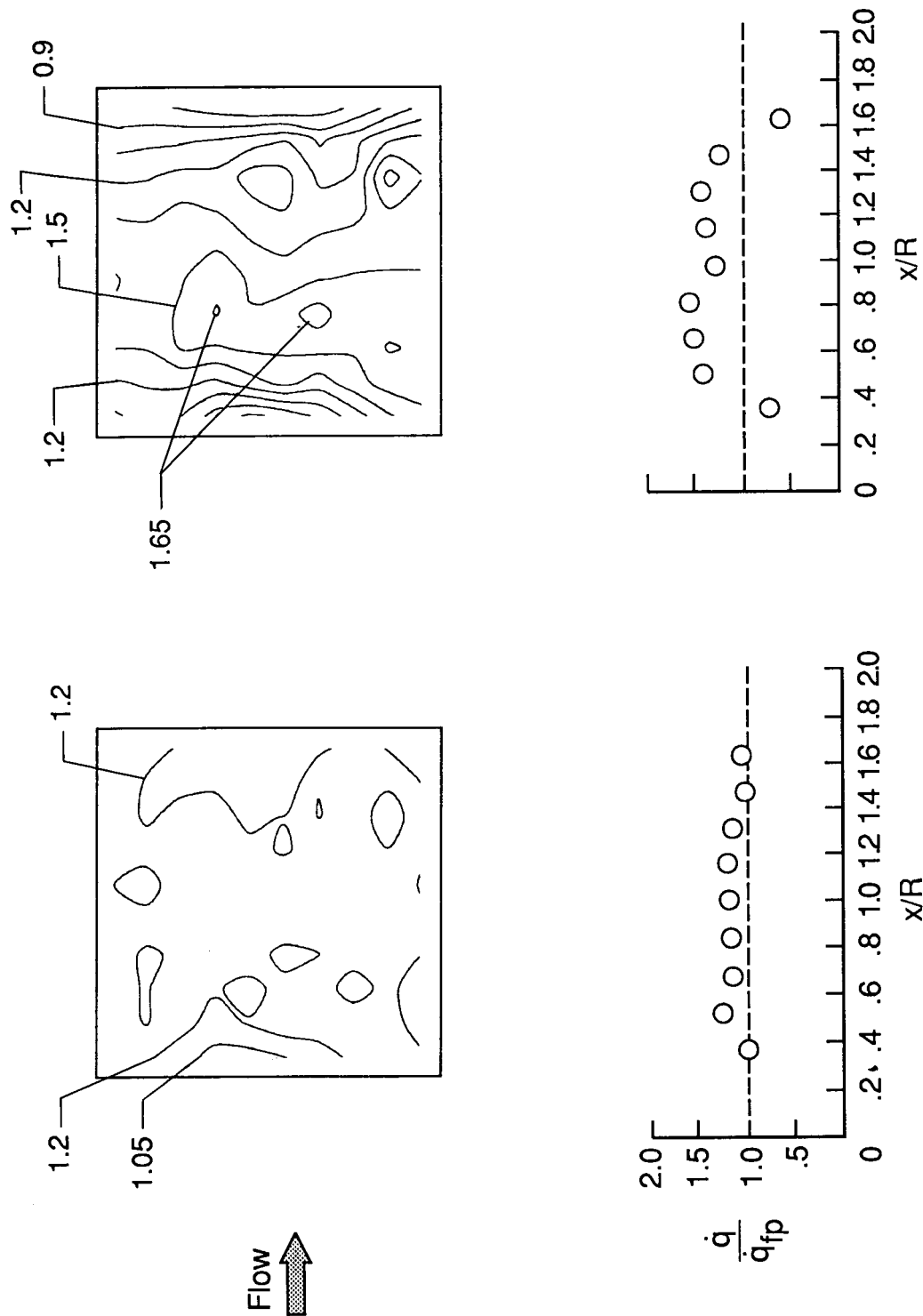


Figure 19. Heating-rate contours and longitudinal distributions on the aligned heat flux dome, laminar B.L. with blunt L.E. (no trips).

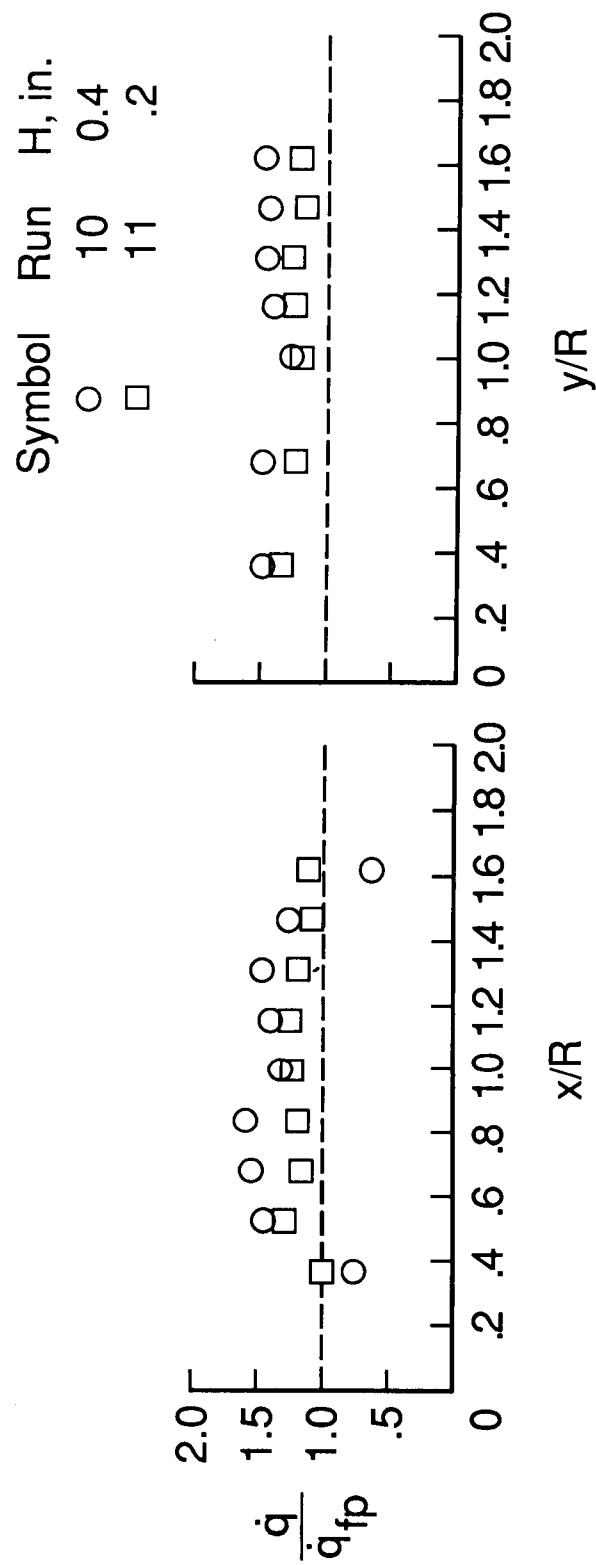
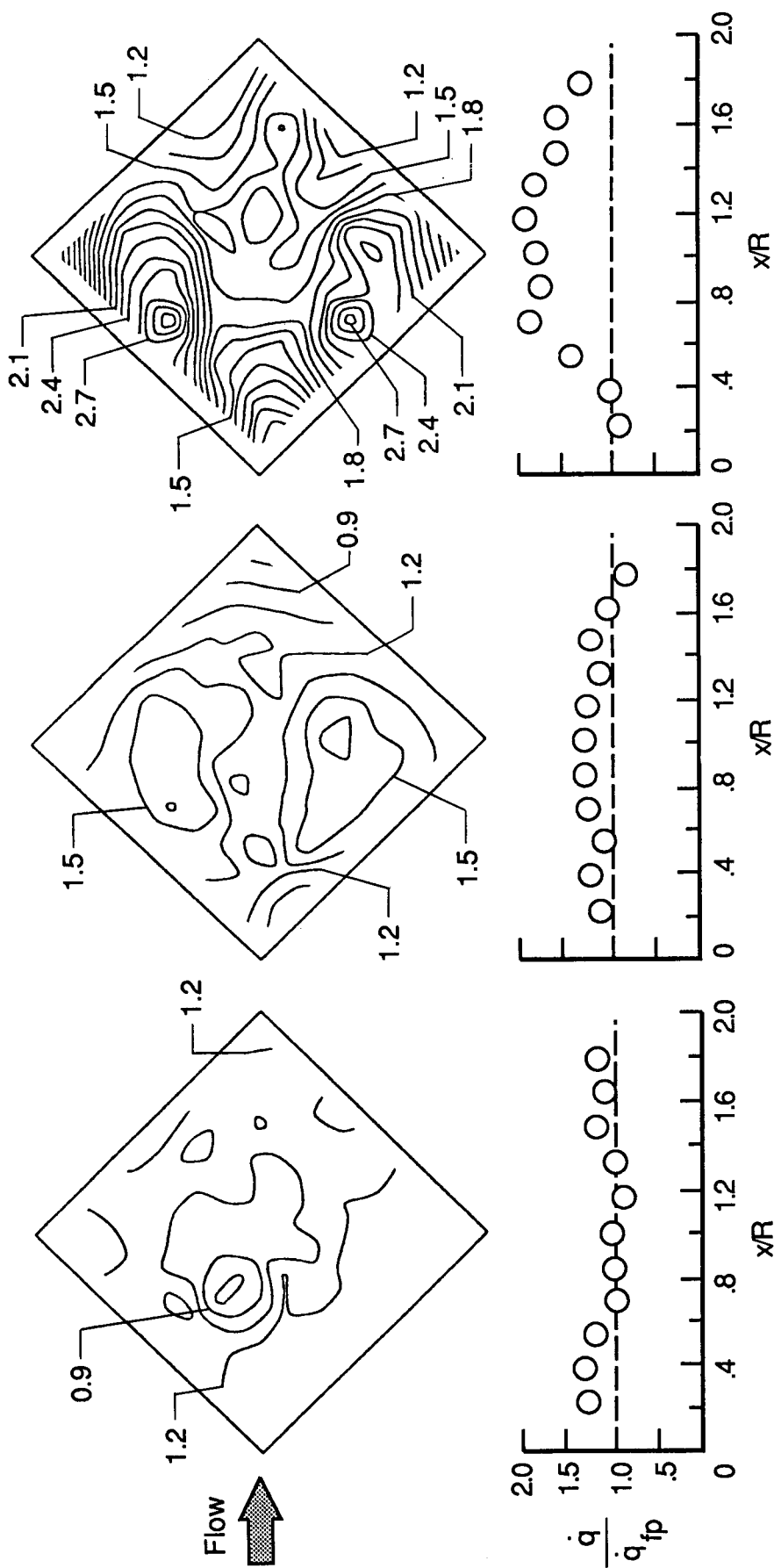
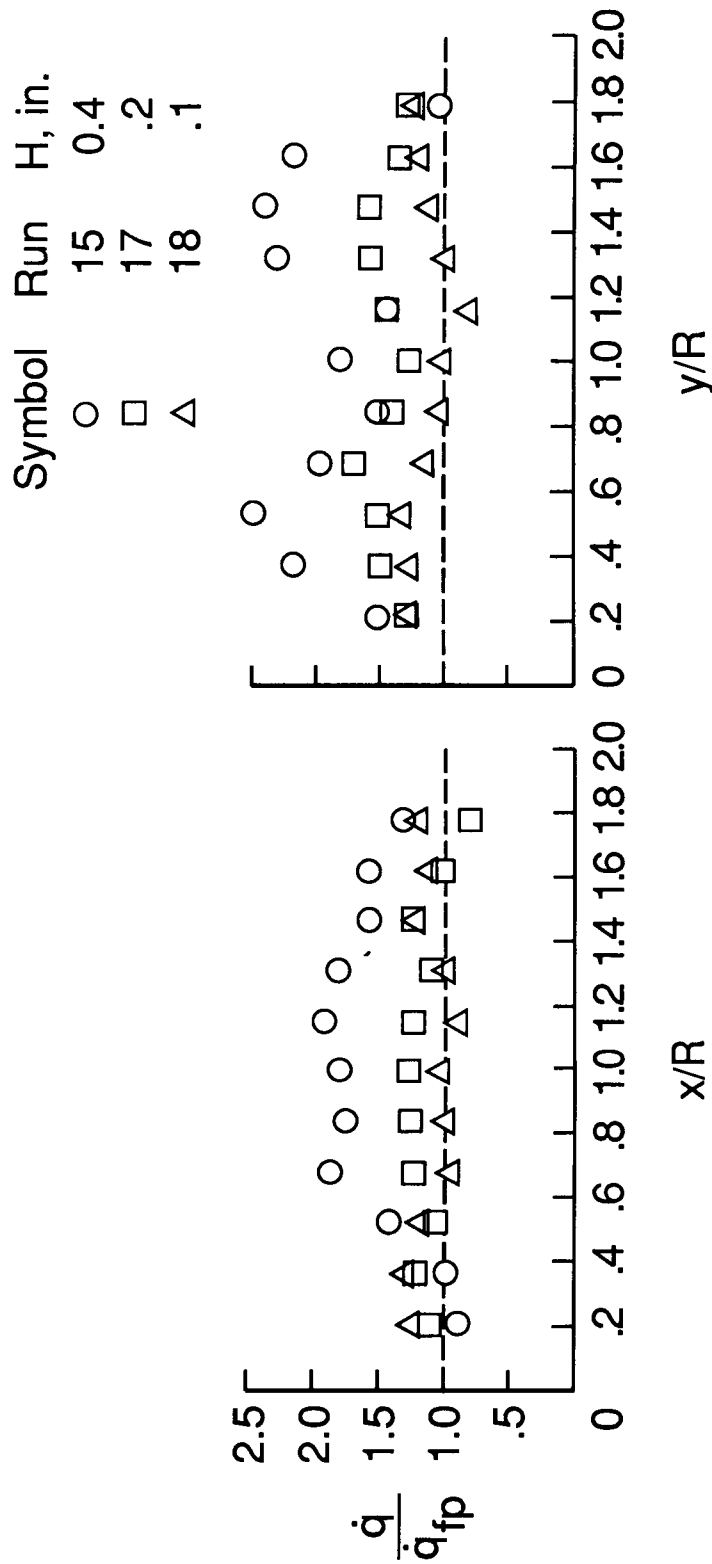


Figure 20. Heating rate on the aligned heat flux dome, laminar B.L. with blunt L.E. (no trips).



(a) Nominal height $H = 0.1$ in. (b) Nominal height $H = 0.2$ in. (c) Nominal height $H = 0.4$ in.

Figure 21. Heating-rate contours and longitudinal distributions on the skewed heat flux dome, laminar B.L. with blunt L.E. (no trips).



(a) Longitudinal distributions.

(b) Lateral distributions.

Figure 22. Heating rate on the skewed heat flux dome, laminar B.L. with blunt L.E. (no trips).

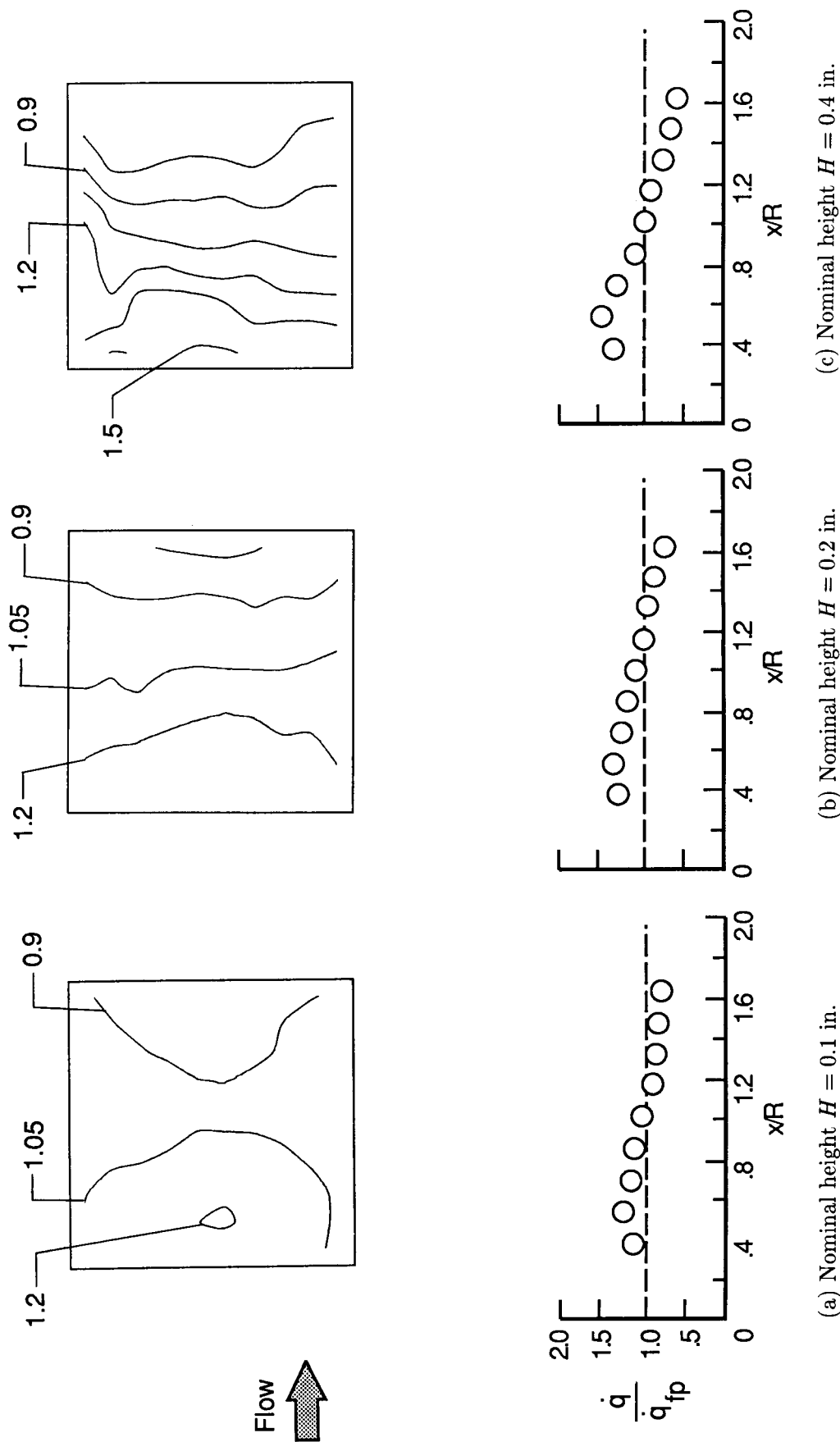


Figure 23. Heating-rate contours and longitudinal distributions on the aligned heat flux dome, turbulent B.L. with sharp L.E. (trips).

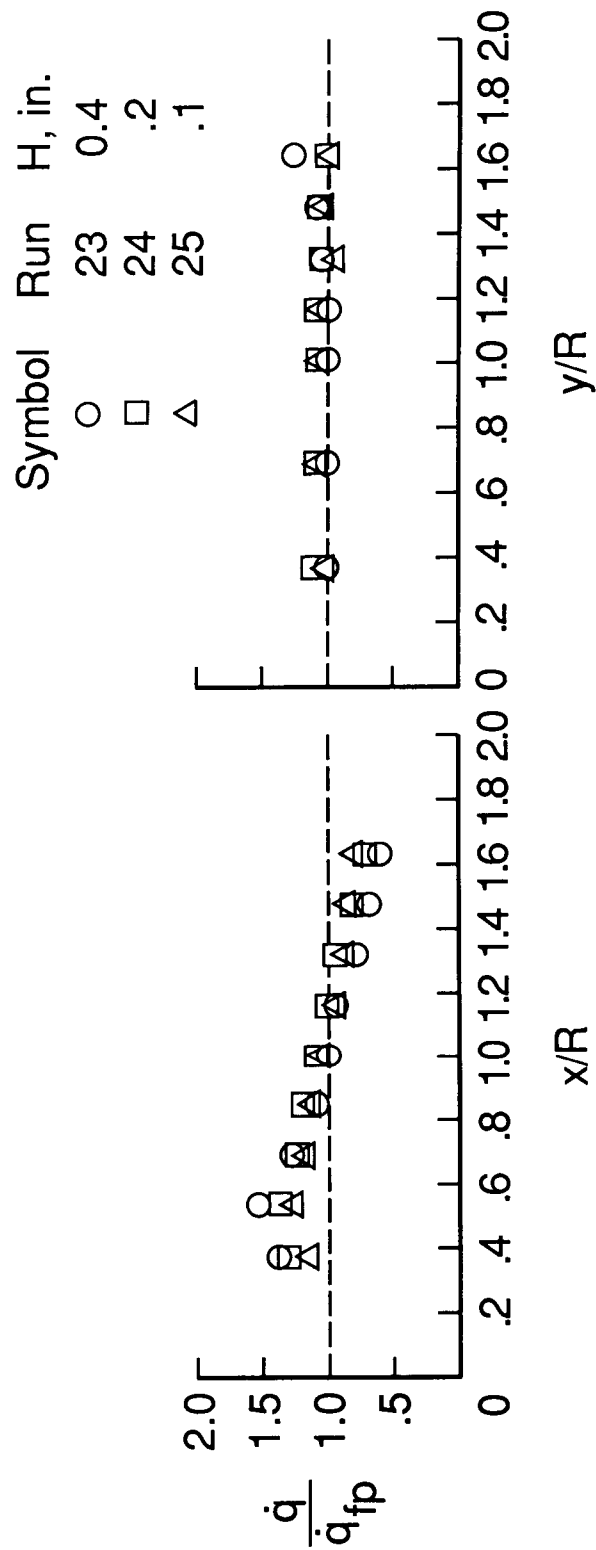


Figure 24. Heating rate on the aligned heat flux dome, turbulent B.L. with sharp L.E. (trips).

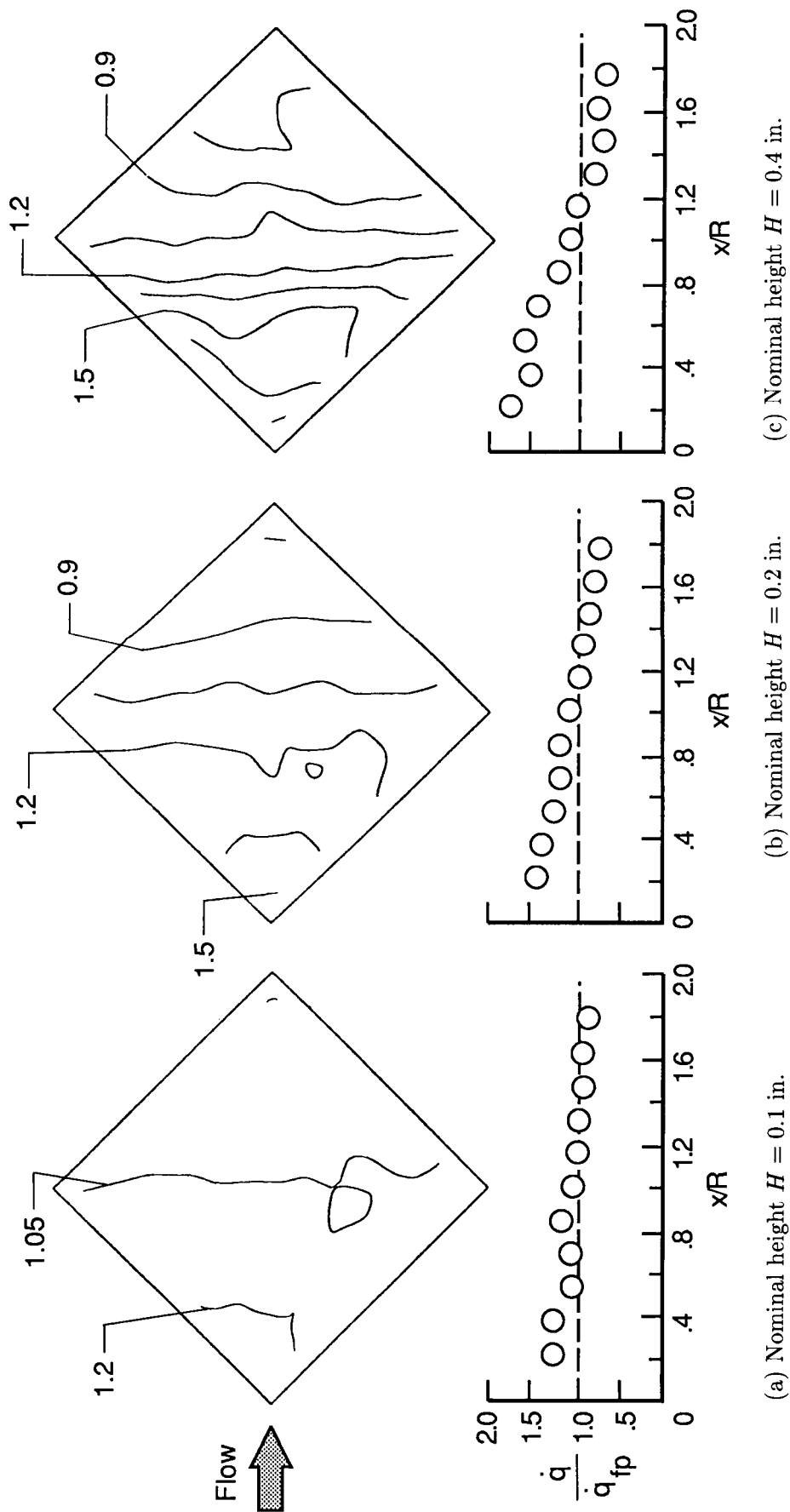
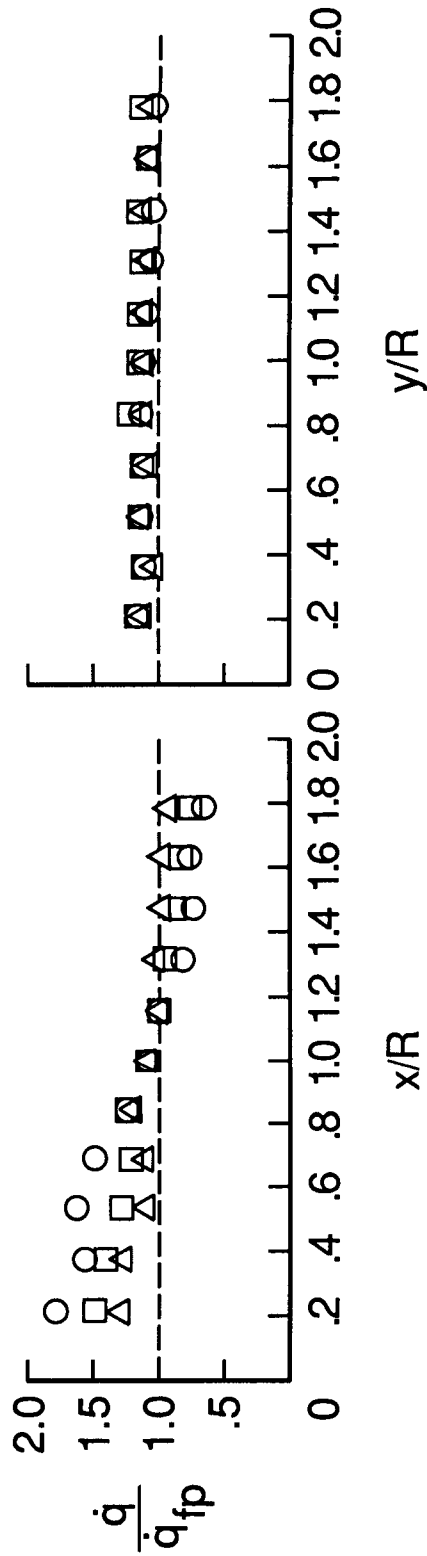


Figure 25. Heating-rate contours and longitudinal distributions on the skewed heat flux dome, turbulent B.L. with sharp L.E. (trips).

Symbol	Run	H, in.
○	30	0.4
□	32	.2
△	33	.1



(a) Longitudinal distributions.
 (b) Lateral distributions.

Figure 26. Heating rate on the skewed heat flux dome, turbulent B.L. with sharp L.E. (trips).

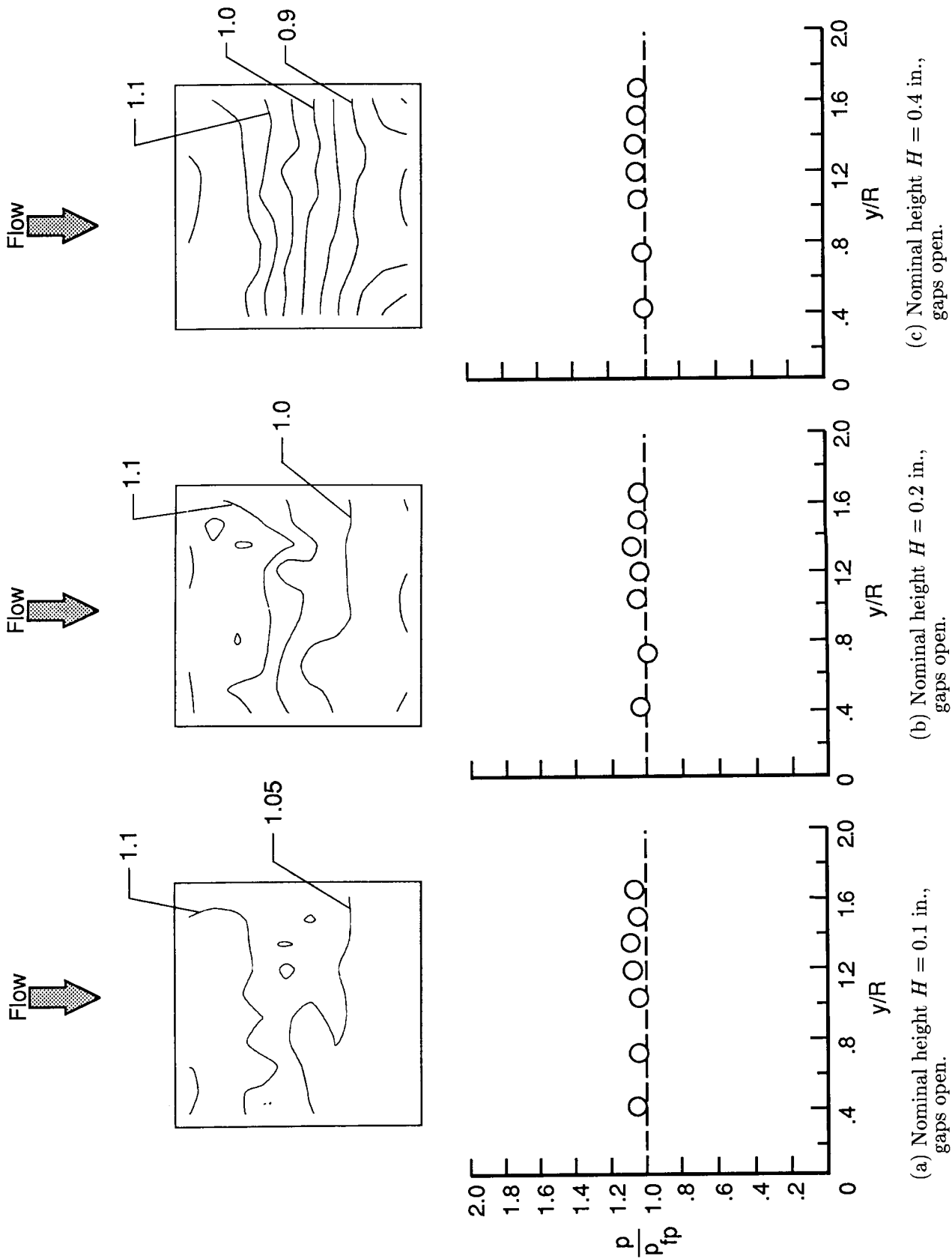


Figure 27. Pressure contours and lateral distributions on the aligned pressure dome showing gap effects, laminar B.L. with blunt L.E. (no trips).

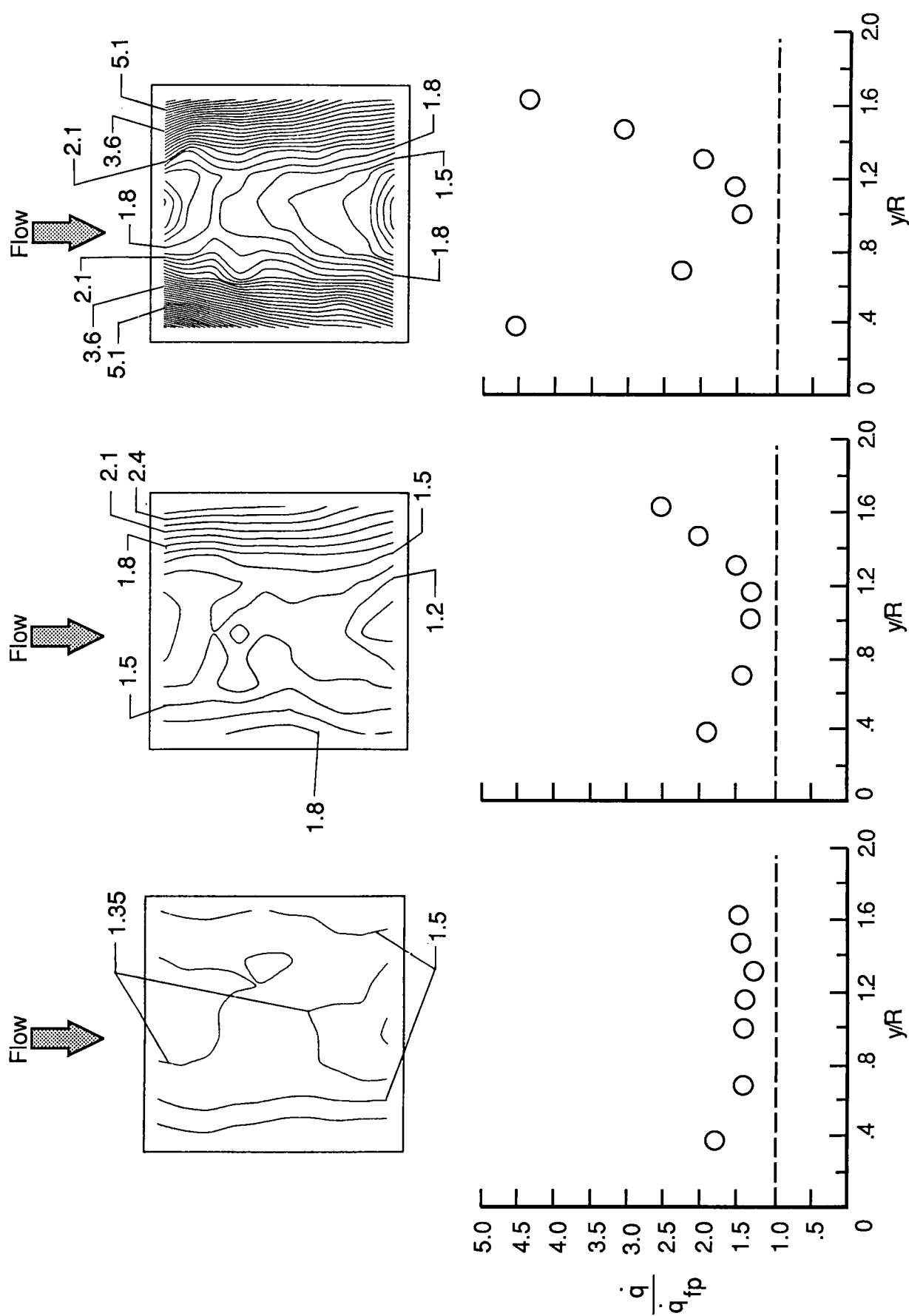
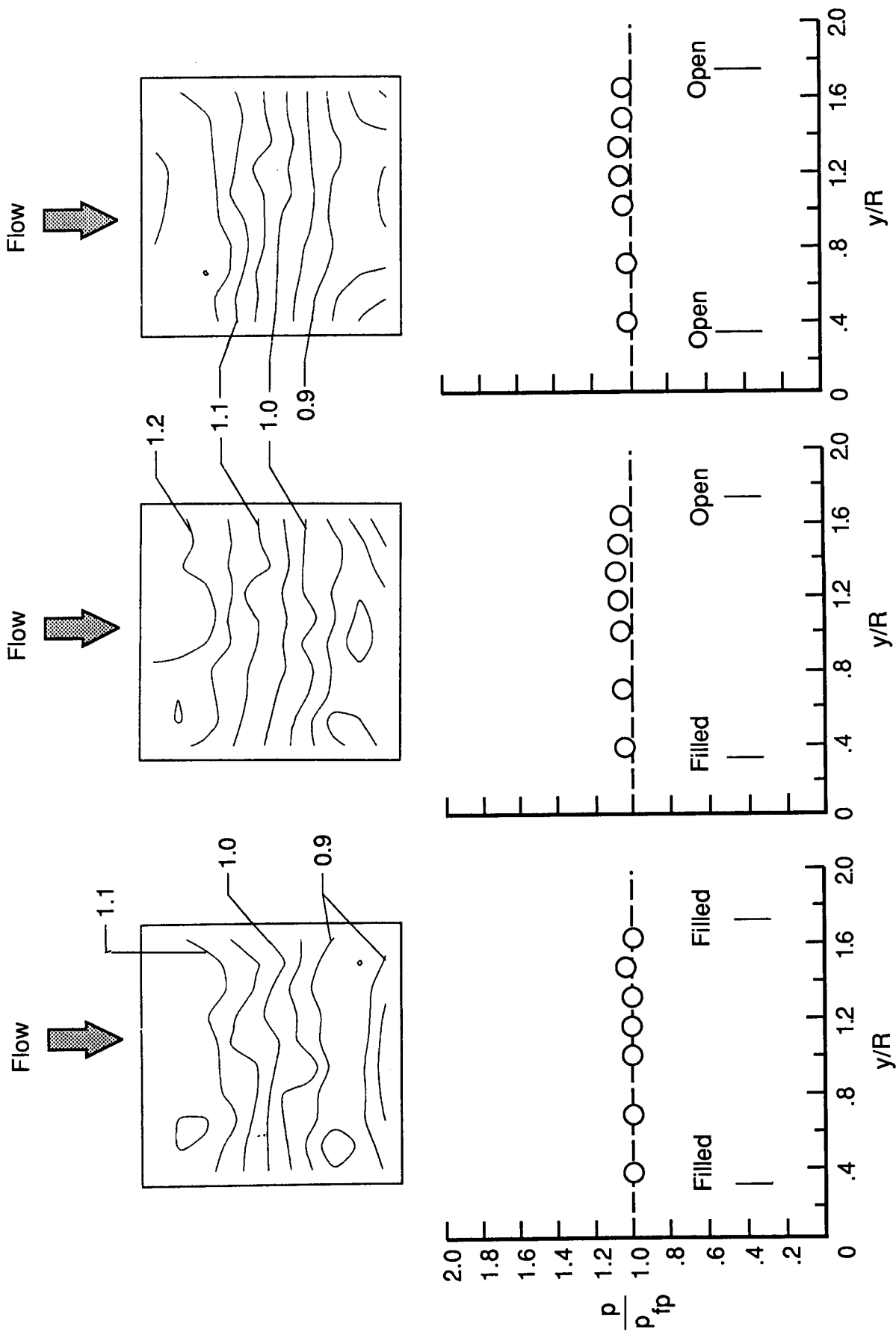
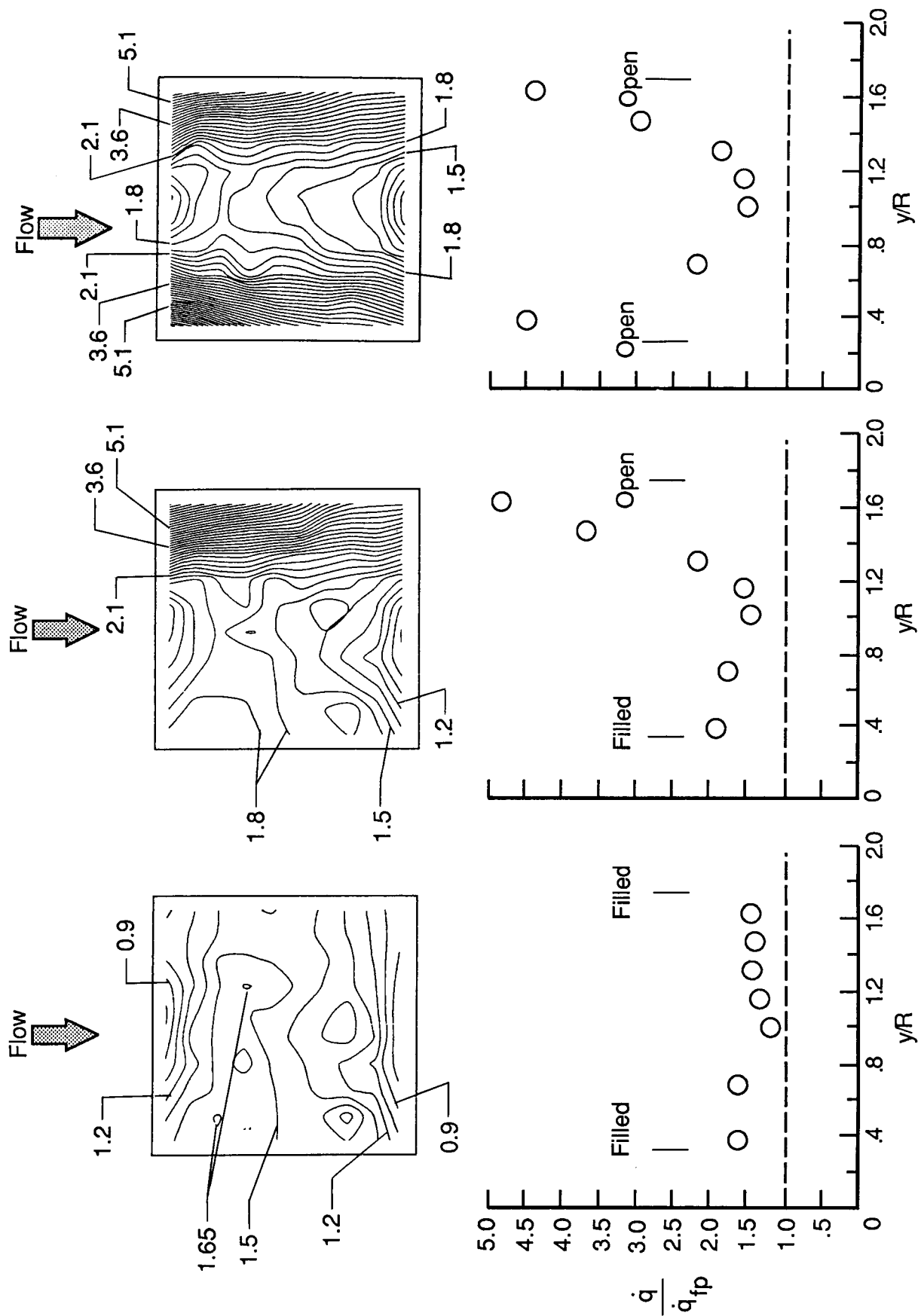


Figure 28. Heating-rate contours and lateral distributions on the aligned heat flux dome with gaps open, laminar B.L. with blunt L.E. (no trips).



(a) Nominal height $H = 0.4$ in., gaps filled. (b) Nominal height $H = 0.4$ in., starboard gap open. (c) Nominal height $H = 0.4$ in., gaps open.

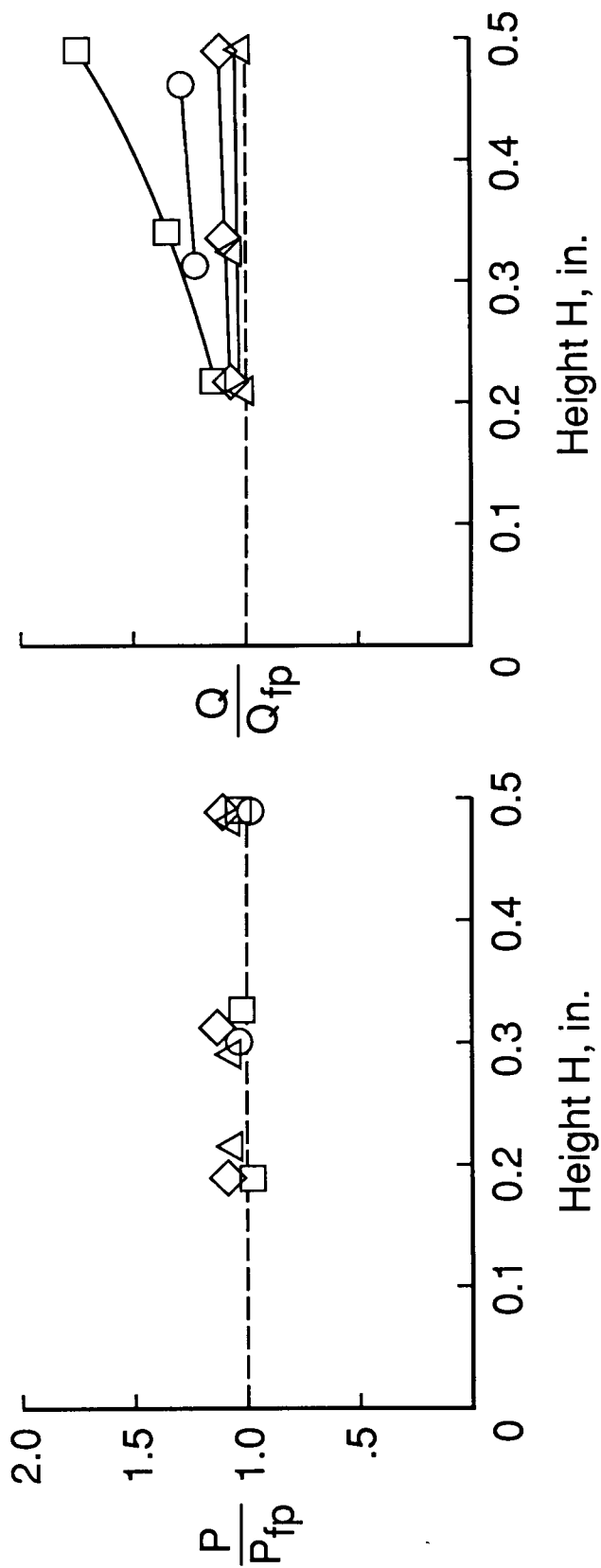
Figure 29. Pressure contours and lateral distributions on the aligned pressure dome showing gap effects, laminar B.L. with blunt L.E. (no trips).



(a) Nominal height $H = 0.4$ in., gaps filled. (b) Nominal height $H = 0.4$ in., starboard gap open. (c) Nominal height $H = 0.4$ in., gaps open.

Figure 30. Heating-rate contours and lateral distributions on the aligned heat flux dome gap effects, laminar B.L. with blunt L.E. (no trips).

- Aligned array, laminar B. L.
- Skewed array, laminar B. L.
- △ Aligned array, turbulent B. L.
- ◇ Skewed array, turbulent B. L.

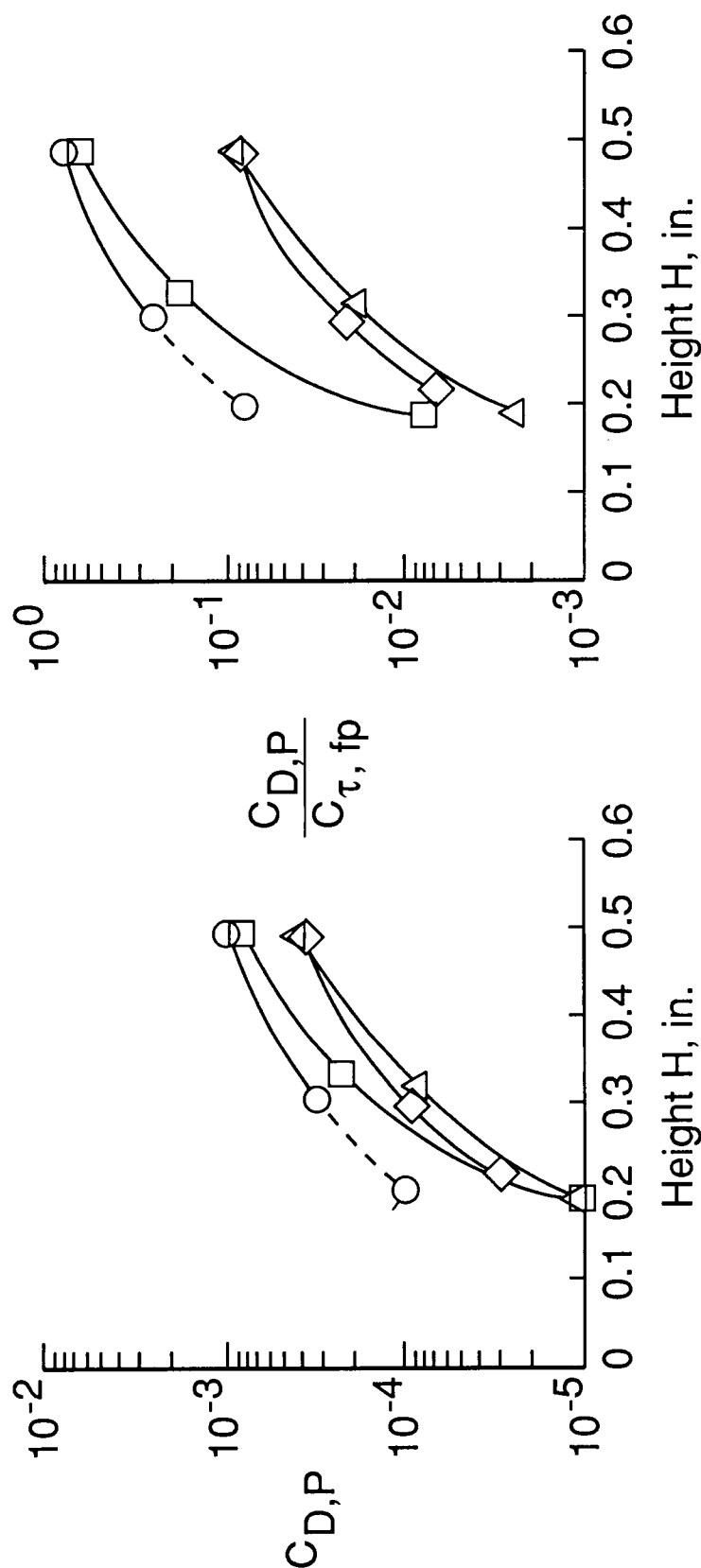


(a) Normalized pressure load.

(b) Normalized heat load.

Figure 31. Total integrated loads on the instrumented domes.

- Aligned array, laminar B.L.
- Aligned array, laminar B.L. (gaps open)
- Skewed array, laminar B.L.
- ◇ Aligned array, turbulent B.L.
- △ Skewed array, turbulent B.L.



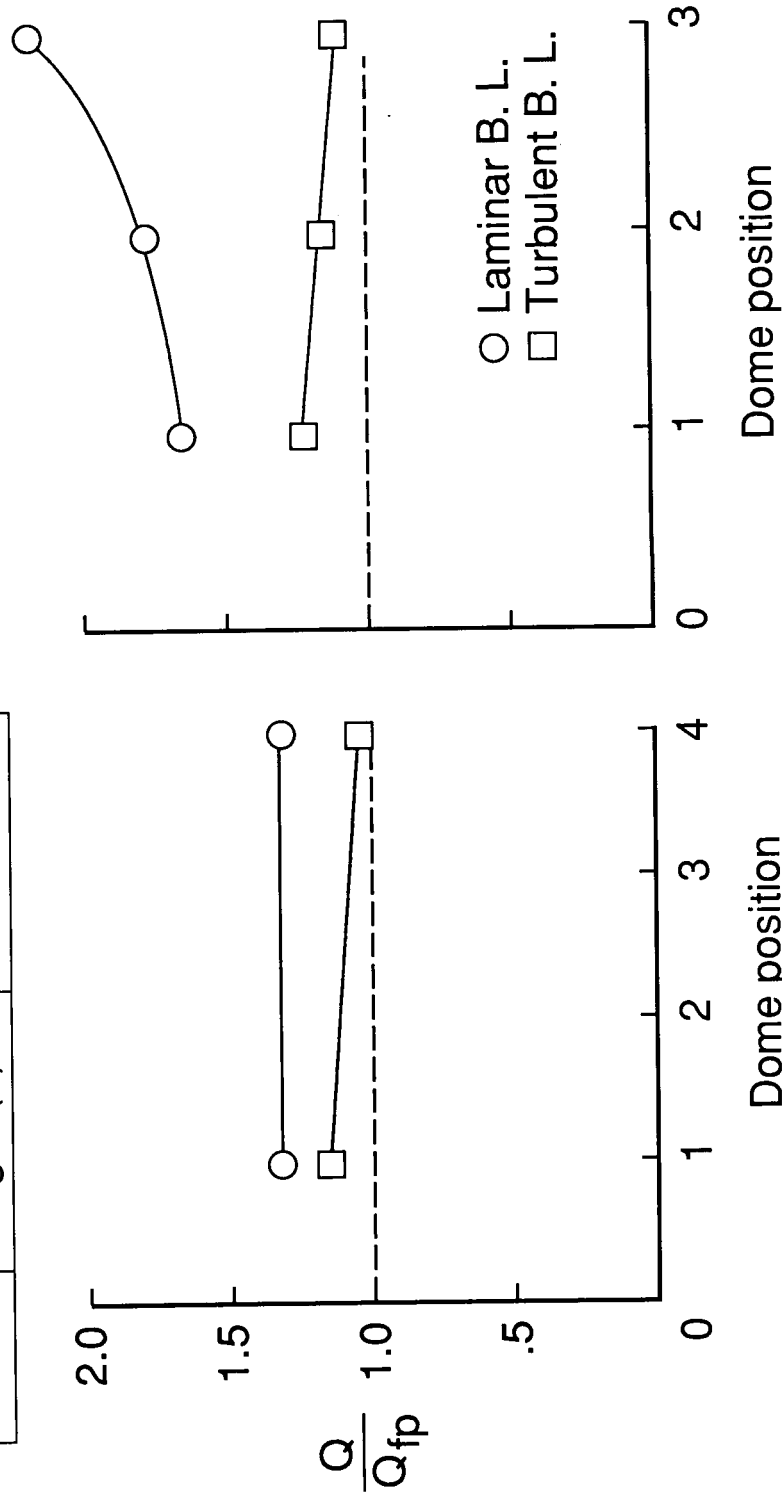
(a) Pressure drag coefficient, $C_{D,P}$.

(b) Pressure drag coefficient $C_{D,P}$, normalized to flat-plate skin-friction coefficient $C_{\tau,fp}$.

Figure 32. Variation of pressure drag coefficient with dome height.

Dome position	Configuration	Location (see fig. 4)
1	fig. 4(b)	2
2	fig. 4(b)	3
3	fig. 4(c)	3

Dome position	Configuration	Location (see fig. 4(a))
1	ref. 13	1
2	-	-
3	-	-
4	fig. 4(a)	4



(b) Skewed array.

(a) Aligned array.

Figure 33. Total integrated heat loads at various positions on the quilted dome model. $H = 0.4$ in.



Report Documentation Page

1. Report No. NASA TP-2804	2. Government Accession No.	3. Recipient's Catalog No.	
4. Title and Subtitle Aerothermal Tests of Quilted Dome Models on a Flat Plate at a Mach Number of 6.5		5. Report Date May 1988	
		6. Performing Organization Code	
7. Author(s) Christopher E. Glass and L. Roane Hunt		8. Performing Organization Report No. L-16346	
		10. Work Unit No. 506-40-21-01	
9. Performing Organization Name and Address NASA Langley Research Center Hampton, VA 23665-5225		11. Contract or Grant No.	
		13. Type of Report and Period Covered Technical Paper	
12. Sponsoring Agency Name and Address National Aeronautics and Space Administration Washington, DC 20546-0001		14. Sponsoring Agency Code	
15. Supplementary Notes			
16. Abstract Aerothermal tests were conducted in the NASA Langley 8-Foot High-Temperature Tunnel (8' HTT) at a Mach number of 6.5 on simulated arrays of thermally bowed metallic thermal protection system (TPS) tiles at an angle of attack of 5°. Detailed surface pressures and heating rates were obtained for arrays aligned with the flow and skewed 45° diagonally to the flow with nominal bowed heights of 0.1, 0.2, and 0.4 in. submerged in both laminar and turbulent boundary layers. Aerothermal tests were made at a nominal total temperature of 3300°R, a total pressure of 400 psia, a total enthalpy of 950 Btu/lbm, a dynamic pressure of 2.7 psi, and a unit Reynolds number of 0.4×10^6 per foot. The experimental results form a data base that can be used to help predict aerothermal load increases from bowed arrays of TPS tiles.			
17. Key Words (Suggested by Authors(s)) Hypersonic flight vehicle Thermal protection system Protuberance Pressure and heating-rate distributions Laminar and turbulent boundary layers Bowed tile arrays		18. Distribution Statement Unclassified—Unlimited	
		Subject Category 34	
19. Security Classif.(of this report) Unclassified	20. Security Classif.(of this page) Unclassified	21. No. of Pages 69	22. Price A04